UNIVERSITÀ DEGLI STUDI DI TRIESTE

Dipartimento di Fisica

PH.D. DISSERTATION

Impact of the Electron Dynamics on Coherence of Free-electron Lasers Radiation

Candidate:
Giovanni Perosa

Supervisor:
Prof. Simone Di Mitri

Co-supervisor:
Prof. Claudio Masciovecchio

Academic Year 2021 - 2022

Ph.D. School in Physics - XXXV Cycle

To my sister Giulia and my brother Andrea

"I sing the body electric..." — W. Whitman, *from "Leaves of grass"*

My Work in a Nutshell

Radiation from free-electron-lasers seeded by poissonian light (laser seeded FELs) shows a higher degree of longitudinal (temporal) coherence versus the radiation from self-amplified spontaneous emission free-electron lasers (SASE FELs). Nonetheless, energy and density modulations in the electron bunch may reduce the coherence of FEL light. In this scenario, we show that good agreement between theory and experiment requires considering intrabeam scattering mechanism. This finding raises the conjecture about how to observe the interplay between electron beam dynamics and decoherence phenomena, along with the measure of the quantum statistics of the seeded FEL light. To address the latter issue, we propose a novel method for detecting the degree of "poissonianity" of the distribution of photons under the constraint imposed by the multi-photon FEL pulses. At the same time, the question concerning the electron beam dynamics and decoherence phenomena is boosting interest in a new theory based on the Dirac equation in a quantized electromagnetic field. Such a theory must be suitable to predict the behavior of the FEL photons related to the laser-seeded electron bunch.

Abstract

Nowadays the possibility of generating ultrashort laser-like pulses from the TeraHertz (THz) to the X-ray spectral region stands at the frontier of the physics of light-matter interactions. For this reason, light-sources like inverse Compton scattering, high harmonic generation in gases (HHG) and laser-seeded free electron lasers (FELs) are important tools of research in several areas of the modern science.
In particular, they have in common the exploitation of the radiating process resulting from the acceleration of electrons under the influence of an electromagnetic field.
Interestingly, it is often stated that, when the emission is stimulated by an external laser, the coherence of the laser field is imprinted, at least to a certain degree, into the outgoing light. This is the case, for instance, of HHG and externally seeded FELs.
Aim of this thesis is to explore the impact of the electron dynamics on the coherent behavior of FELs seeded by an external laser. We demonstrate that the electron dynamics plays a major role in the conversion and transformation of the features of the light generated by these sources, such as coherence, which can be transmitted to electrons and "inherited" from the re-emitted light. To fulfill this purpose, both theoretical and experimental approaches have been used. Most of the models presented, derived or extended in this work, are supported by experimental evidence. Experiments has been conducted at the FERMI FEL of Elettra Sincrotrone Trieste, Italy.
The interplay between electrons and light properties is then investigated using both classical and quantum dynamics. While the former is routinely adopted to describe the FEL dynamics and collective phenomena in an electron bunch, the latter becomes mandatory to fully achieve an overall description of the phenomena involving the emission of photons.
The first chapter serves as an introduction to the concept of FEL mechanism and seeding from laser. In the second chapter the degree of coherence of seeded and unseeded Free-Electron Lasers in the classical regime is explored. Coherence is determined via first- and second-order correlation function measurements, demonstrating the higher second-order longitudinal coherence of the laser seeded FELs.
In the third chapter, a novel and comprehensive analytical model for electron beam longitudinal dynamics is described. This includes a phenomenon first observed in electron linacs, known as intrabeam scattering, which has been unveiled by us for the first time by investigating its impact on the electrons distribution. The predictions of this model are directly compared with beam and FEL measurements, showing good agreement. Various experimental evidences of the collective phenomenon in the electron bunch, known as microbunching instability, are supported by our model. These results include the commissioning of a novel experimental station installed at the FERMI FEL of Elettra Sincrotrone Trieste, Italy.
Our investigations offer some useful models for the prediction and characterization of the electron beam parameters, allowing to observe the correlations between coherence and instabilities originating in the electron bunch.
In the last chapter, we attempted to address the question concerning the capability to introduce quantum features, such as quantum coherence, in any process of harmonic generation driven by a coherent light pulse. In order to answer this question, we focus our attention on the characterization of quantum coherence via photon number distribution and the quantum electrodynamics of an electron in a laser field. Although the conclusions and discussions regard FELs, some of the theoretical results can be extended to describe any process of light-electron interaction.
The work reported in this thesis is the result of multi-task research, while my contribution is highlighted at the end of the introduction and at the beginning of each chapter.

Contents

Chapter 1

Introduction

Free-electron lasers (FELs) were originally proposed as a novel type of light-source, engineered to maximize the brightness of X-ray electromagnetic radiation pulses in the femtosecond time regime. Nowadays, FEL facilities can provide radiation pulses from the THz to the hard X-rays, with repetition rates from a few tens of Hz to MHz, depending on the linear accelerator (linac) energy and technology, i.e. conventional linac versus superconducting linac.
Mostly used as users' facilities, in these last years several FELs facilities have been designed and upgraded to achieve a significant continuous photon energy tunability along with the control of the polarization from linear to circular. This has been the landscape for several years where the FEL designs have been driven by the brightness (peak and average), the transversal coherence (spatial coherence) and the pulse duration. These photon parameters were dictated by science cases where the FELs have been seen as supermicroscopes in the direct space and reciprocal space for imaging nano-objects or performing elastic and scattering experiments respectively, both out of equilibrium.
Nowadays, this paradigm fails when considering other properties of the photon that might be associated with an FEL light pulse. These include, first and foremost, quantum coherence. If this would be possible, one could extend quantum optics, and with them relative spectroscopy, beyond the spectral domain typical of conventional laser systems. Of course, a quantum FEL has been the subject of theoretical studies in recent years. Physics does not preclude quantum FELs from being designed and built, but the stringent properties required for the electron "bunch" are such that they are unrealistic for the time being.
An alternative, to generate quantum coherent light in the extended X-ray spectral range, is to transfer the quantum coherence characteristics of a laser pulse used as a trigger of the FEL process, laser seeded FEL, and test whether theoretically and then experimentally this scheme is realistic or not. In this thesis I try to give an answer, albeit partial, to this question as well.
The purpose of this introduction is also to lay the conceptual and formal foundation for what I will then develop in subsequent chapters. This is in order to make clear the course of study I have followed during my doctorate and, at the same time, to make evident what results, in terms of novelty and scientific merit, I have achieved. Finally, I will give, in the last part of the thesis, a possible realistic scenario and an initial theoretical frame for measuring and controlling quantum states in laser seeded FEL pulses.

1.1 FEL dynamics

Light generation and amplification in free-electron lasers is a nonlinear process developed from the constructive interference of radiation emitted from a bunch of electrons in an undulator. The phenomenon builds up because of a positive feedback: the emission leads to the formation of microbunches (*i.e.* density modulation), that in turn increases the intensity of the former. The "magnetic lattice" of the undulator triggers the emission of photons, while the high-energetic electron beam is the active medium. As we are going to see, the similarities with traditional lasers end here.
One dimensional analysis has the incredible benefit to allow for an analytical formulation of the high-gain FEL dynamics, while still being able to cover most of the fundamental aspects of the process, despite its simplifications. For this reason, we use it as a primer to introduce the main features of FEL dynamics. In the following paragraph, we refer to the notation proposed in [1, 2].
Let us assume that the electrons are traveling along the z-direction through a linearly polarized undulator,

described by the vector potential

$$\boldsymbol{A}_u = A_u(e^{ik_u z}\hat{\boldsymbol{x}} + \text{c.c.}), \quad A_u = \frac{mcK}{e}, \tag{1.1}$$

where m is the electron mass, e is the electron charge, k_u is the wave number of the magnetic field of the undulator and K is the undulator strength parameter. In what follows, we are going to discard the transverse effects such as radiation divergence. The only information about the transverse plane that we are going to keep is the characterization electron motion. Without it, no coupling with the FEL radiation could exist. As a matter of fact, the coupling between electromagnetic fields and electrons is amplified by a factor

$$[JJ] = J_0\left[\frac{K^2}{2(1+K^2)}\right] - J_1\left[\frac{K^2}{2(1+K^2)}\right] \tag{1.2}$$

because of the wiggling path followed by charged particle in the magnetic lattice. In (1.2), $J_n(x)$ are the Bessel functions. In the high-energy approximation, the electron velocity is

$$v_z \approx c\left(1 - \frac{1+K^2}{2\gamma^2}\right) \quad \text{and} \quad \boldsymbol{v}_\perp \approx -\frac{e\boldsymbol{A}_u}{m\gamma}[JJ] \tag{1.3}$$

in which γ is the Lorentz factor. The standard choice for the electron coordinates in this system is given by the so-called electron phase θ

$$\theta = (k_s + k_u)z - \omega_s t \tag{1.4}$$

and longitudinal coordinate $\tau = \omega_u t$ and $k_s = \omega_s/c$ is the wave number of the radiation field. Such phase entails the dependence of the ponderomotive force given by the superposition of the two electromagnetic field. In place of the linear momentum along z, it is customary to use the electron Lorentz factor γ, since $p_z \approx mc^2\gamma$.
The radiation field is decomposed, following the prescription of the slowly varying envelope approximation, into a fast oscillatory factor and a slowly varying one

$$\mathbf{E}(z,t) = \boldsymbol{\epsilon}(z,t)e^{(k_s z - \omega_s t)} + \text{c.c.}, \quad \boldsymbol{\epsilon}(z,t) = \epsilon(z,t)\hat{\mathbf{x}} \tag{1.5}$$

Considering the electromagnetic bath in which the electron bunch is submersed, it is reasonable to assume that also the electron phase space distribution ρ can be written in terms of the slowly varying envelope

$$\rho(z,t,\gamma) = en_0 f(\tau,\theta,\gamma) = en_0\left(F(\tau,\theta,\gamma)e^{i\theta} + \text{c.c.}\right). \tag{1.6}$$

However, since the electron bunch is moving with velocity v_z, the fast modulating term in (1.6), must also be equal to $e^{ik_r(z-v_z t)}$. Hence, to be equal, the following relations have to be satisfied

$$k_r z = (k_s + k_u)z \tag{1.7}$$

$$k_r v_z t = \omega_s t = k_s c t \tag{1.8}$$

which lead to the resonant condition

$$\lambda_s = \frac{2\pi}{k_s} = \frac{\lambda_u}{2\gamma^2}\left(1 + \frac{K^2}{2}\right), \quad \text{with} \quad \lambda_u = \frac{2\pi}{k_u}. \tag{1.9}$$

This wavelength is the only one that, for a fixed energy, will benefit from constructive interference of in-phase wavefront and is, therefore, the FEL emission wavelength. The time evolution of ρ under the effect of the magnetic and radiation fields obeys the Vlasov equation

$$\frac{d}{dt}\rho(z,t,\gamma) = en_0\frac{d}{dt}f(z,t,\gamma) = 0, \tag{1.10}$$

and is coupled to the Maxwell equations for the FEL electric field

$$\left(\frac{d^2}{dz^2} - \frac{1}{c^2}\frac{d^2}{dt^2}\right)\mathbf{E}(z,t) = \mu_0\frac{\partial}{\partial t}\boldsymbol{j}(z,t), \quad \boldsymbol{j}(z,t) = en_0\int d\gamma \boldsymbol{v}_\perp f(z,t,\gamma). \tag{1.11}$$

We can simplify these expressions. Recalling the definition (1.22), in the paraxial approximation, we can write the d'Alembert operator

$$\left(\frac{\partial^2}{\partial z^2} - \frac{1}{c^2}\frac{\partial^2}{\partial t^2}\right) \approx 2ik_s \left(\frac{\partial}{\partial z} + \frac{1}{c}\frac{\partial}{\partial t}\right) \tag{1.12}$$

and recalling equations (1.1), (1.3), (1.6) and the fact that $\partial_t f \approx -i\omega_s f$, we get

$$\left(\frac{\partial}{\partial z} + \frac{1}{c}\frac{\partial}{\partial t}\right)\epsilon(z,t) = \frac{n_0\mu_0 e^2 c A_u}{2m}[JJ]\int \frac{d\gamma}{\gamma}F \tag{1.13}$$

and finally, passing from the coordinates (z,t) to (τ,θ),

$$\left(\frac{\partial}{\partial \tau} + \frac{\partial}{\partial \theta}\right)\epsilon(\tau,\theta) = D_1\int \frac{d\gamma}{\gamma}F(\tau,\theta,\gamma), \quad \text{where} \quad D_1 = \frac{n_0\mu_0 e c^2 K}{\sqrt{2}k_u}[JJ]. \tag{1.14}$$

For simplicity, we assume that the beam is mono-energetic with all electrons having energy γ_0 and velocity $v_z(\gamma_0) = v_0$. In this way we also fix the resonant wavelength and the envelope frequency ω_s. [1, 2]
The Vlasov equation can become tractable once linearized. In fact, it displays a nonlinearity in the last term of the total derivative

$$\frac{\partial f}{\partial t} + v_z(\gamma)\frac{\partial f}{\partial z} + \frac{dp_z(f)}{dt}\frac{\partial f}{\partial p_z} = 0 \tag{1.15}$$

since the momentum is modified by the electromagnetic field, which in turn is dependent on the distribution f itself. The linearized version, instead, reads

$$\frac{\partial f}{\partial t} + v_z(\gamma)\frac{\partial f}{\partial z} + \frac{dp_z(f)}{dt}\frac{\partial f_0}{\partial p_z} = 0 \tag{1.16}$$

where f_0 is the initial electron distribution. In doing so, we are basically neglecting the development of energy spread due to the interaction with the radiation field. Passing from p_z to γ,

$$\frac{dp_z}{dt} = \frac{d}{dt}mc^2\gamma = e\boldsymbol{v}_\perp \cdot \boldsymbol{E} = -\frac{e^2c^2A_u[JJ]}{\gamma}\epsilon(z,t)e^{i\theta}, \tag{1.17}$$

and using the new coordinates (τ,θ), gives

$$\left[\frac{\partial}{\partial \tau} + \eta\left(\frac{\partial}{\partial \theta} + i\right)\right]F = D_2\frac{1}{\gamma}\frac{df_0}{d\gamma}\epsilon \tag{1.18}$$

$$D_2 = \frac{eK}{2\sqrt{2}mc^2k_u}[JJ] \tag{1.19}$$

$$\eta = \frac{v_z(\gamma) - v_0}{c - v_0} = 1 - \frac{\gamma_0^2}{\gamma^2} \tag{1.20}$$

For an initial uniform and mono-energetic distribution $f_0 = \delta(\gamma - \gamma_0)$ and no radiation field for $\tau = 0$, these equations can be solved analytically. To do so, together with the new set of electron variables (τ,θ), we can introduce the corresponding Fourier transform over θ and Laplace transform over τ

$$\bar{g}(\Omega,q) = \int d\tau \int d\theta g(\tau,\theta)\exp\{i\left(\Omega\tau - q\theta\right)\} = \int d\tau \tilde{g}(\tau,q)\exp\{i(\Omega\tau)\}, \quad \Omega \in \mathbb{C}, \quad q \in \mathbb{R} \tag{1.21}$$

The fact that the distribution is modulated at a wavelength resonant with the radiation field implies that $\hat{E}$ and $\hat{F}$ are proportional to $\delta(q)$, so that there is no detuning. Fourier-Laplace transform leads to a cubic equation in Ω and roots of such equation are the poles around which we integrate when we anti-transform back the solution to the space coordinates. [1, 2]
The solution reads

$$E(\tau) = \frac{iD_1}{3\gamma_0^3}\sum_{j=1}^{3}\frac{e^{-i\Omega_j}}{\omega_j}\int d\gamma F(\tau = 0,\gamma) \tag{1.22}$$

where $\Omega_j = 2\rho \exp\{ij2\pi/3\}$ are the roots of the equation

$$\Omega^3 - (2\rho)^3 \approx 0, \quad \text{and} \quad (2\rho)^3 = \frac{2D_1 D_2}{\gamma_0^3}. \tag{1.23}$$

The quantity ρ is called *Pierce parameter* [3]. The cubic equation is obtained by invoking both the mono-energetic condition and the slowly varying envelope approximation for F.
Now, the electric field is proportional to a quantity named *bunching factor*:

$$b \equiv \int d\gamma F = \int d\gamma f e^{-i\theta} = \langle f e^{-i\theta} \rangle \tag{1.24}$$

where the symbol $\langle ... \rangle$ indicates the mean value calculated over an ensemble of particles. The bunching factor determines the mean value of the harmonic content at the resonant wavelength of the electron distribution and it is a measure of the density modulations.
When the FEL process is triggered by the spontaneous emission originated from the granularity, *i.e.* the shot-noise, in the beam, the process is called *Self-Amplified Spontaneous Emission* (SASE) [4–6]. The presence of amplification is granted because there is always one root of the cubic equation that leads to an exponential growth of the electric field.
The stochasticity of the shot-noise in the bunch is the dominant mechanism that determines the photon statistics in a SASE FEL, together with the gain. For this reason, these sources are not lasers at all [7], in the strict sense of the term, since the process is purely traceable to classical electrodynamics, while the high spatial coherence is due solely to the spatial dimension of the radiation source, *i.e.* electrons bunch, and the structure of the ultrashort light pulse results from the propagation of appropriately controlled behavior of the electron bunches during the acceleration process in the linac. SASE FEL dynamics is closer to that of super-fluorescent emission [7].
In other words, these are predominantly thermal light sources that have little to do with the radiation produced by a stimulated emission process with population inversion in a resonant optical cavity that determines the quantum nature of the laser emission. This fact is confirmed by interference experiments, at the first and second order of longitudinal (time) coherence, where the degree of classical coherence is broadly compatible with that of light sources predominantly thermal [8].

1.2 External seeding and coherence

Over time, however, other solutions have been proposed to trigger the FEL process, the most notable of which is the externally seeded operation mode. An external infrared laser can be used to imprint an energy modulation that is then translated into a density modulation. [1, 2] The interaction between electrons and laser is enhanced by the used of a dedicated undulator, called a *modulator*. The bunching factor accumulated in this way, is used as the starting condition for the real FEL process, since this bunched beam is then injected into a second undulator. This standard setup is called high-gain harmonic generation (HGHG).A comparison of SASE and HGHG schemes is shown in Fig. 1.1.

From the mathematical point of view, we start from a Gaussian energy distribution in the energy with energy spread σ_γ

$$f_0(\gamma - \gamma_0) = \frac{1}{\sqrt{2\pi}\sigma_\gamma} e^{-(\gamma-\gamma_0)^2/2\sigma_\gamma^2}. \tag{1.25}$$

After the modulator, the energy distribution of the beam is given by

$$f_0(\gamma - \gamma_0 - \Delta\gamma \sin\theta) \tag{1.26}$$

where $\Delta\gamma$ is the amplitude of the energy modulation acquired from the interaction with the laser. The phase after the dispersive section is shifted by a factor proportional to the dispersion strength $d\theta/d\gamma$, and the distribution at the entrance of the undulator is, therefore,

$$f(\theta, \gamma) = f_0 \left[\gamma - \gamma_0 - \Delta\gamma \sin\left(\theta - \theta_0 - \frac{d\theta}{d\gamma}(\gamma - \gamma_0) \right) \right] \tag{1.27}$$

Thus, the bunching factor at the $n-th$ harmonic, using the definition (1.24), can be estimated

$$b_n = \exp\left\{ -\frac{1}{2} n^2 \sigma_\gamma^2 \left(\frac{d\theta}{d\gamma} \right)^2 \right\} J_n \left(n\Delta\gamma \frac{d\theta}{d\gamma} \right). \tag{1.28}$$

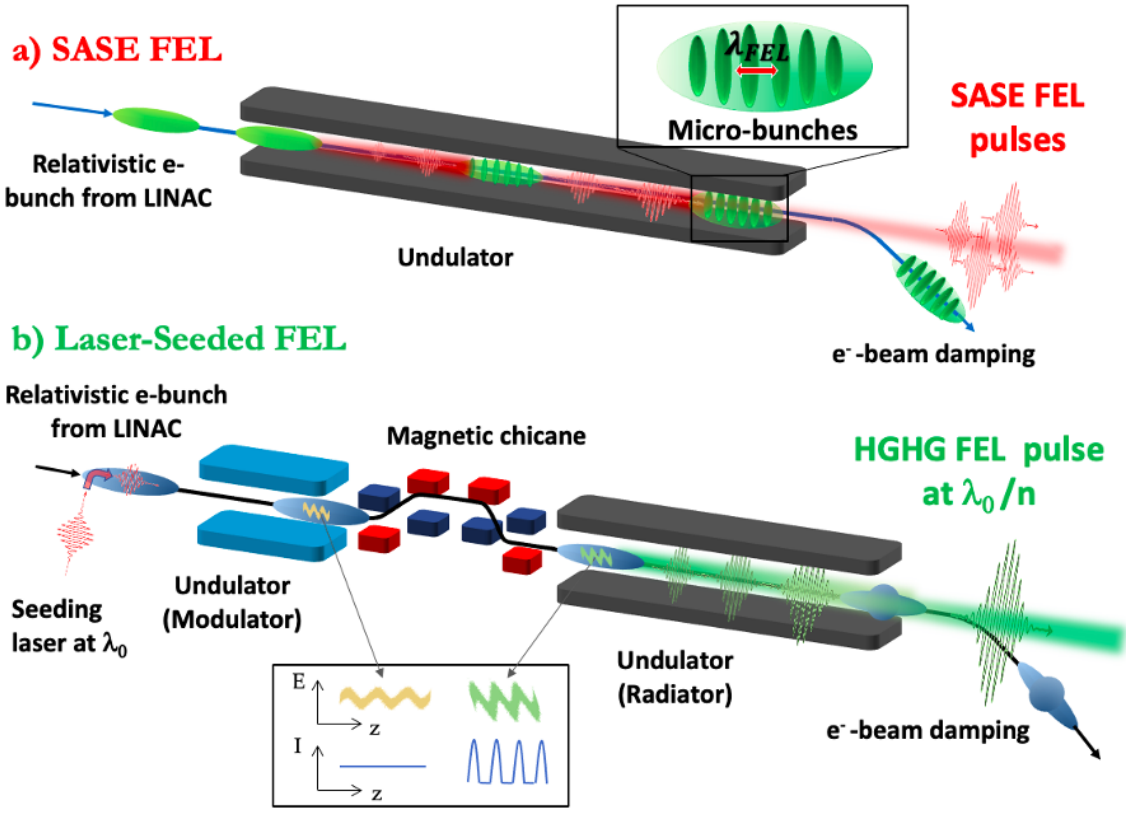

Figure 1.1: SASE and externally seeded FELs configurations. Image from [9]

This strategy, however, brings some novelties. The spectral behavior is now dominated by the coherence of the laser and the emission is an harmonic of the seed laser wavelength. Thus, externally seeded FELs could gain another figure of merit: **temporal coherence**. The first indication of temporal coherence is given by the coherence time. It is usually accessed via phase correlation measurements, typically in double slits interference setup and gives the time interval in which the wave fronts of the source are in phase. This is, however, just a single mono-dimensional index that cannot entail the whole concept of coherence. For this reason, higher order degree of coherence, described in terms of correlation functions, are measured to quantify the stochasticity of a source. Second order correlations, *i.e.* intensity correlation, already carries a plethora of new information to be deduced. A complete survey of the theory of coherence and correlation function is presented in the next chapter.

As for the case of high harmonic generation (HHG) in gas, this is another technique that exemplifies the transmission of coherence through matter via harmonic conversion. Needless to say that this innovation was again dictated also by science cases: some attention has been shifted to spectroscopy and non-linear scattering studies where the average brightness and the longitudinal coherence become photon parameters of paramount importance.

The first realization of HGHG in the XUV was achieved at FERMI at Elettra [10, 11] (see also Appendix A). The strengths of the FERMI light source include on polarization tunability, phase control and the high degree of coherence. While the former is due to the specific choice of the undulators, the others are properties inherited from or controlled by the seed laser.

The main obstacle to the preservation of coherence and its extension to shorter wavelength is also inherent to the gain and the gain medium, *i.e.* the electron bunches. Inhomogeneities in the energy and density distributions of the electron beam result in the accumulation of spurious radiation that decrease the phase stability and, overall, the degree of coherence of FELs. All the modulations that fall inside the gain bandwidth and, as a consequence are enhanced by the FEL mechanism, are in fact source terms for radiation. Let us consider for simplicity a two-frequency system, in which the first is the laser one and the other is due to the spurious modulations [12]. In this setup, the electric field will therefore exhibit two terms: one the expression presented in (1.22) and the other is going to be proportional to the amplitude of the spurious

modulations in the electron beam.
We define A_m to be the amplitude of the energy modulation of the beam at wavelength $\omega_m = \Delta\nu\omega_s$, where $\Delta\nu$ is smaller than ρ. Under this condition the sideband frequency is still included in the FEL gain bandwidth. We also introduce b_m, the bunching factor at ω_m

$$b_m = \langle e^{-i\Delta\nu\theta} \rangle. \tag{1.29}$$

We are going to treat these terms as perturbation to the main radiation fields.
It is possible to demonstrate that the spurious electric field is proportional to [12]

$$\epsilon_m(\tau) \approx -\frac{i}{3}\left(A_m + e^{2\pi i/3} b_m\right) \tau\epsilon(\tau). \tag{1.30}$$

The development of a second contribution to the total field compete with the growth of the main FEL radiation mode, resulting in the reduction of the bunching factor at the seed wavelength and the appearance of sideband in the spectrum. The latter is the cause of the deterioration of the spectral purity, leading to the reduction of temporal coherence, given the departure from monochromaticity of the field.
The collective phenomenon that results on the accumulation of these modulations is called the *microbunching instability* [13]. This instability has been observed at a number of facilities, using various techniques, and some of them are reported in the third chapter, together with a comprehensive modeling of the electrons phase space evolution. All that considered, it becomes vital to understand the mechanism underlying the development of microbunching instability to avoid the loss of coherence.
While the inheritance of coherence in a classical sense is an established fact, very little could be said about quantum coherence. This aspect was in fact ignored, except in the case of purely theoretical studies to realize quantum FELs [14–17] or in the case where the FEL photon energy allowed the process of light emission to be realized in a resonant optical cavity [18]. In the latter case, the FEL radiation can be generated in a resonant optical cavity only for photons with energy compatible with the maximum energy gap of the mirrors insulating materials of the resonant cavity, *i.e.* $\sim$ 11 eV for alkali metal fluorides.
However, for photon energies from near-IR to those achievable by non-perturbative highly non-linear optical processes, like High Harmonic Generation (HHG), the realization of expensive and complex sources, such as FELs has no tangible advantages over conventional laser sources, except for radiation in the THz regime, where the intensity of FEL pulses can be order of magnitude brighter respect to laser based nonlinear optical processes needed to achieve ultrashort terahertz radiation in the $\sim$ 1-20 THz frequency range. In this case, the FEL radiation produced in a resonant cavity (under the right conditions) could have the quantum characteristics satisfying the statistical criteria defining the Glauber coherent states [18].
However, photon statistics experiments for these light sources do not exist, to the best of my knowledge, and so even in this case, although quantum coherent states may be plausible, they are not demonstrated yet. Of course, the question is not only an experimental curiosity, but overall a problem relevant to the physics of the laser process, which can lead to a definitive answer to the question of whether the quantum nature of the laser light is exclusively determined by a quantum process such as population inversion and stimulated emission in an optical resonant cavity.

1.3 About this thesis

The aim of my research is the study of the classical and quantum longitudinal coherence of seeded FEL. The focus is on the role of the electron dynamics and the mechanisms that can affect the first and second order coherence, i.e. classical phase coherence and intensity correlation measurements.
Although there is direct evidence that the radiation from FERMI FELs shows a longitudinal coherence much superior to SASE FELs [19, 20], the physics of the electron bunch dynamics is of paramount importance to control, preserve and improve this property. Nevertheless, completely coherent light requires the measure of the degree of coherence at any order. This was still missed. Here I treat also this topic and the results are given as the last part of this work.
The rest of the thesis is divided in three chapters. The next chapter is devoted to the characterization of the classical transverse and temporal coherence of seeded FELs. After introducing the concepts necessary to understand the theory at the base of the whole manuscript, namely first- and second-order degree of coherence, the results for one of the seeded FEL lines at FERMI are shown. One of the sections presents a comparison (the first ever reported in literature) of the development of first-order transverse coherence

between SASE and seeded FELs. Young double slits interference is measured as a function of the distance between the slits, comparing how the spatial coherence is evolving along a chain of undulator magnets. The consistency of the comparison is granted by the fact that the same beamline has been used, at the same wavelength and using the same electron beam condition.
The second section is focused on the second-order longitudinal coherence of non-linear harmonics generated by seeded FELs. The second order correlation function that we measure for wavelengths in the water window confirms the expected high degree of coherence inherited from the laser seed pulse.
I have taken part to the revision of the results concerning the transverse coherence and I had a major role in the measurements and the analysis of longitudinal coherence.
The quoted sentences in this chapter are reduced from references [20, 21] that I have coauthored.

The third chapter focuses the attention on microbunching instability as a possible cause of decoherence in seeded FELs. This is a cascade instability originated from electron shot noise and amplified along the linac. Its impact on FEL dynamics is predicted theoretically and benchmarked experimentally measuring spectral intensity distribution and brilliance of the light pulses. Actually, the inclusion of momenta diffusion due to multiple small angle scattering in the electron phase space is the breakthrough in our theory.
Direct evidence of microbunching instability are presented: we developed a 2-D Fourier analysis of the phase space and we commissioned a new infrared spectrometer at FERMI facility.
I developed the theory presented here and the code used for the simulations showed along the chapter, including the comparison with the energy spread measurement and the characterization of the FEL spectral impurity. I was involved in the data analysis and elaboration of the theory for the 2-D Fourier technique and the HGHG FEL spectral behavior. I have also taken part to the commissioning of the infrared spectrometer, collecting and analyzing the data presented here.
The quoted sentences in this chapter are reduced from references [22–29] that I have coauthored or where I am the first author.

The last chapter develops the concept of FEL quantum coherence by introducing the quantum nature of photon correlation and anti-correlation. Major emphasis has been put on the, sometimes subtle, differences that occur between classical and quantum nature of correlation. A brief survey of the quantum states of light and their representation is inserted before presenting our results.
We exploited a technique of photon population retrieval, already applied in the optical regime for laser-like and incoherent photon statistics, for FEL radiation. The great advantage is that the information retrieved by this technique is complementary to the information given by correlation functions.
The basic idea is that off-click counts from a non-ideal Geiger detector generate a statistics. This distribution is the input for a maximum-likelihood extimation of the most probable photon state that reproduces such statistics. The possibility to extend the algorithm to a higher number of photons is demonstrated via simulations for FEL-like states.
Finally, we tackled the fundamental problem of a free electron interacting with a quantized monochromatic field. Despite the apparent simplicity of the problem, the answers are still unsatisfactory.
We derived a generalized formalism for solving the Dirac equation in an external electromagnetic field for a generic initial condition for both light and electron. The derivation is commented along with our interpretation of the dressed electron state and the so-called Volkov ansatz. This last chapter is a primer for a larger project: the investigation of transmission of quantum coherence from light to matter and from matter to light.
My contributions consist in the development of the code for the algorithm and the generation of the data, together with the interpretation of its output and performances. I am one of the three main investigators of the Dirac-Volkov equation, I proposed the overall physical interpretation and I conducted most of the calculations presented in this chapter.
The quoted sentences in this chapter are reduced from references [9] that I have coauthored.

Chapter 2

Classical Coherence

Coherence is the property that determines the stability of the relative phase between waves at two different points, whether they are in space or time. An ideal coherent radiation source produces fields with exactly the same spectral properties. In this sense, it is a measure of similarity between fields. As a consequence, coherence is also a way to quantify the insurgence of interference, keeping in mind that any interferometer is a physical correlator.
As already anticipated, correlations can be measured both in time (or wavelength) and space, discriminating in this way between temporal and spatial coherence.
In what follows, we are going to focus on first and second order degree of coherence of light and the corresponding correlation functions. We present two experimental setups to measure coherence of light and from there we derive the expressions to quantify the degree of coherence and the correlation functions. This machinery is then applied to characterize correlations of some classical fields, namely, chaotic light and laser, underlining their main features and the behavior of their correlation functions. In the last part, we show some experimental results of the measurement of transverse and longitudinal coherences of SASE and seeded FELs. For the latter, I was directly involved in the measurement and I took care of the data analysis and interpretation of the results.

2.1 Classical theory of coherence

2.1.1 Phase correlation

Interferometers are designed to demonstrate and study interference. Young's two-slit interferometer [30–33] is the prototype of these instruments and it works with both fermions and bosons. There are however other schemes, such as Mach-Zender and Michelson interferometers [30–33] that are mostly suited for detection of interference of non-massive particles because of the exploitation of a beam splitter. Generally, speaking all these setups are designed to obtain a superposition of fields allowing to study the coherence of both classical and quantum states of light.
All these interferometers are "phase correlators". In fact, they return a measurement of correlation between fields at different point in space or time providing information about their relative phase. For all these reasosn, the quantitative measurements performed with these types of interferometers are used to characterize the so called first-order coherence.
The linear superposition of equally polarized fields is given by

$$E(x) = \delta_1 E(x_1) + \delta_2 E(x_2) \tag{2.1}$$

where $x = (t, \mathbf{x})$ is the four-dimensional position vector, x_i are considered at the time $t_i = t - s_i/c$ and δ_i are geometric factors that depend on the distances s_i.
Light detectors in the optical frequency regime measure the average light intensity,

$$I(\mathbf{x}) = \langle |E(x)|^2 \rangle, \quad \text{where} \quad \langle f(t) \rangle = \lim_{T\to\infty} \frac{1}{T}. \int_0^T f(t)dt \tag{2.2}$$

Assuming the ergodic hypothesis, the time average is equivalent to an ensemble average. At the first electric field order the normalized mutual coherence or correlation function is defined as

$$\gamma^{(1)}(x_1, x_2) = \frac{\langle E^*(x_1)E(x_2)\rangle}{\sqrt{\langle|E(x_1)|^2\rangle\langle|E(x_2)|^2\rangle}}. \tag{2.3}$$

Hence Eq. (2.3) determines the correlations between the field amplitudes relative to the magnitudes of the uncorrelated amplitudes, and satisfies the condition $0 \leq |\gamma^{(1)}(x_1, x_2)| \leq 1$. This is consistent with the idea that a phase interferometer must keep track of the phase differences of electric fields.
To simplify the next discussion, we assume that δ_1 and δ_2 have the same modulus δ, which is the case of identical optical beams so that we can express the normalized first-order correlation function as

$$\gamma^{(1)}(x_1, x_2) = |\gamma^{(1)}(x_1, x_2)| \exp\{[i\alpha(x_1, x_2)]\}. \tag{2.4}$$

The interference pattern can be measured via the fringe visibility

$$C = \frac{I_{\text{max}} - I_{\text{min}}}{I_{\text{max}} + I_{\text{min}}}, \tag{2.5}$$

where I_{max} and I_{min} are the maximum and minimum intensity in the interference pattern respectively, so that

$$C = \frac{2\sqrt{(I_1 I_2)}}{I_1 + I_2}|\gamma^{(1)}(x_1, x_2)|. \tag{2.6}$$

The normalized correlation function is also known as the degree of coherence, since it can be used to discriminate between the three types of coherence: when $|\gamma^{(1)}(x_1, x_2)| = 1$, the coherence is complete and the time average can be factorized, *i.e.*

$$\langle E^*(x_1)E(x_2)\rangle = \langle E^*(x_1)\rangle\langle E(x_2)\rangle. \tag{2.7}$$

The visibility of the fringes is maximized in this case. The intermediate values of the correlation function, *i.e.* $(0 < |\gamma^{(1)}(x_1, x_2)| < 1)$, characterize a partial correlation (coherence) between the fields. In both cases, the interference is present. Finally, for $|\gamma^{(1)}(x_1, x_2)| = 0$, the visibility is 0 and the field is completely incoherent.

2.1.2 Intensity correlation

Phase interferometry, despite the possibility to retrieve the coherence length, and, more generally to which extent a generic light source tends to monochromaticity, i.e. to a single frequency wave, cannot provide information about the statistical behavior of light. First-order coherence may be understood mathematically as the result of the factorization of the expectation values in the correlation function of the fields. That is, first-order coherence experiments are unable to distinguish between states of light with identical spectral distributions but with quite different photon number distributions [32, 33].
For this reason the characterization of the correlation of intensities rather than phase, as for the Hanbury Brown and Twiss experiment is of paramount importance [30–34]. Correlation of intensities correspond to the delayed coincidence rate obtained from two light detectors from which the statistics of the beam could be determined, if the delay is larger than the coherence time of the source. The probability of obtaining coincident events when the detectors are at different distances from the sources and with a delay $\tau = |t_2 - t_1|$, is

$$\gamma^{(2)}(x_1, x_2; x_2, x_1) = \frac{\langle I(x_1)I(x_2)\rangle}{\langle I(x_1)\rangle\langle I(x_2)\rangle} = \frac{\langle E^*(x_1)E^*(x_2)E(x_2)E(x_1)\rangle}{\langle|E(x_1)|^2\rangle\langle|E(x_2)|^2\rangle} \tag{2.8}$$

Equation (2.8) is the classical second-order coherence function. Dealing with intensities means that we are working with quantities proportional to the square modulus of the fields, hence the name. By analogy to first-order coherence, the second-order classical coherence is given by $|\gamma^{(1)}(x_1, x_2)| = 1$ and $\gamma^{(2)}(x_1, x_2; x_2, x_1) = 1$. The last equality corresponds to the factorization condition for the intensities

$$\langle E^*(x_1)E^*(x_2)E(x_2)E(x_1)\rangle = \langle|E(x_1)|^2\rangle\langle|E(x_2)|^2\rangle, \tag{2.9}$$

in analogy to the complete coherence condition for the first correlation function. However, the second-order coherence function is not restricted to be less than 1, as for the first order one. To prove this, let us consider

the case where there is no delay and the distance of the detectors from the source is the same. In this configuration, we have

$$\gamma^{(2)}(0) = \frac{\langle I^2(t)\rangle}{\langle I(t)\rangle^2}, \tag{2.10}$$

which is always equal or more than 1, because of Cauchy's inequality. There is no way to establish an upper limit, thus

$$1 \leq \gamma^{(2)}(0) < \infty \tag{2.11}$$

For nonzero time delays, instead,

$$0 \leq \gamma^{(2)}(\tau) < \infty \quad \text{and} \quad \gamma^{(2)}(\tau) < \gamma^{(2)}(0), \tag{2.12}$$

and this is always true for classical fields. Analogously to what we have done for the visibility at first order, we can define a visibility of the pattern in intensity correlation,

$$C^{(2)} = \frac{2\langle I_1 I_2\rangle}{\langle (I_1 + I_2)^2\rangle}. \tag{2.13}$$

Based on this definition, we see that the maximum visibility interference pattern in the intensity correlation is equal to $1/2$, contrary to the first order case. Although the properties derived here are true for temporal coherence, the same arguments can be applied to the study of transverse coherence, leading to the same results.

2.2 Spatial and Temporal coherence

For a physical beam, the propagation of a spatially extended wavefront requires to introduce two quantities, namely the coherence length l_c and the coherence time τ_c that characterize respectively the space and time scale at which the interference is observed. These quantities are usually expressed as a function of the source bandwidth $\Delta\omega$ and, in particular, $l_c = c/\Delta\omega$ and $\tau_c = l_c/c = 1/\Delta\omega$ [30–33]. However, the spatial (or transverse) coherence and the temporal (or longitudinal) coherence, differ significantly since the temporal coherence is related to the process that generates the light, whereas the spatial coherence is related to the size of the source. In the limit of point-size sources the light is fully spatially coherent. Finally, when the electromagnetic field is not simply emitted but also amplified, coherence is no longer an intrinsic property of the source, but strongly depends on the amplification process.

For a source with a finite dimension to generate transversally coherent radiation, the effective radiation size and the source's dimension should match. In this condition, a light source is said to be at diffraction limit. For instance, this is closed to be realized in fourth generation synchrotron radiation storage ring, where the electron beam emittances are designed to match the emitted photon beam spot size [35, 36]. During amplification or with dedicated tools (when available), transverse coherence can be improved via mode-selection, leading to the selection of a single transverse mode.

Temporal coherence and coherence time, on the other hand, are determined by the emission process. The thermodynamic and statistical behaviors of the emitters are imprinted into field's phase and intensity. Analysis of longitudinal coherence, therefore, can be considered as a probe of the mechanism of light emission [37]. For this reason, longitudinal coherence cannot be achieved by any form of mode selection, even when the gain spectrum of the amplification is narrowed. In fact, according to the Wiener-Khintchine theorem [38], spectral density $F(\omega)$ and first-order correlation function are related by

$$F(\omega) = \frac{1}{\pi}\,\mathrm{Re}\left[\mathcal{F}[\gamma^{(1)}(\tau)]\right] = \frac{1}{\pi}\,\mathrm{Re}\left[\int_0^\infty \gamma^{(1)}(\tau) e^{i\omega\tau} d\tau\right]. \tag{2.14}$$

Narrower spectra correspond to the tendency towards first-order longitudinally coherent pulse with longer coherence time. However, as we have seen before, the proximity or the achievement of phase stability is not enough to ensure longitudinal coherence. This is exactly what a high-order degree of coherence can discriminate. If a process that controls intensity fluctuations of the field existed, it would be the mandatory step to reach temporal coherence. In some sense, harmonic conversion is the closest mechanism to such an ideal process.

Finally, despite their differences, longitudinal and transverse coherence are not completely independent from each other. In particular, a finite size source will affect the longitudinal and transversal coherence in an intertwined way difficult to be disentangled in the interference pattern.

2.3 Classical fields

In this section we present two paradigmatic examples of classical light, computing their first and second order correlation functions. We limit ourselves to consider the temporal coherence for simplicity, knowing that the same formalism can be applied also to transverse coherence.

Monochromatic field A monochromatic unpolarized light is a plane wave of the form

$$E(\mathbf{r},t) = E_0 e^{i(\mathbf{k}\cdot\mathbf{r}-\omega t)} \tag{2.15}$$

which is completely characterized by its frequency ω and wave vector $\mathbf{k} = \omega\hat{\mathbf{k}}/c$. Since we are interest in the temporal coherence, we can drop the spatial dependence of the field and write the mutual correlation function as

$$\gamma^{(1)}(\tau) = \frac{\langle E^*(t)E(t+\tau)\rangle}{\sqrt{\langle|E(t)|^2\rangle\langle|E(t+\tau)|^2\rangle}} = e^{-i\omega\tau} \tag{2.16}$$

and thus $|\gamma^{(1)}(\tau)| = 1$, meaning that the source is perfectly coherent in time at first order.
The same holds for the second order correlation function and for all the higher order correlation functions. Starting from the definition of $\gamma^{(2)}$,

$$\gamma^{(2)}(\tau) = \frac{\langle E^*(t)E^*(t+\tau)E(t+\tau)E(t)\rangle}{\langle|E(t)|^2\rangle\langle|E(t+\tau)|^2\rangle} = 1 \tag{2.17}$$

and considering that the numerator is always independent on t hence, the mean value can be factorized. This is a consequence of the constancy of the intensity of a plane wave field. This fact is verified whenever the electric field of a plane wave is multiplied by its complex conjugate and can be applied to any power of the electric field. Thanks to this consideration, we can generalize the previous result to any order n, leading to the condition

$$\gamma^{(n)}(\tau) = 1, \quad \forall n > 1 \tag{2.18}$$

Monochromatic light is coherent at each order both in time and space. This is sometimes referred as the Glauber necessary conditions for complete coherence [39].

Chaotic light Let us consider a field

$$E(\mathbf{r},t) = E_0 e^{i(\mathbf{k}\cdot\mathbf{r}-\omega t)} e^{i\phi(t/\tau_0)} \tag{2.19}$$

where $\phi(t/\tau_0)$ is an additional phase introduced to take into account the process that generates the electromagnetic field. Generally speaking, any form of random process that leads to the emission of light is characterized by a characteristic time τ_0. The functional dependence of ϕ on time must also depend on this characteristic time. Because of the stochasticity of the radiation process, this type of light is termed *chaotic*.
The main feature of chaotic light is the broadening of its spectrum, *i.e.* the spread in the emission frequencies. As a matter of fact, for a field like (2.19), its frequency is no longer fixed in time as in the previous case, but can be defined as

$$\omega_0(t) = \frac{i}{E(\mathbf{r},t)}\frac{\partial}{\partial t}E(\mathbf{r},t) = \omega - \frac{d\phi}{dt} = \omega - \frac{1}{\tau_0}\frac{d\phi(u)}{du}, \tag{2.20}$$

where $u = t/\tau_0$. If the phase is a constant or is linear in t, this relation simplifies and we retrieve the case of a monochromatic field. Otherwise, the emission lineshape is always broader.
The first order correlation function for this kind of field is

$$\gamma^{(1)}(\tau) = e^{-i\omega\tau}\left\langle \exp\left\{ i\left[\phi\left(\frac{t+\tau}{\tau_0}\right) - \phi\left(\frac{t}{\tau_0}\right)\right]\right\}\right\rangle. \tag{2.21}$$

Assuming that ϕ is a smooth function $\forall t$ then, invoking Lagrange's theorem,

$$\phi\left(\frac{t+\tau}{\tau_0}\right) - \phi\left(\frac{t}{\tau_0}\right) = \frac{\tau}{\tau_0}\left.\frac{d\phi(u)}{du}\right|_{u=u_0} \tag{2.22}$$

where $u_0 \in (t, t+\tau)/\tau_0$. Notice that u_0 depends on t and has to be defined for each interval. If we assume that τ/τ_0 is small enough such that the choice of u_0 is independent from t, the derivative is no longer t-dependent. As a consequence, the correlation function is equal to

$$\gamma^{(1)}(\tau) = e^{-i\omega\tau} \exp\left\{ i\frac{\tau}{\tau_0} \frac{d\phi(u)}{du}\bigg|_{u=u_0} \right\} = e^{i\omega_0(u_0\tau_0)} = e^{i\omega_0(t_0)}, \quad t_0 = u_0\tau_0 \tag{2.23}$$

showing that the light is still coherent. Of course, this is true only for very small values of τ/τ_0 and it is no longer verified if the delay is larger than the characteristic time. When $\tau > \tau_0$, the mean value of the phase in eq. (2.21) tends to zero and so does the modulus of the correlation function. This means that outside of the temporal window specified by τ_0, the field is incoherent. For this reason, the characteristic time of the random process, τ_0, and the coherence time of the field, τ_c, coincides. Finally, for $\tau = 0$, $|\gamma^{(1)}(0)| = 1$.
A more general expression to characterize the degree of coherence is found assuming only that $\tau \ll \tau_0$, and reads

$$\gamma^{(1)}(\tau) \approx e^{-i\omega\tau} \frac{1}{T} \int_0^T \exp\left\{ i\tau \frac{d\phi(t/\tau_0)}{dt} \right\} dt. \tag{2.24}$$

Chaotic light also satisfies a pair of useful relations: the first is

$$\tau_c = \int_{-\infty}^{\infty} d\tau |\gamma^{(1)}(\tau)|^2 \tag{2.25}$$

which becomes a method to determine the coherence time of a source, once the $\gamma^{(1)}(\tau)$ is known; the second one, instead, is a relation between the first and second order correlation function

$$|\gamma^{(2)}(\tau)| \approx 1 + |\gamma^{(1)}(\tau)|. \tag{2.26}$$

The higher is the number of emitters, the better this approximation becomes [32, 33]. As a consequence, since $0 \leq |\gamma^{(1)}(\tau)| \leq 1$,

$$1 \leq \gamma^{(2)}(\tau) \leq 2 \tag{2.27}$$

and, in particular,

$$\gamma^{(2)}(0) = 2. \tag{2.28}$$

2.4 Experimental characterization of FEL coherence

Now that the formalism and properties of coherence of classical fields are established, we can exploit them to interpret and explain the transverse and temporal coherence properties of an FEL operated in two different configurations: SASE and externally seeded.
Both configurations can offer almost perfect transverse coherence, showing a single transverse electric mode near saturation [21], because of the mode-selection that happens during the amplification process. The fundamental difference between these two schemes lies in their longitudinal coherence: the first, since it is an FEL process originating from the noise (therefore from the stochasticity) of the electron bunch, shows a poor temporal coherence and behaves as chaotic light; the second, instead, inherits the longitudinal coherence from the external laser used to pre-bunch and "synchronize" the electrons, introducing a phase stability in the emission and showing an higher degree of longitudinal coherence.
The characterization exposed here refers to FERMI FEL-2 line (see Appendix A). For reliable operation at shorter wavelengths down to the soft-x-ray range, in this line the HGHG scheme has been implemented in a two-stage configuration, using the emission of the first stage to seed the second one [11].

Transverse Coherence In comparing the degree of transverse coherence of seeded and unseeded free electron lasers, phase correlation shows comparable values, when the machine is operated at the same wavelength and with the same electron-beam conditions. What differs significantly is the way in which the coherence is achieved. While in the former case the transverse coherence is inherited from the seed laser, in the latter is established due to the transverse mode selection and maximum coherence is reached well before power saturation [21]. As a matter of fact, during the exponential regime, as the bunch progresses

along the undulators, higher gain modes dominate until the non-linear regime starts. Transverse coherence is reached at this point. Of course, as we explained before, having a diffraction-limited electron source is a necessary condition for transverse coherence [35].
A recent comparison between these operation modes was conducted at FERMI (see Appendix A) [21]. A performant SASE mode at FERMI is usually obtained by an optical klystron in order to boost the bunching (self-) generated during the amplification process [40–42]. The externally seeded scheme used in the comparison is the most common one, called high-gain harmonic generation (HGHG) [2]. In this operation mode, an optical laser is exploited to modulate the bunch at the fundamental wavelength λ_{seed} and its high order harmonics $\lambda_n = \lambda_{\text{seed}}/n$. The energy modulations are converted via dispersion into density modulations. This is the initial bunching that triggers the FEL process when the electrons are injected in the radiator, tuned at a specific harmonic λ_n of the seed laser [10, 11].
To measure the degree of transverse coherence a Young double-slit setup was used. From the interference pattern, in fact, one can find the transverse coherence length. The total degree of coherence can be expressed in terms of the ratio between the transverse coherence length and the transverse radiation size in the x plane at the position of the slits

$$\zeta_x = \frac{1}{\sqrt{1+4/q^2}}, \quad q = \frac{l_{cx}}{\sigma_x} \tag{2.29}$$

where l_{cx} is the coherence length and σ_x is the FEL spot size. The measurements have been performed by progressively tuning the radiator sections to the resonant wavelength, and acquiring, for a given number of active radiator sections, the average output power of around 50 shots and the corresponding interference patterns from different slit separations [21].
In Fig. 2.1, the gain curve and total degree of transverse coherence are shown. The HGHG mode reach

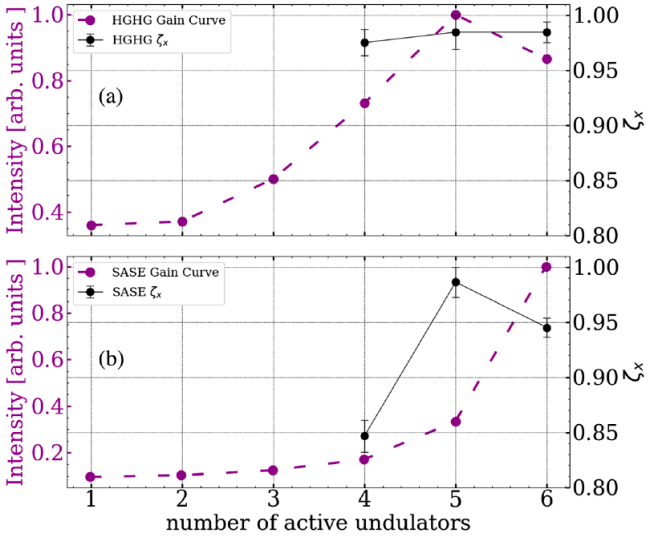

Figure 2.1: Gain curve (purple) and total degree of transverse coherence ζ_x (black) (normalized to unity), as a function of the distance in the second-stage radiator, for (**a**) HGHG and (**b**) SASE. Image from [21]

power saturation before the last radiator module and the total degree of transverse coherence is almost constant and saturates before the intensity. Instead, the FEL did not reach power saturation operating in SASE OK mode and the total degree of transverse coherence reaches maximum value well before intensity saturation. This mismatch in the behavior is a confirmation of the different mechanism that leads to transverse coherence.
Depending on the slit separation Δx, the fringe visibility can be written as

$$|\gamma_{\text{eff}}(\Delta x)| \equiv C(\Delta x) = \exp\left\{-\frac{(\Delta x)^2}{2l_{cx}}\right\} \tag{2.30}$$

where we have introduced the effective degree of coherence. The quantitative comparison for HGHG and SASE in Fig. 2.2, shows that, even if they start from similar values of $|\gamma_{\text{eff}}(\Delta x)|$, increasing the

separation between the slits leads to a clear distinction between the effective degree of transverse coherence. In particular, the HGHG source have higher degree of coherence, thus, a larger coherence length when compared to SASE.

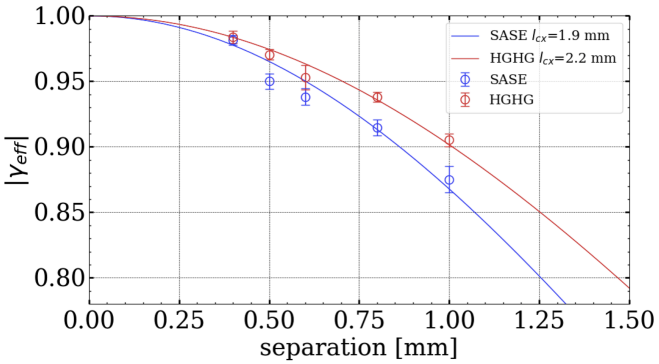

Figure 2.2: The degree of transverse coherence $|\gamma_{eff}|$ as a function of slit separation, for SASE (blue circles) and HGHG (red circles) and the fit for Gaussian decay HGHG (red) and SASE (blue) solid lines providing the transverse coherence lengths. Image from [21]

Longitudinal Coherence "The statistical properties of the light emitted by a seeded FEL differ substantially from those of a SASE FEL source. A SASE FEL has the typical statistics of chaotic light [8, 43], while it was demonstrated that the harmonic conversion and amplification processes preserve part of the coherence properties of the seed laser, even at high harmonic orders, and the seeded FEL statistics resemble those of laser light [19]. As already explained, longitudinal coherence is intrinsic to the emission process:

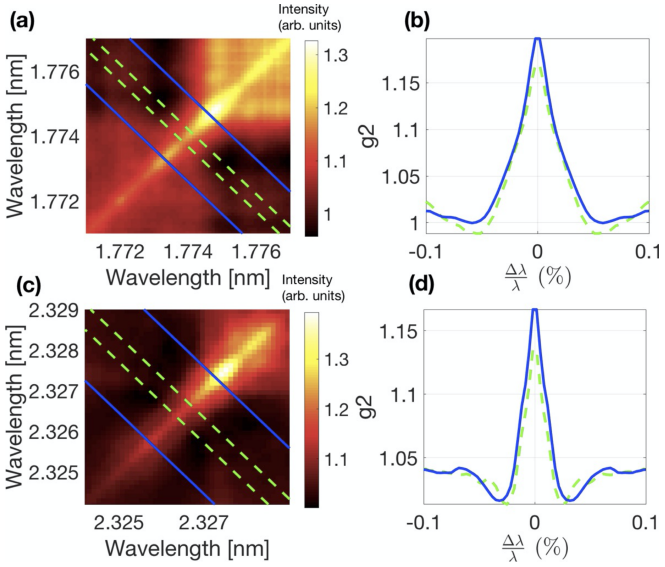

Figure 2.3: Second-order spectral correlation function $\gamma^{(2)}$ for 700 eV (1.77 nm) and 530 eV (2.33 nm) radiation: $(\mathbf{a})$ and $(\mathbf{c})$ shows the whole map defined in Eq. (2.31), while $(\mathbf{b})$ and $(\mathbf{d})$ the mean values of $\gamma^{(2)}$ calculated averaging over a very narrow central bandwidth (green dotted line) and over a larger one (blue solid line). Image from [20]

SASE FELs inherit their thermal behavior from the stochasticity of the electron bunch noise; in seeded FELs, instead, the bunched part of the electron beam, under the effect of the strong laser field, is organized in a phase-locked fashion.
Theoretical studies predict that the frequency multiplication process produces phase noise degradation proportional at least to the square of the frequency multiplication factor [44], preventing full coherence with a HGHG FEL at a very short-wavelength range. To further extend the range toward the water window (up

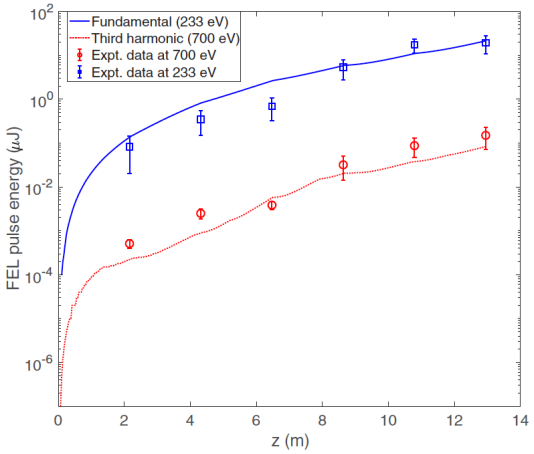

Figure 2.4: Measured (markers) and simulated (lines) FEL gain curves at 233 eV (*i.e.*, 5.3 nm) and at 700 eV (*i.e.*, 1.77 nm). The measurements were done by progressively detuning the undulator gap of the second-stage radiator and by integrating the spectra on two different spectrometers (one for 233 eV and one for 700 eV) within a narrow bandwidth around the central wavelength. Error bars correspond to the standard deviation from the mean value calculated over 50 shots. Image from [20]

to the Oxygen K-edge at 530 eV) and the L-edges of the $3d$ transition metals up to 800 eV, an externally seeded FEL can be operated in the so-called nonlinear harmonic generation (NHG) regime [20, 45–48]. In this regime, the exponential gain leading to the generation of the harmonic λ_n drives the bunching, and consequent emission, at λ_n/m, where m is an integer.
The natural question is what happens to the light statistics of the nonlinear harmonics emitted at very short wavelengths by a seeded FEL and what is the second-order degree of coherence of this spectral component of the emitted light [20]. In the spectral domain, the second-order correlation function corresponds to

$$\gamma^{(2)}(\lambda,\lambda) = \frac{\langle I_1(\lambda) I_2(\lambda)\rangle}{\langle I_1(\lambda)\rangle\langle I_2(\lambda)\rangle} \tag{2.31}$$

where $I(\lambda)$ is the spectrum intensity of a single FEL pulse.
We have used the statistics of the spectra acquired at 700 eV and at 530 eV to calculate the normalized second order correlation function, showing that the high degree of longitudinal coherence, which is imparted by the seed to the light at λ_n in the linear regime, extends also to the nonlinear harmonic λ_n/m. Figure 2.3 reports the $\gamma^{(2)}$ function calculated for the spectra at 1.77 nm (*i.e.*, 700 eV) and at 2.33 nm (*i.e.*, 530 eV), averaged over a very narrow central bandwidth ($\Delta\lambda = 3 \times 10^{-4}$ nm, green line) and a larger one ($\Delta\lambda = 1.5 \times 10^{-3}$ nm, blue line). The value of $\gamma^{(2)}(0)$ ($\sim$1.16) is almost independent of the bandwidth chosen and in both cases the measured value is very close to the typical performance obtained at FERMI in the nominal spectral range (100–4 nm) [19]." From one of my paper [20]
Therefore, the answer to the question is that even in a non-linear process, longitudinal coherence is inherited from the seed pulse and mostly preserved. Of course, as shown in Figure 2.4, this is verified in the gain regime explored with our configuration. Higher gain and saturation, in fact, always deteriorate longitudinal and transverse coherence. The departure from unity can be justified considering the non-negligible presence of microbunching instability in the electron bunch, as shown in the hotter region for longer wavelengths in Figs. 2.3.

2.5 Summary

In this chapter, we showed first- and second-order degree of coherence of FELs. A Young's experiment has been performed to compare the development of transverse coherence in a SASE and seeded FELs. It is demonstrated that in the first case, coherence is builded up during the FEL process, while in the latter the high degree of coherence is inherited from the seed laser pulse. In both cases, the amplification due to high gain is detrimental for transverse coherence and both configurations can achieve a comparable degree

of coherence.
We also measured temporal coherence of non-linear harmonics from a seeded FEL via second-order correlation function. With our analysis, we demonstrated that even in the case of non-linear regime of light emission, longitudinal coherence is transmitted from seeding light to the emitted one and is conserved, as long as the gain is kept low.

2.6 List of publications

- Pop, M., Allaria, E., Curbis, F., Geloni, G., Manfredda, M., Di Mitri, S., Foglia, L., Garzella, D., Giannessi, L., Mahieu, B., Mahne, N., Mirian, N., Penco, G., **Perosa, G.**, Ribic, P.R., Simoncig, A., Spezzani, C., Trovó, M., Werin, S., Zangrando, M. and De Ninno, G., Single-shot transverse coherence in seeded and unseeded free-electron lasers: A com- parison. *Phys. Rev. Accel. Beams* **25**, 040701. (4 Apr. 2022).

- Penco, G., **Perosa, G.**, Allaria, E., Badano, L., Bencivenga, F., Brynes, A. D., Callegari, C., Capotondi, F., Caretta, A., Cinquegrana, P., Dal Zilio, S., Danailov, M. B., De Angelis, D., Demidovich, A., Di Mitri, S., Foglia, L., Gaio , G., Gessini, A., Giannessi, L., Kurdi, G., Manfredda, M., Malvestuto, M., Masciovecchio, C., Mincigrucci, R., Nikolov, I., Pedersoli, E., Pelli Cresi, S., Principi, E., Ribic, P. R., Simoncig, A., Spampinati, S., Spezzani, C., Sottocorona, F., Trovó, M., Zangrando, M., Chardonnet, V., Hennes, M., Luning, J., Vodungbo, B., Bougiatioti, P., Davis, C., Roesner, B., Sacchi, M., Roussel, E., Jal, E. and De Ninno, g., Nonlinear harmonics of a seeded free-electron laser as a coherent and ultrafast probe to investigate matter at the water window and beyond. *Phys. Rev. A* **105**, 053524. (5 May 2022).

Chapter 3

Microbunching Instability

As we have anticipated, spurious harmonic content in the beam becomes detrimental for the FEL coherence. It is, indeed, the main source of its deterioration and, on top of that, it is also the cause of a general worsening of the FEL performance. As matter of fact, modulations and its harmonics that fall inside or near the FEL gain bandwidth contribute to the formation of pedestal and sidebands, deteriorating in this way the pulse energy, the bandwidth and its spectral purity [26, 27, 49–51].
In this chapter, the theoretical and experimental aspects of modulations in the electron beam are presented. The so-called microbunching instability is described from the theoretical point of view, deriving new models that includes also intra-beam scattering. The mathematical apparatus is then used to predict the impact on linac and FEL parameters. The results are benchmarked with direct and indirect measurement of microbunching instability and we propose some novel solutions to counteract the formation of this instability based on our formalism. In particular, we present: measurement of the energy spread that testifies the contribution of both intra-beam scattering and microbunching instability; measurement of FERMI performance in absence and presence of the instability; the commissioning of a diagnostic station for measuring microbunching instability at FERMI and a new technique based on 2-D Fourier analysis.
I personally developed the model that I am going to present and the code that has been used in a series of works dedicated to the estimation of microbunching impact on electrons and FEL dynamics. I partecipated in the commissioning on the new infrared spectrometer in FERMI, collecting all the data showed here. I took part in the analysis of the data for the 2-D Fourier analysis.

3.1 Theory

Microbunching instability (MBI) [13, 52] is the combination of collective phenomena that occur during acceleration, compression and transport of the electron beam and results in the accumulation of broadband energy and density modulations at micron scale.
The instability arises from a cascade process: the self-fields of the electron bunch enhance and convert density modulations into energy modulations and viceversa. More precisely, the electron beam is modulated in energy by the electric field generated by density non-uniformities. In the case of straight section, when the electromagnetic interaction is given by the wake of an electric field, this phenomenon is named Longitudinal Space Charge (LSC) [53]. When, instead, the interaction is mediated by radiation, the self-interaction is termed as a function of the emitted light, as for instance Coherent Synchrotron Radiation (CSR) or Coherent Edge Radiation (CER) [52]. The latter is the case of dispersive section such as magnetic compressors, collimators and transfer lines. The accumulated energy modulations are therefore enhanced but also converted into density modulations in non-isochronous sections.

3.1.1 Huang-Kim model

To model the evolution of density modulations along a dispersive section, and, in particular, along the chicane of a magnetic compressor, we can use the Huang-Kim (HK) formalism [54]. This model relies on the approximated analytical solution of a Vlasov-Maxwell equation for the bunching factor

$$b[k(s);s] = \frac{1}{N}\int d\vec{X}\,\mathrm{e}^{-ikz} f(\vec{X};s), \tag{3.1}$$

defined as the Fourier transform of the phase space distribution $f(\vec{X};s)$ and treating the MBI as a small perturbation of an equilibrium distribution $f_0(\vec{X};s)$.
The evolution can be expressed as an integral equation, after linearizing the Vlasov equation in the perturbative regime in the presence of CSR,

$$b[k(s);s] = b_0[k(s);s] + \int_0^s d\tau K(\tau,s) b[k(\tau);\tau], \tag{3.2}$$

where the kernel of the equation is

$$\begin{aligned} K(\tau,s) = ik(s)R_{56}(\tau\to s)\frac{I(\tau)Z[k(\tau);\tau]}{\gamma I_A}\mathrm{e}^{-k_0^2U^2(s,\tau)\sigma_\delta^2/2}\times \\ \exp\left\{\left[-\frac{k^2(s)\epsilon_0\beta_0}{2}\left(V(s,\tau)-\frac{\alpha_0}{\beta_0}W(s,\tau)\right)^2-\frac{k^2(s)\epsilon_0}{2\beta_0}W^2(s,\tau)\right]\right\} \end{aligned} \tag{3.3}$$

and where k_0 is the modulation wave number at $s=0$, $k(\tau)=B(\tau)k_0$, $B(\tau)=[1+hR_{56}(\tau)]^{-1}$ is the compression factor, $I(\tau)=ecn_0B(\tau)$ is the peak current at τ, I_A is the Alfvén current, $Z[k(\tau);\tau]$ is the CSR impedance and

$$U(s,\tau) = B(s)R_{56}(s) - B(\tau)R_{56}(\tau), \tag{3.4}$$

$$V(s,\tau) = B(s)R_{51}(s) - B(\tau)R_{51}(\tau), \tag{3.5}$$

$$W(s,\tau) = B(s)R_{52}(s) - B(\tau)R_{52}(\tau). \tag{3.6}$$

An approximated analytical solution for the bunching at the end of the chicane can be found by iteration, neglecting the microbunching induced by energy modulation in the same dipole, i.e. considering staged amplification from one dipole to another. The problem reduces to the determination of the following terms

$$\begin{aligned} b[k(s_3);s_3] = b_0[k(s_3);s_3] + \int_0^{L_b} ds_1 K(s_1,s_3)b[k(s_1);s_1] + \int_0^{2L_b} ds_2 K(s_2,s_3)b[k(s_2);s_2] + \\ + \int_0^{2L_b} ds_2 K(s_2,s_3)\int_0^{L_b} ds_1 K(s_1,s_2)b[k(s_1);s_1] \end{aligned} \tag{3.7}$$

where s_j is the coordinate inside the jth dipole. Transfer functions are

$$\begin{aligned} &R_{51}(s_1) = \frac{s_1}{\rho_0}, \quad R_{52}(s_1) = \frac{s_1^2}{2\rho_0}, \quad R_{56}(s_1) = \frac{s_1^3}{6\rho_0^2}, \\ &R_{51}(s_2) = \frac{L_b - s_2}{\rho_0}, \quad R_{52}(s_2) \approx \frac{\Delta L s_2}{\rho_0}, \quad R_{56}(s2) \approx -\frac{\Delta L L_b}{\rho^2}s_2, \\ &R_{51}(s_3) = -\frac{L_b - s_3}{\rho_0}, \quad R_{52}(s_3) \approx \frac{2\Delta L L_b(s_3 - L_b)}{\rho_0}, \quad R_{56}(s_3) \approx -\frac{2\Delta L L_b^2}{\rho^2} \equiv R_{56} \\ &R_{56}(s_1\to s_2) \approx -\frac{\Delta L}{\rho^2}(L_b - s_1)s_2, \quad R_{56}(s_2\to s_3) \approx -\frac{\Delta L}{\rho^2}(2L_b - s_2)s_3, \\ &R_{56}(s_1\to s_3) \approx -\frac{2\Delta L}{\rho^2}[(L_b - s_1)L_b + s_1 s_3]. \end{aligned} \tag{3.8}$$

In absence of coherent synchrotron radiation (CSR), the bunching degradation is

$$b_0[k(s);s] = b_0[k_0;0]\mathrm{e}^{-k^2(s)R_{56}^2(s)\sigma_\delta^2(s)/2}\exp\left\{\left[-\frac{k^2(s)\epsilon_0\beta_0}{2}\left(R_{51}(s)-\frac{\alpha_0}{\beta_0}R_{52}(s)\right)^2-\frac{k^2(s)\epsilon_0}{2\beta_0}R_{52}^2(s)\right]\right\}. \tag{3.9}$$

The exponential term coincides with the Fourier transform of the equilibrium distribution evolved along a dispersive section and is called Landau Damping. As the name suggests, it is a term that encapsulates the natural suppression of the MBI. This process of de-synchronization that counteracts the amplification of the instability is originated from the path difference of particles with different energy, momentum and position in a dispersive section.

3.1.2 Bosch-Kleman model

The beam harmonic content can be obtained also following the Bosch-Kleman (BK) formalism [55]. Differently from the HK model, whose results are derived for magnetic bunch length compressors only, the BK allows the description of MBI in linear regime along dispersive sections of arbitrary geometry, such as multi-bend transfer lines. The theory treats a 2-dimensional vector space of longitudinal modulations of electron bunches in current and energy. All the collective phenomena, namely LSC, CSR and CER, possibly including the effect of vacuum chamber shielding, are introduced by means of impedances $Z(\lambda)$ [56], as a function of the modulation wavelength λ. The contribution to beam modulations are expressed via matrix multiplication. Although we limit our discussion to LSC, CSR and CER, it is always possible to add piece-wise other longitudinal collective effects, as long as they can be described by impedances. This makes the model highly adaptable to any kind of section and to any degree of accuracy in the description of the beam line.
Given the integrated impedance $Z_{col}(\lambda)$ of a specific collective effect along a section of length L, the corresponding matrix acting on the modulations space is

$$S_L = \frac{1}{E(L)} \begin{pmatrix} E(L) & 0 \\ -Z_{col}(\lambda) I & E(0) \end{pmatrix} \tag{3.10}$$

where $E(z)$ is the energy value along the section, with $0 < z < L$.
When the section is energy-dispersive, the effect of longitudinal Landau Damping can be included through the following matrix

$$\mathcal{D} = \begin{pmatrix} F(\lambda) & ik(\lambda) R_{56} C F(\lambda) \\ iCG(\lambda)/E & CF(\lambda) - k(\lambda) R_{56} C^2 G(\lambda)/E \end{pmatrix} \tag{3.11}$$

where $C = (1 - hR_{56})^{-1}$ and the functions F and G are

$$F(\lambda) = \int \cos[k(\lambda) C R_{56} \delta/E] f(\delta) d\delta \quad \text{and} \quad G(\lambda) = \int \sin[k(\lambda) C R_{56} \delta/E] f(\delta) \delta d\delta \tag{3.12}$$

These quantities embody the suppression of gain due to uncorrelated energy spread and they depend on the slice energy profile. We considered $f(\delta)$ as a normalized Gaussian function with rms energy spread σ_E. More precisely, the dynamics of microbunching inside a dispersive region is regulated by the harmonic content of the slice energy distribution, i.e. by its Fourier transform.

3.1.3 Comparison between models

Since HK and BK are based on the linearization of phase space dynamics, these models agree quite well in the determination of MBI development along a beamline. Both models are able to determine the spurious harmonic content, *i.e.* the bunching factor, the spectral gain of MBI, the energy modulations and the effective energy spread related to MBI. Linear gain is defined as the ratio between final and initial bunching factor,

$$G(k) = \left| \frac{b[k(s), s]}{b_0[k(0), 0]} \right| \tag{3.13}$$

and, as the name suggests, it defines the enhancement of bunching in the linear regime. For this reason, the gain for strongly modulated longitudinal phase space cannot be described by this expression. In particular, while in the HK formalism, the numerator of Eq. (3.13) is given by Eq. (3.7), for the BK formalism, it corresponds to the upper element of the vector obtained after multiplication by the beamline matrix $\mathcal{B}$ [55]

$$b[k(s), s] = (1, 0) \begin{pmatrix} \mathcal{B}_{11} & \mathcal{B}_{12} \\ \mathcal{B}_{21} & \mathcal{B}_{22} \end{pmatrix} \begin{pmatrix} b_0[k(0), 0] \\ 0 \end{pmatrix} \tag{3.14}$$

The dominant contribution to the gain in linac driver for FEL is the zeroth-order LSC-induced energy modulations, converted into density modulations after a dispersive section. This could be no longer verified for long dispersive sections in which beam and MBI dynamics cannot be treated consistently with a first- or second-order approach.
Even in the case of two-stage compressions, it is still possible to demonstrate that the best approximation for linear gain after a single chicane can be written as

$$G(k) \approx \frac{I}{I_A} \left| C k R_{56} \int_0^L ds \frac{4\pi Z_{\mathrm{LSC}}(k, s)}{\gamma(s) Z_0} \right| \mathrm{e}^{-C^2 k^2 R_{56}^2 \sigma_\delta^2 / 2}, \tag{3.15}$$

where we can recognize that

$$p(k,L) = 4\pi \int_0^L b[k(s),s] \frac{I}{I_A} \frac{Z_{\text{LSC}}(k,s)}{\gamma(s) Z_0} ds \tag{3.16}$$

are the relative energy modulations accumulated during acceleration along a section of length L. The expression for the gain is valid whether you are using HK or BK formalism, since CSR and CER have a negligible effect compared to LSC. In the case of HK this is true even at second order in the CSR impedance. This means that, generally speaking, for simple transport line (accelerator + bunch length compressor) the dominant part of the bunching factor is given by the LSC-induced energy microstructures, converted in the dispersive section.
This expression can be generalized in the case of non-Gaussian equilibrium energy distribution $f(p_0)$, knowing that the damping term is proportional to its Fourier transform [57]

$$G(k) \approx \frac{I}{\gamma I_A} \left| C k R_{56} \int_0^L ds \frac{4\pi Z_{\text{LSC}}(k,s)}{Z_0} \right| \int dp_0 f(p_0) \mathrm{e}^{iCkR_{56}p_0}. \tag{3.17}$$

Therefore the LSC-induced RMS absolute energy spread is the integral of the modulation amplitude over the whole spectrum of modulations and we find that [24, 58]

$$\sigma_\gamma^2 = \frac{2ec}{I_0} \int d\lambda \frac{|G(k) Z_{\text{LSC}}(\lambda)|^2}{\lambda^2} \tag{3.18}$$

expressed as an integral over the wavelength $\lambda = 2\pi/k$.
The main difference between these two formalisms relies in the characterization of dispersive section. HK could in principle be derived for any type of beamline, with a significant effort from the analytical and numerical points of view. At the moment, only formulas for chicanes have been derived. On the other hand, BK supplies matrices as building blocks for any combination of dipoles and straight sections and, as long as the linear regime is valid, can already describe any type of beam transport line.

3.1.4 Suppression of MBI

In equation (3.9) the first exponential term is due to the energy spread of the beam, while the second is associated to the dispersion invariant H [59]. These two terms are essential for the control of the instability and, as a matter of fact, they represents two of the most valuable knobs to enhance its damping [26, 60]. Here we show such degrees of freedom are controlled to control MBI gain.

Laser Heater The most adopted solution to damp the gain of instability is the laser heater (LH)[53, 61–64]. Firstly proposed in [53], it is a section designed to introduce a controlled amount of energy spread in the beam and suppress microbunching instability. It is designed to exploit the coupling of an infrared laser pulse and electrons inside of an undulator to introduce energy modulations that are then converted into an effective energy spread. The most common design is composed of a four-dipole chicane with an undulator at the center of it [61–64]. It is usually adopted in the low-energy section of the beam line in order to maximize its effect and it is optimized in order to find a compromise between the suppression of the instability and FEL performance [62]. As an example, the FERMI laser heater is shown in Fig. 3.1.
To quantify the damping, we can derive the matrix in the case of an energy distribution modulated by a laser heater.
Following the standard procedure to characterize the interaction of the laser with the electron bunch, the process can be described as a shaping of the electron energy distribution [61]

$$\rho(s,\Delta\gamma,r) = f_l(s,\Delta\gamma) \times f_t(r) = \frac{I}{ec\sqrt{2\pi}\sigma_\gamma} \exp\left\{ -\frac{[\Delta\gamma - \Delta\gamma_{LH}(r)\sin k_{LH} s]}{2\sigma_\gamma} \right\} \times \frac{1}{2\pi\sigma_x^2} \exp\left\{ \left(-\frac{r^2}{2\sigma_x^2} \right) \right\}, \tag{3.19}$$

where $\Delta\gamma_{LH}(r)$ is the amplitude of the modulation induced by the resonant interaction [61]

$$\Delta\gamma_{LH}(r) = \sqrt{\frac{P_L}{P_0}} \frac{K L_u}{\gamma \sigma_r} \left[J_0\left(\frac{K^2}{4+2K^2} \right) - J_1\left(\frac{K^2}{4+2K^2} \right) \right] \exp\left\{ \left(-\frac{r^2}{4\sigma_r^2} \right) \right\} \tag{3.20}$$

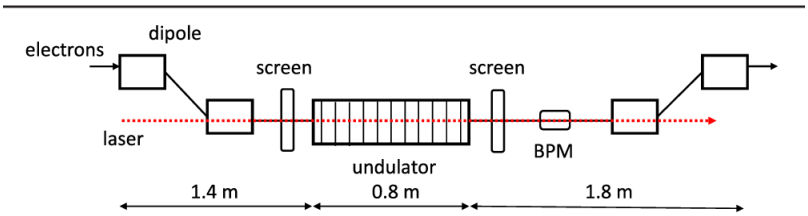

Figure 3.1: Schematic representation of the laser heater chicane at FERMI. The first pair of dipole magnets deflects the beam to a line parallel to the linac axis at a distance of 0.03 m from it, coinciding with the undulator axis. Then the beam is deflected again back to the linac axis by the second pair of magnets. Image from [62].

$\Delta\gamma = \Delta\gamma_{LH}(0)$ and, assuming a round beam, we're using cylindrical coordinates to describe the transverse part of the distribution. To obtain the energy distribution, it is sufficient to integrate ρ over the spatial coordinates

$$f(\Delta\gamma) = \int \rho(s, \Delta\gamma, r) dV = \\ = \frac{1}{\pi\sigma_x^2\sqrt{2\pi}\sigma_\gamma} \int r dr \exp\left\{\left(-\frac{r^2}{2\sigma_x^2}\right)\right\} \int \frac{d\xi}{\sqrt{\Delta\gamma_{LH}(r) - (\Delta\gamma - \xi)^2}} \exp\left\{\left(-\frac{\xi^2}{2\sigma_\gamma^2}\right)\right\} \quad (3.21)$$

In the original BK formalism, a simpler expression for F and G is given[55] and the dependence of ρ from the transverse coordinates is neglected. Here, we derive fully three-dimensional expressions for Landau damping terms, plugging $f(\Delta\gamma)$ in equations (3.11), to obtain

$$F_{LH} = \exp\left\{\left(-\frac{1}{2}k(\lambda)CR_{56}\sigma_\delta\right)\right\} \int RdR \exp\left\{\left(-\frac{R^2}{2}\right)\right\} J_0\left[k(\lambda)R_{56}\delta_{LH} \exp\left\{\left(-\frac{R^2\sigma_x^2}{4\sigma_r^2}\right)\right\}\right] \quad (3.22a)$$

$$G_{LH} = \exp\left\{\left(-\frac{1}{2}k(\lambda)CR_{56}\sigma_\delta\right)\right\} \int RdR \exp\left\{\left(-\frac{R^2}{2}\right)\right\} J_1\left[k(\lambda)R_{56}\delta_{LH} \exp\left\{\left(-\frac{R^2\sigma_x^2}{4\sigma_r^2}\right)\right\}\right]. \quad (3.22b)$$

These expressions allow to model the superposition of laser and electrons in the BK model and take into account the finite sizes of both laser spot and bunch transverse dimensions together with their eventual mismatch. The first expression coincides with the one derived for the HK model [61].

At FERMI, the laser heater is routinely used also with a second purpose: THz-scale modulations at fixed wavelength can be impressed on the electron bunch by a laser pulse with a tailored longitudinal intensity profile [65]. In particular, the laser heater temporal profile is firstly chirped, introducing a phase factor ϕ_a in the electric field proportional to [65]

$$\phi_a = \pi a t^2 \quad (3.23)$$

where a is the linear chirp coefficient. The pulse is then splitted in an interferometer with adjustable delay τ. The recombination of the two pulse results in a chirped-pulse beating [66]. The frequency of this pulse is linear in the delay introduced in one of the two arms of the interferometer between splitted pulses [65]

$$\omega_{\text{beat}} = a\tau. \quad (3.24)$$

At the exit of the LH chicane, the modulated energy spread resulting from the interaction in the undulator is partially converted into density modulation, leading to a seeded microbunching in the whole longitudinal phase space.
Finally, a third configuration has been recently developed. In this configuration, the LH pulse is shortened to reach few ps of duration, shorter enough to heat significantly only a portion of the whole electron bunch. The local heating spoils a reduced portion of the electron longitudinal phase space, leaving the rest unperturbed. In this way, one can correlate the local properties of the bunch with any signal correlated to the longitudinal phase space.

Optics Linear gain theory of MBI is independent from the initial condition, meaning that, independently from the initial condition, the gain function for a beam-line can be determined using either HK or BK formalism. The latter is clearly more versatile for long dispersive sections, multi-bend and energy-dispersive switchyards. For this reason, it can be applied to RF linac-based accelerators, laser- and beam-driven plasma accelerators [25], which typically adopted a switchyard to install energy collimators to protect the undulator or to serve multiple photon beamlines [67–72].

Some differences in the initial condition of the electron beam transported along a switchyard, however,

Table 3.1: Electron Beam Parameters

Parameters	**Values**
Charge	30 pC
Energy	1, 5 GeV
Peak Current	3kA
Bunch Duration (rms)	4 fs
Slice energy spread (rms)	10-300 keV
Normalized emittance(rms)	0.3 μm rad

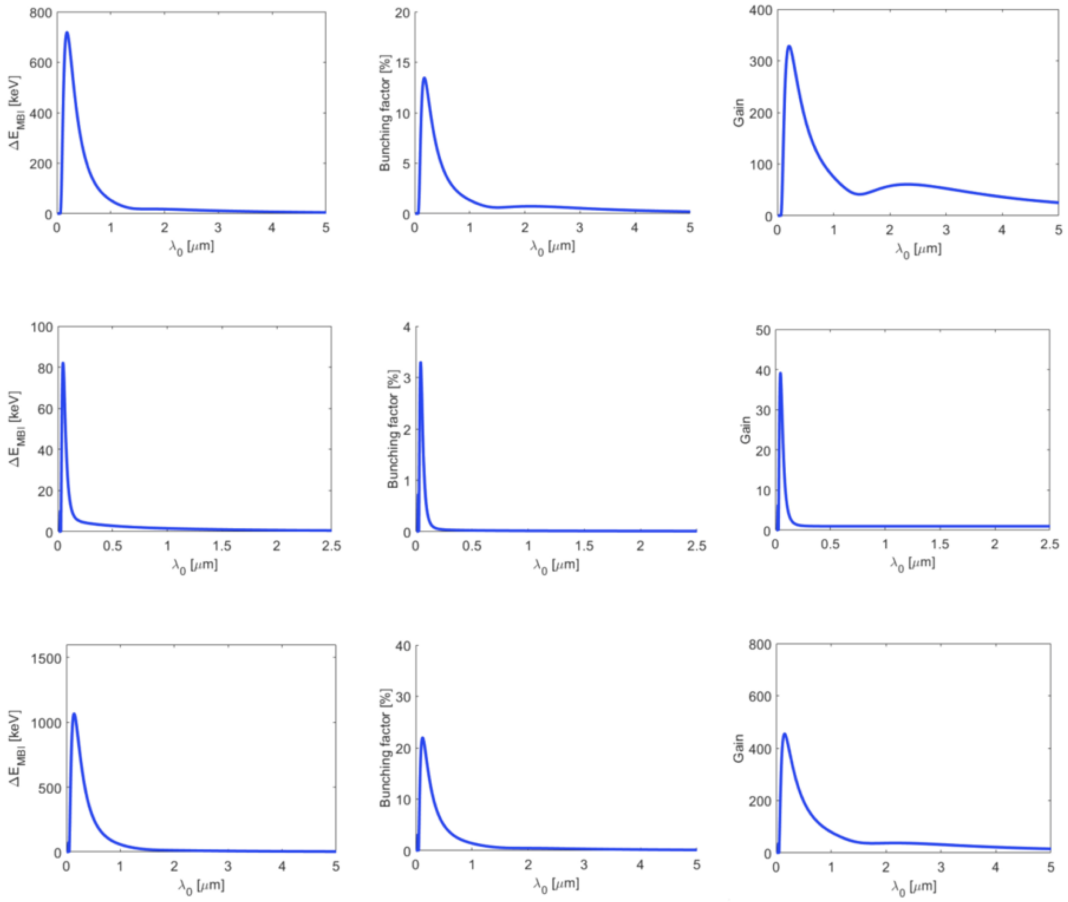

Figure 3.2: From left to right are the final energy modulation, bunching factor, and gain as a function of the initial modulation wavelength λ_0. For the longitudinal transport matrix term $R_{56} = -2.5$ mm (top), $R_{56} = 0$ (middle), and $R_{56} = 2.5$ mm (bottom), respectively. We note the different scales used for the three cases. Image from [25]

need some clarifications. With respect to high-brightness beams driven by radio-frequency (RF) accelerators, the initial condition change significantly and it is important to point them out.
Firstly, because plasma acceleration provides high peak current bunches ($\geq$ 1 A), the electron beam does not undergo the longitudinal beam gymnastics that usually includes bunch length compression and linearization. Secondly, in plasma-based accelerators the effect of the LSC is basically limited to the switchyard path length because the beam energy is already suitable for lasing in soft X-rays (*e.g.*, 1 GeV or more). The total length of the multi-bend transport lines is of order of tens of meters for the aforementioned energies. On the contrary, to reach the undulator in RF linacs, LSC force is the dominant collective effect during the whole acceleration, which is a path tipically from 0.1 to 3 km for final beam energies in the range of 1-17 GeV [73]. Thirdly, the longitudinal phase space generated by plasma accelerators usually shows large relative slice energy spread (SES) values in the range of approximately 0.1-1% [74–77], which tends to dampen the MBI by virtue of Landau energy damping before any amplification builds up, as shown in the next paragraphs.
In summary, the spurious modulations at the entrance of a switchyard after a plasma accelerator are significantly weaker compared to RF linacs.
Despite these facts, however, other factors could heavily affect the development of MBI. *In primis*, the beam charge density in plasma accelerators can still be very high, meaning that collective effects are generally stronger. Moreover, schemes for the reduction of the slice energy spread at the entrance of the undulator are being pursued to achieve more efficient lasing [78–82]. Since the MBI gain is heavily reduced by the relative energy spread and it is linear in the bunch peak current, the growth of the instability also in the switchyard line downstream of a plasma accelerator could become relevant.
Because of the uncertainty of the uncorrelated energy spread at the exit of the plasma cells, which may strongly depend on the details of the scheme adopted for beam generation and acceleration, we will consider this as a variable. Thus, MBI in the switchyard could be analyzed as a function of the momentum compaction or longitudinal transport matrix term (R_{56}) of the line, while for the initial uncorrelated energy spread $\sigma_{E,i}$ in the range of 10-300 keV, beam energies of 1 and 5 GeV are considered. Given these ranges of parameters, our findings allow to infer the dominant physical mechanisms behind the development of the instability and establish some regimes, based on the smaller or larger values of the energy spread. Parameters used for the calculations are shown in Table 3.1.
There are two figures of merit that can be used to evaluate the efficiency of the transport line: the gain peak

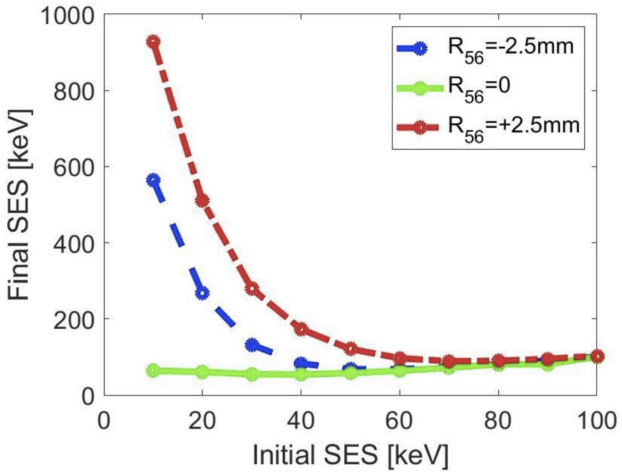

Figure 3.3: The calculated final slice energy spread vs. initial slice energy spread for three switchyard optics (see Table 3.2). Image from [25]

of the instability and the effective final energy spread. Based on these parameters, we can provide analytical prescriptions for the terms of the first-order transport matrix of the switchyard. These in turn are necessary conditions—although are not sufficient—for the preservation of the bend plane emittance in the presence of CSR kicks and longitudinal emittance (Liouvillian behavior). The semi-analytical estimation of the MBI through the switchyard indicates that the isochronous optics is preferable, since it minimizes the instability

with respect to both positive and negative momentum compaction. The reduction in the peak gain and peak energy modulation amplitude is up to 10-fold (see Fig. 3.2). However, the isochronous optics blue-shifts the maximum gain at sub-μm wavelengths, which could still interfere with lasing at < 1 nm.
Considering the comparison of the final SES in Fig. 3.3, we find that the optics associated with a larger gain, *i.e.*, non-zero R_{56}, show a non-linear trend of MBI for $\sigma_{E,i} < 60$ keV, which is a signature of the phase space dominated by the instability. At larger values of $\sigma_{E,i} < 60$ keV, the dependence becomes linear, which reflects the preservation of the longitudinal emittance, *i.e.*, the instability is largely mitigated or suppressed. On the contrary, the isochronous optics shows MBI as being almost independent from $\sigma_{E,i} < 60$ keV for small values of this parameter (*i.e.*, the non-linear dependence is strongly suppressed), while a linear dependence still exists for larger values. At a minimum value of $\sigma_{E,i} \approx 30$ keV, the instability level is already largely mitigated.
A similar result is obtained for $\sigma_{E,i} > 70$ keV for the non-isochronous optics. The final slice energy spread (SES) is partly reduced by a negative R_{56} value with respect to the positive value (see Table 3.2), which indicates a contribution of LSC to the total gain. Regardless, the isochronous optics give a 10-fold smaller SES value.

Table 3.2: Numerical Results for MBI Peak Gain and Final Energy Spread

R_{56} [mm]	Peak Gain	σ_{MBI} [keV]
+2.5	407	928
0	38	64
-2.5	281	565

3.2 Intra-beam scattering

Intrabeam scattering (IBS) is the multiple small-angle Coulomb scattering of charged particles in accelerators. It can drive the growth in time of transverse emittance and uncorrelated energy spread, proportional to the beam charge density. IBS can be pictured as a diffusion process in the phase space, where collisions lead the distribution towards a spherical shape in the beam reference frame and redistribute the momenta of electrons. Since Landau damping is strongly dependent on the beam energy spread, IBS plays a pivotal role in the reduction of MBI and is, therefore, a crucial effect that has to be included in calculations [24, 83].
The novelty in our treatment is the analytic evaluation of the IBS cutoff: in a plasma-like environment such as the accelerated electron bunches, light could be considered as a massive particle, hence characterized by a finite range and a Yukawa potential. This effective mass is a function of the electron beam spatial and temporal structure and is changing as the beam is compressed or accelerated. It has been demonstrated that this mechanism could impact significantly the development of IBS-induced energy spread. [24, 83]
Historically, there are two consistent approaches to characterize the growth rate of transverse and longitudinal emittances. The first one, due to Piwinski [84], is based on Analytical Mechanics; the second one, due to Bjorken and Mtingwa [85], is based on Quantum Field Theory. These formalisms coincide in the high energy approximation [86]. The relevance of this effect to the development of storage rings has recently been recognized with the Wilson Prize to A. Piwinski, J. D. Bjorken and S. K. Mtingwa [87]. Because of the computational expense required to implement the full theory in particle tracking codes, high energy approximations have been derived [88–90].
We start from the Vlasov equation for $f(\vec{X}; s)$, this time including the collision term (Boltzmann equation) in the Fokker-Planck approximation,

$$\frac{\partial f(\vec{X}; s)}{\partial s} + \{f(\vec{X}; s), H\} = \left(\frac{\partial f(\vec{X}; s)}{\partial s}\right)_c, \tag{3.25}$$

where the last term represents the effect of collisions. This expression is obtained as a small-angle expansion of the Boltzmann collisional term and is equal to

$$\left(\frac{\partial f(\vec{X}; s)}{\partial s}\right)_c = -\sum_i \frac{\partial}{\partial p_i}(f(\vec{X}; s)D_i) + \frac{1}{2}\sum_{i,j}\frac{\partial^2}{\partial p_i \partial p_j}(f(\vec{X}; s)D_{ij}) \tag{3.26}$$

The first term is a drift and the second is a diffusion process, whose coefficients, D_i and D_{ij} are written in term of the Rosenblath potentials [91]. IBS growth rate found by [85] can be recovered taking the second order momenta of (3.25) when $f(\vec{X};s)$ is assumed to be equal to the zeroth order Gaussian $f_0(\vec{X};s)$. Therefore, the dynamics described by IBS is the exchange of longitudinal and transverse momenta of particles, resulting in a diffusion process in the phase space. In other words, it is a relaxation in the momentum distribution to a spherical shape in the beam reference frame, acting on both emittance and energy spread.
In the framework of linac-driven FELs and as discussed in previous chapter, we are particularly interested to the growth rate of the relative energy spread, described by the differential equation [86]:

$$\frac{1}{\tau_\delta} = \frac{1}{\sigma_\delta}\frac{d\sigma_\delta}{dt} = \frac{cr_e^2 N_e[\log]\sigma_H}{16\gamma^2(\epsilon_{nx}\sigma_x)^{1/2}(\epsilon_{ny}\sigma_y)^{1/2}\sigma_z\sigma_\delta^3} g\left[\left(\frac{\beta_x\epsilon_{n_y}}{\beta_y\epsilon_{n_x}}\right)^{1/2}\right], \tag{3.27}$$

where c is the speed of light, r_e is the classical electron radius, N_e is the number of electrons, $\sigma_\delta = \sigma_E/E$, $\gamma = E/mc^2$, ϵ_n is the normalized emittance, $\sigma_{x,y}$ are the beam's rms sizes, $\beta_{x,y}$ are the betatron functions, σ_z is the bunch length,

$$\frac{1}{\sigma_H^2} = \frac{1}{\sigma_\delta^2} + \frac{\gamma\mathcal{H}_x}{\epsilon_{n_x}} + \frac{\gamma\mathcal{H}_y}{\epsilon_{n_y}}, \quad \mathcal{H}_{x,y} = \frac{\left[\eta_{x,y}^2 + \left(\beta_{x,y}\eta'_{x,y} - \frac{1}{2}\beta'_{x,y}\eta_{x,y}\right)^2\right]}{\beta_{x,y}} \tag{3.28}$$

in which η is the dispersion lattice function, and finally

$$g(x) = \frac{4\sqrt{x}}{\pi}\int_0^\infty \frac{y^2 dy}{\sqrt{(1+y^2)(x^2+y^2)}}\left(\frac{1}{1+y^2} + \frac{1}{x^2+y^2}\right) \tag{3.29}$$

Both the Piwinski [84] and Bjorken-Mtingwa [85] theory includes the so-called Coulomb logarithm:

$$[\log] = \ln\left(\frac{b_{max}}{b_{min}}\right) \approx \ln\left(\frac{\theta_{max}}{\theta_{min}}\right) \tag{3.30}$$

with b_{max} and b_{min} the maximum and minimum impact parameter of IBS scattering events, θ_{max} and θ_{min} the maximum and minimum scattering angle. Equation (3.30) inherits the logarithmic behavior from the phase space divergence in the presence of long-range interactions; the divergence can be avoided by imposing a cutoff. This procedure is mandatory not only to normalize the integration in the phase space, but also to discard hard scattering events, which may heavily bias IBS contributions in the bunch core [28]. The minimum scattering angle is usually chosen in terms of Debye length or beam size. The lower limit is taken to be

$$\theta_{min} \approx \frac{2r_e m^2 c^2}{b_{max} p^2} = \frac{2r_e}{\sigma_x \bar{\beta}^2} \tag{3.31}$$

choosing $b_{max} = \sigma_x$, (see [24]), and p is the momentum in the C.o.M. system. We propose a new estimate for the maximum scattering angle [24], inspired to the strategy proposed for synchrotrons [92]. The upper limit is given in terms of the momentum transfer in the collision, q, calculated as the boundary beyond which the integrated scattering rate matches a characteristic time τ. In the absence of equilibrium conditions, as they commonly happen to be in a storage ring, τ becomes here the time the beam takes to travel along the accelerator.
We start from [92]

$$q_{max}^2 = \frac{c\tau N_e r_e^2}{2\pi\gamma^2\epsilon_x\epsilon_y\sigma_z\sigma_\delta}\int_0^\infty \frac{dx}{\sqrt{x^4 + ux^3 + vx^2 + wx}} \tag{3.32}$$

where the relation between q and θ is [84]

$$q = \frac{\bar{\beta}}{2}\sin\left(\frac{\theta}{2}\right) \approx \bar{\beta}\theta, \tag{3.33}$$

and $\bar{\beta}$ is the average normalized velocity in the C.o.M. system and the coefficients u, v and w are [92]

$$u = \gamma^2 \left(\frac{\gamma \mathcal{H}_x}{\epsilon_{n_x}} + \frac{1}{\sigma_\delta^2} + \frac{\beta_x}{\gamma \epsilon_{n_x}} + \frac{\beta_y}{\gamma \epsilon_{n_y}} \right) \tag{3.34}$$

$$v = \gamma^2 \left(\frac{\gamma^2 \mathcal{H}_x \beta_y}{\epsilon_{n_x} \epsilon_{n_y}} + \frac{\beta_x \beta_y}{\epsilon_{n_x} \epsilon_{n_y}} + \frac{\gamma \beta_x}{\epsilon_{n_x} \sigma_\delta^2} + \frac{\gamma \beta_y}{\epsilon_{n_y} \sigma_\delta^2} + \frac{\gamma^2 \eta_x^2}{\epsilon_{n_x}} \right) \tag{3.35}$$

$$w = \gamma^2 \left(\frac{\gamma^3 \eta_x^2 \beta_y}{\epsilon_{n_x}^2 \epsilon_{n_y}} + \frac{\gamma^2 \beta_x \beta_y}{\epsilon_{n_x} \epsilon_{n_y} \sigma_\delta^2} \right), \tag{3.36}$$

For a round ($\epsilon_x = \epsilon_y$, $\beta_x = \beta_y$) and ultra-relativistic electron beam in a *straight* section, the polynomial's coefficients reduce to:

$$u = \frac{\gamma^2}{\sigma_\delta^2}, \qquad v = 2\frac{\beta_x}{\epsilon_n}\frac{\gamma^3}{\sigma_\delta^2} = 2\frac{\beta_x \gamma}{\epsilon_n} u = 2\chi u, \qquad w = \frac{\beta_x^2}{\epsilon_n^2}\frac{\gamma^4}{\sigma_\delta^2} = \chi^2 u \tag{3.37}$$

and the integral can be rewritten in the simpler form

$$I = \int_0^\infty \frac{dx}{\sqrt{x}\sqrt{x^3 + u(x+\chi)^2}}. \tag{3.38}$$

We now apply a change of variable of the form $x = \chi/(z-1)$, we get

$$I = \frac{1}{\chi}\frac{1}{\sqrt{\delta}} \int_1^\infty \frac{dz}{\sqrt{z^3 - z^2 + 1/\delta}}, \tag{3.39}$$

where $\delta = u/\chi = \gamma \epsilon_n / \beta_x \sigma_\delta^2$. We note that in high brightness electron beams, and even for multi-GeV beam energies, δ is a small quantity, of the order of 10^5-10^6. This allows us to take into account only terms of the order of $\mathcal{O}(1/\sqrt{\delta})$. We therefore rewrite eq. (3.32) as:

$$q_{max}^2 \approxeq \frac{c\tau N_e r_e^2}{2\gamma^{3/2} \epsilon_n^{3/2} \sigma_z \sqrt{\beta_x}}. \tag{3.40}$$

The mean value of the electron velocity in the C.o.M. frame is $\bar{\beta} = \frac{\gamma \sigma_{x'}}{\sqrt{2}}$ [24]. This is substituted in the expression for the angles in (3.30), getting

$$\log\left(\frac{\theta_{max}}{\theta_{min}}\right) = \log\left(\frac{q_{max}\sigma_x \bar{\beta}}{2r_e}\right) = \log\left(\frac{q_{max}\epsilon_n}{2\sqrt{2}r_e}\right). \tag{3.41}$$

Differently from our first estimation [24], we can conclude that, at first order in δ, the Coulomb logarithm does not depend on σ_δ, but it does depend upon γ. The implication of our new findings compared to our first estimates are illustrated and discussed below.
For an ultra-relativistic beam in a *dispersive* section, instead [92],

$$u = \frac{\gamma^2}{\sigma_H^2}, \qquad v = \frac{\gamma^2 \beta_y}{\sigma_H^2 \epsilon_{n_y}} + \frac{\gamma^2 \tilde{\sigma}_x^2}{\sigma^2 \epsilon_{n_x}^2} = \alpha u + \zeta, \qquad w = \frac{\gamma^2 \beta_y \tilde{\sigma}_x^2}{\sigma^2 \epsilon_{n_x}^2 \epsilon_{n_y}} = \alpha\zeta \tag{3.42}$$

Again, the integral can be rewritten in the simpler form

$$I = \int_0^\infty \frac{dx}{\sqrt{x}\sqrt{x^3 + (ux+\beta)(x+\alpha)}}. \tag{3.43}$$

Since $\alpha u/\zeta \approx 1$ and defining the coefficient $\omega = \zeta/\alpha^2$, we obtain

$$\frac{1}{\alpha}\int_0^\infty \frac{dy}{\sqrt{1+\omega y(y+1)^2}} = \frac{1}{\alpha\sqrt{\omega}} \int_1^\infty \frac{dz}{\sqrt{1/\omega + z^3 - z^2}} \propto \frac{1}{\alpha\sqrt{\omega}} = \frac{1}{\sqrt{\alpha u}} \tag{3.44}$$

Notice that α plays the role of χ in the non-dispersive case, but now u depends on σ_H. As a consequence, the Coulomb logarithm has the same formal expression of the non-dispersive case, but now q_{max} is the expression (3.32) times the ratio σ_H/σ_δ.
Again, it is important to underline that these integrals at first order in δ are analytically exact, differently from the numerical one used so far [24]. On top of the higher precision reached in the determination of the Coulomb logarithm, which was still ambiguous in dispersive regions, its functional dependence on the beam energy and from the energy spread is now explicit, leading to new expressions for the induced energy spread.

3.2.1 IBS-induced energy spread

With the proposed expression for the Coulomb logarithm in equation (3.41), we can proceed and solve equation (3.27). We discriminate two cases: dispersive section at constant energy and straight (or non-dispersive) section, in the presence or absence of acceleration. In the latter configuration, the beam energy is assumed to grow linearly along the section with a null dispersion ($\mathcal{H}_{x,y} = 0$) and a gradient $G = [E(L) - E(0)]/L$, i.e.

$$d\gamma = \frac{G}{mc^2} cdt = \frac{G}{mc^2} ds \tag{3.45}$$

Straight section with varying energy

For the moment, we simplify the math by assuming a round beam. Thus, the function in (3.29) becomes $g(1) = 2$ and the growth rate differential equation is simplified:

$$\frac{1}{\tau_\delta} = \frac{cr_e^2 N_e [\log](\gamma)}{8\gamma^2 \epsilon_n \sigma_x(\gamma)\sigma_z \sigma_\delta^2} \tag{3.46}$$

where we make explicit the dependence on γ of the terms. In addition to IBS growth rate, we take into account the growth rate term associated to acceleration $1/\tau_{acc}$. This quantity can be derived imposing that the absolute energy spread does not change during acceleration:

$$\frac{d\sigma_\gamma}{ds} = \frac{d}{ds}(\gamma\sigma_\delta) = \sigma_\delta \frac{d\gamma}{ds} + \gamma \frac{d\sigma_\delta}{ds} = 0. \tag{3.47}$$

The right-hand side of the equation (3.47), using (3.45), implies that

$$\frac{1}{\sigma_\delta}\frac{d\sigma_\delta}{ds} = \frac{G}{mc^2\tau_{acc}} = -\frac{G}{mc^2\gamma} \tag{3.48}$$

or, equivalently,

$$\frac{1}{\sigma_\delta}\frac{d\sigma_\delta}{d\gamma} = \frac{1}{\tau_{acc}} = -\frac{1}{\gamma} \tag{3.49}$$

Combination of equations (3.27) and (3.49) can be recast in the following form

$$\frac{d\sigma_\delta^2}{d\gamma} = \frac{2\sigma_\delta^2}{\tau_{acc}} + \frac{r_e N_e mc^2 [\log](\gamma)}{4G\gamma^2 \epsilon_n \sigma_x(\gamma)\sigma_z} = -\frac{2\sigma_\delta^2}{\gamma} + k\frac{[\log](\gamma)}{\gamma^{3/2}} \quad \text{with} \quad k = \frac{r_e N_e mc^2}{4G\epsilon_n^{3/2}\beta_x^{1/2}\sigma_z}. \tag{3.50}$$

The solution is

$$\sigma_\delta^2(\gamma) = \sigma_\delta^2(\gamma_0)\frac{\gamma_0^2}{\gamma} + \frac{1}{\gamma^2}\int_{\gamma^0}^{\gamma} g(\gamma')\gamma'^2 d\gamma' \quad \text{and} \quad g(x) = \frac{k[\log](x)}{x^{3/2}}. \tag{3.51}$$

Straight section with constant energy

In this case the separation of variables is immediate, leading to

$$\sigma_\delta^2(s) - \sigma_\delta^2(0) = \frac{r_e N_e [\log] s}{4\gamma^{3/2}\epsilon_n^{3/2}\beta_x^{1/2}\sigma_z}. \tag{3.52}$$

This expression can also be derived by looking at certain limits of the previous solutions. In fact, this results coincides with the first case, if $d\gamma$ tend to zero, since the ratio $d\gamma/G$ reduces to L/mc^2.

Dispersive section

The differential equation to be solved has the form:

$$\frac{d\sigma_\delta^2}{ds} = \frac{a\log\left(b\frac{\sigma_H}{\sigma_\delta}\right)}{\sqrt{h\sigma_\delta^2 + 1}} \quad \text{with} \quad a = \frac{r_e^2 N_e}{4\gamma^2\epsilon_n\sigma_x\sigma_z}, \quad b = \sqrt{c\tau a}\frac{\epsilon_n}{2r_e}, \quad h = \frac{\gamma\mathcal{H}_x}{\epsilon_n}. \tag{3.53}$$

The equation can be integrated separating the variables,

$$\int \frac{\sqrt{h\sigma_\delta^2+1}d\sigma_\delta^2}{\log\left(\frac{b}{\sqrt{h\sigma_\delta^2+1}}\right)} = \frac{2b^3}{h}\left\{Ei\left[3\log\left(\frac{\sqrt{h\sigma_\delta(0)+1}}{b}\right)\right] - Ei\left[3\log\left(\frac{\sqrt{h\sigma_\delta(s)+1}}{b}\right)\right]\right\} = as \quad (3.54)$$

in which Ei stands for the exponential integral [93].
In order to find the value of $\sigma_\delta(s)^2$, we need to find numerically the zero of the function F, written as

$$F(x) = \frac{2b^3}{h}\left\{Ei\left[3\log\left(\frac{\sqrt{hx_0+1}}{b}\right)\right] - Ei\left[3\log\left(\frac{\sqrt{hx+1}}{b}\right)\right]\right\} - as \quad (3.55)$$

If we take the limit for h that tends to zero, equation (3.55) coincide with (3.52).

3.2.2 Interplay between MBI and IBS

IBS and MBI both affect and are affected by the bunch phase space distribution and can be coupled using Vlasov-Maxwell equations. The main interplay between them is given by the inclusion of IBS-induced uncorrelated energy spread in the MBI model, which substantially modifies the instability gain through energy Landau damping [24]. In doing so, we still consider only the effect of IBS on the zeroth order term of the energy distribution $f(\vec{X};s)$ in (3.25), assumed to be a diffusive process in the longitudinal momentum space. According to a recent numerical analysis [94], we can in fact discard higher order effects on microbunching instability (MBI).
More quantitatively, we can derive the conditions under which energy spread growth due to intrabeam scattering can or cannot be neglected when considering the evolution of microbunching instability in a magnetic bunch length compressor. Considering that in the BK model the energy distribution and the bunching factor are updated step-wisely, by discretizing the curvilinear coordinate along the simulated beamline, this model is not able to fully couple the dynamics of MBI, as instead permitted by massive numerical calculations by Vlasov solvers. To give a quantitative answer, we look at the microbunching gain as defined in HK model. The only situation in which the IBS has an impact on the microbunching gain is for the initial bunching and energy modulations, whose Landau damping term is equal to

$$\exp\left\{\left(-\frac{\bar{\sigma}_\delta^2(s_f)}{2(1+hR_{56})^2}\right)\right\} \quad \text{with} \quad \bar{\sigma}_\delta^2(s_f) = k_0R_{56}(\sigma_\delta^2(0)+\sigma_{\delta,IBS}^2). \quad (3.56)$$

Although limited to only two of the numerous terms coming from the staged amplification used to determine the MBI growth, it affects the dominant contribution, as explained before.
The contribution from the first dipole, considering that the dominant part of the damping is due to the term proportional to $R_{51}(s_1)$ in equation (3.9), is

$$\begin{aligned}\int_0^{L_b} ds_1 K(s_1,s_3)b[k(s_1);s_1] =& \frac{\sqrt{\pi}A\bar{I}_f}{2\bar{\sigma}_x}\exp\left\{\left(-\frac{\bar{\sigma}_\delta^2(0)}{2(1+hR_{56})^2}+D^2\right)\right\}\times \\ &\times\left[erf\left(\bar{\sigma}_x+D\right)-erf\left(D\right)\right]b_0[k_0;0] \end{aligned} \quad (3.57)$$

where we have assumed for simplicity that

$$\sigma_\delta(s) \approx \sigma_\delta(0) + a\log(b)s = \sigma_\delta(0) + As \quad (3.58)$$

and we have introduced the new quantity D

$$D = \frac{L_bk_0^2R_{56}^2B(s_f)^2A}{2\bar{\sigma}_x}. \quad (3.59)$$

D quantifies the contribution of growing energy spread. The possibility to ignore the IBS effect translate to $D \ll 1$, or

$$\lambda_0 \gg \lambda_{crit} = \frac{\pi L_bR_{56}^2B(s_f)^2A}{2\sqrt{\epsilon_0\beta_0}\nu} \quad (3.60)$$

where ν is the chicane bending angle.
We now recall the $H(t)$ function and rewrite it with the inclusion of terms describing the IBS effect. The evaluation of the modified $H(t)$ allows us to quantify the relevance of those terms to the overall dynamics.

$$H(t) = \exp\left\{\left[-\bar{\sigma}_x^2 \frac{(1-2t+\alpha_0\phi t)^2+\phi^2 t^2}{(1+hR_{56}t)^2} - \frac{\bar{\sigma}_\delta(t)}{2(1+hR_{56}t)^2}\left(t^2+\frac{(1-t)^2}{(1+hR_{56})^2}\right)\right]\right\} \tag{3.61}$$

in which $\phi = 2\Delta L/\beta_0$.
IBS contributes with terms at first, second and third order in t in the numerator. We keep only the first two, accordingly to the assumptions of the model. The expression for the added contributions is

$$\exp\left[\frac{L_b k_0^2 R_{56}^2 B(f)^2 A}{2(1+hR_{56}t)^2} t(1-2t)\right] = \exp\left\{\left[\frac{\bar{\sigma}_x D}{\pi(1+hR_{56}t)^2} t(1-2t)\right]\right\} \tag{3.62}$$

and we therefore find that IBS is negligible when:

$$|L_b R_{56}^2 B(f)^2 A| \ll |4\epsilon\beta\theta_{chicane}^2(\alpha_0\phi-2)| \quad \text{and} \quad |L_b C^2 R_{56}^2 A| \ll |\epsilon\beta\theta_{chicane}^2[4(\alpha_0\phi-2)^2+\phi^2]|, \tag{3.63}$$

for the linear and quadratic term respectively. However, the first condition is sufficient since it implies also the second one. So, rewritten in terms of λ_{crit}, the first condition becomes

$$\bar{\sigma}_x \lambda_0 \gg \frac{\lambda_{crit}}{2|\alpha_0\phi-2|}. \tag{3.64}$$

Again, condition (3.60) is stronger than condition (3.64), demonstrating that the IBS can be neglected for these terms. For instance, at the FERMI first magnetic bunch compressor (BC1), the value of λ_{crit} is in a range between 10^{-8} and 10^{-9} m. Therefore, since the FEL process is affected by modulations at the micron scale, we are legitimized to neglect all the contributions.

3.3 Experimental characterization of MBI

There are several direct and indirect indications of the presence of microbunching instability along the linac and downstream. In what follows we recollected some of the direct techniques used to characterize the development of MBI and benchmark our models.

3.3.1 Energy spread measurement

"As we have demonstrated, the IBS-induced energy spread modifies the exponential term of the MBI gain, which physically represents energy Landau damping. In doing so, the gain at successive compression stages is diminished, with an overall mitigation of the instability. In this section is shown that in configurations of relatively high gain, neglecting the IBS contribution to σ_δ can lead to unrealistic predictions of the gain, of the energy modulation and, in particular, of the final SES (slice energy spread). In this systematic comparison of the SES after the bunch compressor predicted by the model and the experimental data is the observable

$$\sigma_\delta = \sqrt{C\sigma_0^2 + \sigma_{\text{IBS}}^2 + \sigma_\gamma^2} \tag{3.65}$$

where C is the compression factor, σ_0 is the initial energy spread, σ_{IBS} is the IBS induced energy spread and σ_γ is the MBI-related effective energy spread. The former has been introduced in this chapter, while the other have been defined in the previous chapter and sections.

Diagnostic tools

Table 3.3 lists the main parameters of the experiment carried out at the FERMI facility and used in the model. The beam longitudinal phase space was measured at the diagnostic beam dump (DBD) station [95]. The DBD layout is shown in Appendix A.
Beam optics were matched in the DBD region in order to optimize the temporal and the energy resolution at the screen. The systematic error to the deviation of the measured SES from the effective value is due to the screen pixel size, to the beam non-zero vertical emittance ε_y, and to the VRFD-induced energy spread.

Table 3.3: Electron Beam and Machine Parameters

Bunch parameters	100 pC	650 pC	units
Initial peak current	18	60	A
Initial beam energy	96	96	A
Beam energy at BC1	∼290	∼290	MeV
Beam energy at BC2	424-740	610	MeV
Final beam energy	713-754	900	MeV
R_{56} in BC1	-35,-42	-42	mm
R_{56} in BC2	0,-35	0	mm
Compression factor	31-45	11-19	
Normalized emittance	0.4	1.3	μm mrad
$\langle\beta_{x,y}\rangle$ along the linac	7-30	7-30	m
Temporal resolution	8-12	8-12	fs
Energy spread resolution	65-85	65-85	keV

The latter is due to the off-axis longitudinal electric field component sampled by deflected particles. Such spread of longitudinal momentum is correlated with the particle's vertical position inside the cavity, and thus with the bunch length. Its rms value relative to the beam mean energy $E \approx \bar{p}_z$, where $\bar{p}_z$ is the beam central longitudinal momentum and c the speed of light in vacuum, evaluated at σ_z-distance from the bunch centroid, is [96]

$$\sigma_{\delta,\mathsf{VD}} \approx \frac{eV_{RF}k_{RF}}{2\bar{p}_z c}\sqrt{\left(\frac{eV_{RF}k_{RF}L\sigma_z}{3\bar{p}_z c}\right)^2 + \varepsilon_y\beta_{y,\mathsf{VD}}} \tag{3.66}$$

Measurements of the beam optics parameters, of the SES vs the deflector RF power attenuation factor, and the evaluation of the effective peak deflecting voltage, led to the estimated temporal and energy resolutions in Table 3.3. $\sigma_{\delta,\mathsf{VD}}$ is the dominant contribution to the energy resolution, where the VRFD length is $L = 3.5$ m, the operational effective peak voltage and RF wave vector are $V_{RF} \approx 19$ MV and $k_{RF} = 62.8\text{m}^{-1}$, and the average vertical betatron function along the deflector is $\beta_{y,\mathsf{VD}} \approx 25$ m.
The experimental values of SES reported in the following are averaged over 20 consecutive images collected at 10 Hz. At the high charge of 650 pC, a quadratic time-energy correlation appears in the phase space (so-called nonlinear energy chirp), due to longitudinal wakefields in the accelerator. In this case, the SES is defined as the minimum value of the energy spread measured along the bunch (i.e., in correspondence of null time-energy correlation). The associated current profile is usually flat. At the low charge of 100 pC, the energy chirp is dominated by a linear component. In this case, the SES is defined as the energy spread of the central slice, and the linear energy chirp is removed in the post-processing. For each slice, the local current level is also recorded. For most of the recorded images, the SES is calculated as the standard deviation of a Gaussian, which is used to fit the energy distribution of each temporal slice. In some cases, a better fit is ensured by a flat top distribution, and the SES is therefore defined as raw RMS value. For all the images, the temporal duration of the slice is approximately 10 fs.

Initial energy spread

The major uncertainty in our model is the initial value of the uncorrelated energy spread, $\sigma_{E,0}$, i.e., the uncorrelated energy spread at the exit of the linac photo-injector. Since its variation at keV level substantially modifies the model prediction, and since there is no direct measurement of $\sigma_{E,0}$ because of limited resolution, it has been treated in our model as a fitting parameter. That is, while keeping all other machine and beam parameters fixed and in adherence to the experimental settings, we scanned the value of $\sigma_{E,0}$, for the 100 pC and 650 pC bunch charge, in order to obtain a systematic agreement of the measured and the predicted SES over all compression schemes and compression factors. This procedure reproduces the final SES measured in Fig. 3.6b for the fitting value $\sigma_0 = 0.9$ keV at 100 pC, and $\sigma_0 = 2.4$ keV at 650 pC. It is a remarkable result the fact that a single value of σ_0 (per injector set up) satisfies all the diverse linac configurations.

To demonstrate that our fit for $\sigma_{E,0}$ is the only realistic solution, we conducted two independent checks. First, we calculated the SES without IBS, by selecting the value of σ_0 that, in this unrealistic picture, allows

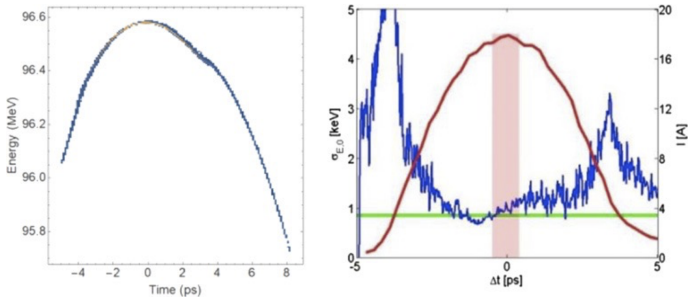

Figure 3.4: Left: longitudinal phase space of the 100 pC charge beam at the exit of the FERMI injector, simulated with GPT. Right: peak current (red) and SES (blue) from GPT tracking. The green horizontal line represents the semi-analytical model prediction of $\sigma_0 = 0.9$ keV. Image from [24]

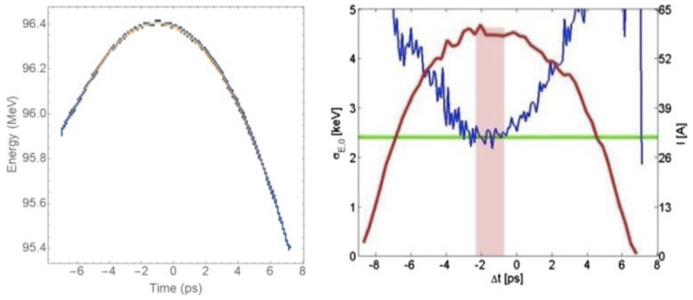

Figure 3.5: Left: longitudinal phase space of the 650 pC charge beam at the exit of the FERMI injector, simulated with GPT. Right: peak current (red) and SES (blue) from GPT tracking. The green horizontal line represents the semi-analytical model prediction of $\sigma_0 = 2.4$ keV. Image from [24]

the predicted SES to collapse onto the measured one. A single value of σ_0 cannot be found in order to satisfy all the diverse compression schemes at 100 pC. Also, the values are far from those obtained when IBS is included in the model: in the absence of IBS, they result in the range 5.5–6.8 keV for 100 pC (vs 0.9 keV when IBS is included), and around 4.3 keV for 650 pC (vs 2.4 keV when IBS is included). Second, we compared our expectations for σ_0 with the SES predicted by particle tracking at the exit of the FERMI injector. This is shown in Figs. 3.4 and 3.5. Tracking was performed with the 3D GPT code [97], which solves the particles' equation of motion starting from the Liénard–Wiechert retarded potentials. This approach promises an accurate prediction of the initial uncorrelated energy spread, in accordance, for example, with findings in [98]. However, IBS intended as a stochastic process was not included in the simulations. Still, the application of our model to the injector section estimates a net IBS-induced energy spread of 0.3 keV for both bunch charges. This has to be added in quadrature to the 0.9 keV and 2.4 keV assumed so far. Thus, the correction of IBS in the injector to the effective total energy spread is expected to be negligible.
The simulated longitudinal phase space at the injector exit is also shown in Figs. 3.4 and 3.5. Since our model assumes the same transverse Gaussian distribution and a constant local beam current in each slice, we have highlighted the region of the peak current which, in the tracking, corresponds to the modelled current level. The superposition of blue data (tracking result) and green line (model) within the red bar region (modeled slice current) shows that the GPT prediction for $\sigma_{E,0}$ is in agreement with our fit in the presence of IBS. In contrast, the aforementioned values of σ_0 used in the model without IBS do not match the tracking results. Oscillations and much larger values of the simulated SES at lower current regions are due to higher numerical sampling noise for small number of particles, and residual large energy chirp components in the phase space.
In summary, our fit for the initial uncorrelated energy spread, as derived from the MBI model with the revisited single pass theory of IBS, is consistent with particle tracking simulations of the injector. An analogous fit from a model without IBS, is not.

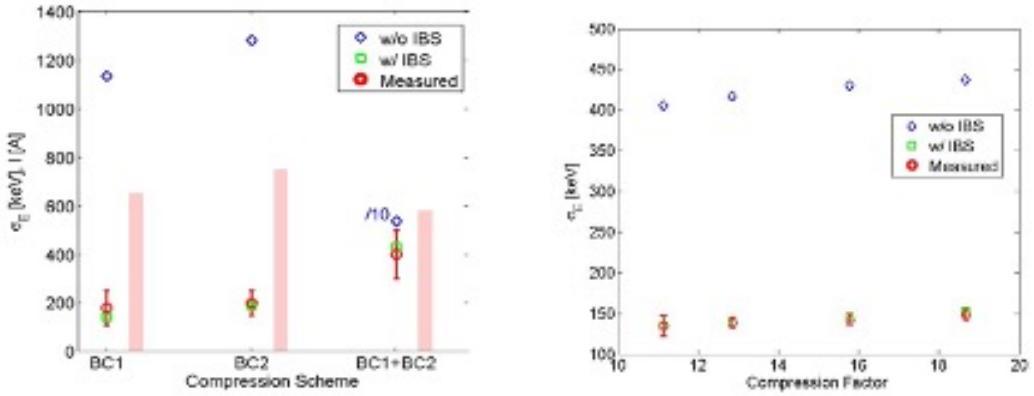

(a) (b)

Figure 3.6: Left: SES (dots) and peak current (bars) measured at the linac end for the 100 pC beam, for various compression schemes. The SES is compared with the prediction of the MBI model with (green squares) and without IBS (blue diamonds). One of the blue points is diminished by a factor 10 for better visibility. Right: SES measured at the linac end for the 650 pC beam. The SES is compared with the prediction of the MBI model with (green squares) and without IBS (blue diamonds). The compression is accomplished with BC1 only, and the compression factor varied through linac RF phases. The peak current ranges from ∼600 to ∼1100 A. Image from [24]

Final energy spread

Figure 3.6 compares the measured and the predicted SES at the end of the FERMI linac, for different compression schemes at low charge (top), and for single compression but at various compression factors at high charge (bottom). The laser heater is switched off in all the measurements. The error bars of the measured data are dominated by the reproducibility of consecutive measurements in the same experimental session. The error bars on the model predictions are dominated by the uncertainty on the average beam sizes in the linac (see next subsection).

Figure 3.6 shows that the proposed model is able to capture the physics of the instability, predicting SES

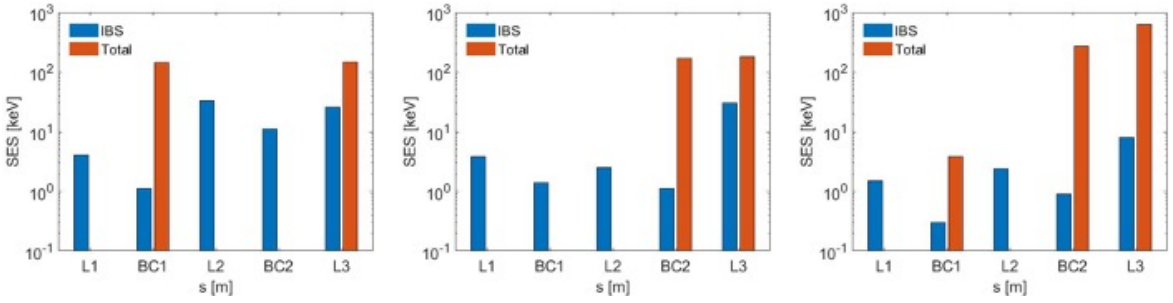

(a) (b) (c)

Figure 3.7: Calculation of the net IBS contribution to the SES (blue bars) accumulated through individual linac sections (see Appendix A for the labeling) and total SES as contributed by IBS and MBI energy modulations in the presence of magnetic compression.From top to bottom: BC1-only, BC2-only and BC1+BC2 compression scheme. The bunch charge is 100 pC in each case. Laser Heater is off. Image from [24]

values at the same level as the experimental data. More importantly, it clearly points out the discrepancy between the predicted and the measured SES in the case that IBS is not included in the model. Figure 5 also shows that the contribution of IBS to the MBI development is larger for higher instability gain, such as in the BC1 + BC2 scheme, as compared to the single compression cases. In fact, when IBS is not included in the model, the double compression offers an unrealistically large value of the SES (see Fig. 3.6a, in which the blue marker is lowered by a factor 10 for better visibility). That is because at large gain, any

additional although small contribution to σ_δ enhances the exponential damping in Eq. (3.18) more notably. Conversely, when the gain is intrinsically low, the effect of additional Landau damping by IBS is less pronounced: the amplification process and therefore the final SES depends more weakly on variations of the machine configuration such as the compression factor (this is the case of Fig. 3.6b).
For completeness, we show in Fig. 3.7 the prediction of the net contribution from IBS to the SES accumulated along individual linac sections (blue bars), for the three compression schemes studied with the low charge beam. The total SES (orange bars) is also given, which represents the SES contributed by MBI (Eq. (3.18)) and IBS (Eq. (3.51), (3.52) and (3.54)), taking into account the compression factor at each chicane. The height of the final orange bar is the SES reported in Fig. 3.6a (IBS included).
To summarize, for plausible injector longitudinal phase space, it is only with the inclusion of the integrated effect of IBS along the whole linac that we can reproduce the SES observed at the end of acceleration, for a wide range of beam parameters and machine configurations, for a single value of σ_0 per injector setup, and in agreement with the σ_0 predicted by particle tracking runs.

Sensitivity to laser heater and beam sizes

The validity of the proposed model is now discussed in the presence of two additional effects, laser heater and large electron beam sizes. This draws on additional experimental results.
Firstly, the model predictions are compared with measured values of the SES in a condition of laser heater turned on, and at a level such that the MBI is suppressed. In this case, one expects an approximate preservation of the longitudinal beam emittance (Liouvillian behaviour), and therefore the SES should be inversely proportional to bunch duration. Figure 3.8 illustrates this situation for the 100 pC bunch charge, compressed in BC1 over a wide range of compression factors. We observe that, first, the model agrees with the expected linear dependence of the SES on the compression factor. Secondly, although the impact of IBS on the beam dynamics is not as significant as in the presence of strong MBI gain, its contribution to the final energy spread leads to the agreement of experimental and modeled results. By comparing Fig. 3.8 with Fig. 3.6, we conclude that IBS lowers the final SES by virtue of energy Landau damping when the instability gain is high. Conversely, it increases the final SES when the instability gain is intrinsically small.
It was mentioned earlier that the major uncertainty in the model is the beam initial energy spread. This

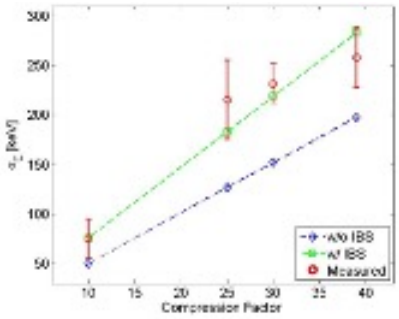

Figure 3.8: SES vs. compression factor, for 100 pC bunch charge and compression in BC1 only. The laser heater is inducing 6 keV RMS energy spread before compression. Image from [24]

uncertainty has been addressed in the previous section. A second uncertainty may derive from the local variation of the beam sizes (namely, Twiss parameters) along tens-of-meters-long linac sections. As discussed in the previous sections, the model assumes average beam sizes, calculated as a function of the transverse emittances and Twiss functions measured at the injector exit, of experimental quadrupole magnets setting and accelerating gradients. Optics matching is reinforced at additional locations, *i.e.*, in the BC1 region and at the linac end. While in most cases the deviation of the beam optics from a matched condition is very limited, the possibility exists of local large oscillations of the betatron functions, due to either mishandling of the magnets or inaccurate matching.
To investigate the sensitivity of our model to the beam sizes, we show in figure 8 the predicted SES for the 100 pC bunch charge (with same parameters as in Fig. 3.6a, see also Table 3.3) as a function of the average betatron function in the low energy part of the FERMI linac. This region is constituted by the laser heater insertion followed by linac1, for acceleration up to BC1. The beam energy ranges from 96 to approximately 300 MeV, for a total length of 43 m (over a total linac length of 150 m). Single and double compression

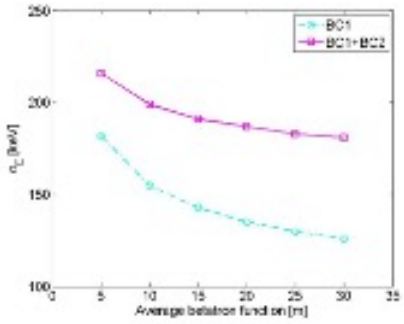

Figure 3.9: SES calculated with the MBI+IBS model vs average betatron function in the low energy region of the FERMI linac, for the 100 pC bunch charge in single (BC1) and double compression (BC1+BC2). Image from [24]

schemes are modeled in Fig. 3.9, with no laser heater action. It is seen that the modification to the predicted SES for a variation of the betatron functions by an unrealistic factor 6 (equivalent to more than doubled beam sizes, and up to 500μm RMS) is at the level of few tens of keV. This variation in the beam optics is considered to have a larger effect on the calculated SES than any remaining inaccuracy in the modeling of the three-dimensional dynamics related to the longitudinal space charge impedance, or in the estimated impact parameters for the Coulomb logarithm.
In summary, no realistic uncertainty on the actual beam optics could significantly impact the prediction of the model as depicted in Figures 3.6 and 3.8, nor the discrepancy of predicted and measured values when IBS is not included." From one of my paper [24]

3.3.2 2-D Fourier analysis

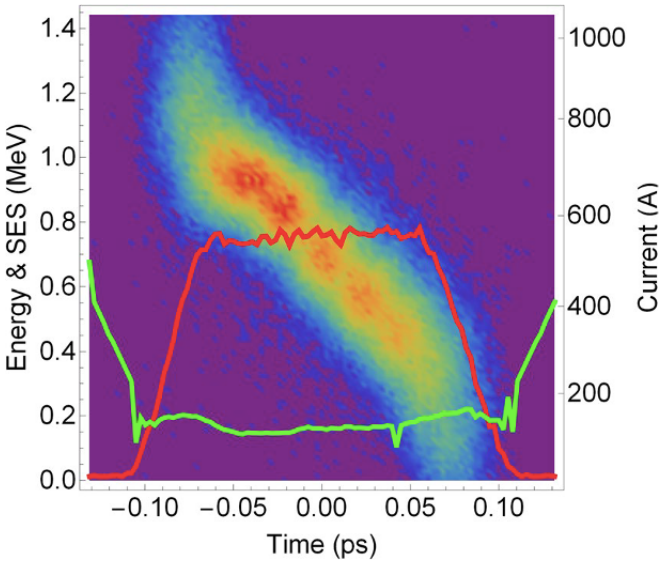

Figure 3.10: Longitudinal phase space of a typical bunch compressed using BC1 only, with the laser heater switched off. The current profile of the bunch is shown in red, and the slice energy spread is in green. Image from [22].

As we have seen, micro-bunching instability information are encoded in the one dimensional Fourier-transformed current profile $b[k(s), s]$. The inclusion of energy modulations in the description leads to a formalism that require a bi-dimensional vector space that can be associated with the 2-D Fourier transform of the whole longitudinal phase space.

Following HK notation, this modulation factor can be expressed as [22]

$$b[k(s), m(s), s] = \frac{1}{N} \int d\vec{X} \mathrm{e}^{-i(kz+m\delta)} f(\vec{X}; s), \tag{3.67}$$

where $m(s)$ is the wavenumber associated to the energy modulation. At first order in the perturbation, the kernel for the MBI evolution remains the same and the dynamics is solely determined by the converted energy modulation at the frequency $m = kCR_{56}$ and by the initial condition.
There are, however, additional information that can be retrieved using a 2-D formalism. The addition of a new axis implies the possibility to consider rotation in the Fourier phase space instead of simple dilation of the frequency. Rotation of the longitudinal phase space in a bunch compressor, for instance, depends on the initial phase of the plasma oscillation and the angle of rotation of phase space in the bunch compressor [60]. In this optics, we are therefore able to map plasma oscillations of the bunch together with the MBI gain spectrum.
An example of measured beam longitudinal phase space in DBD (see Appendix A) is shown in Fig. 3.10. Microbunching parameters can be extracted from the 2-D Fourier transform of this image, only after a filtering process: low- and high-frequency peaks in intensity are excluded to limit the region of interest. In this way, modulations of the order of the bunch length (corresponding to low-order chirps) and artificial structures coming from the limited screen resolution and noise in the measurements are filtered out. The axes are then converted from frequency to wavelength and from dimensions of inverse energy space to dimensions of energy.
The plasma oscillation phase of a microbunched beam, named θ_p, can be measured using the 2-D Fourier transform of the bunch image. θ_p, in fact, is given by the angle of the satellites in 2-D frequency space with respect to the central term (see Fig. 3.11). Microbunching in longitudinal coordinate is given for $\theta_p = 0, \pi$,

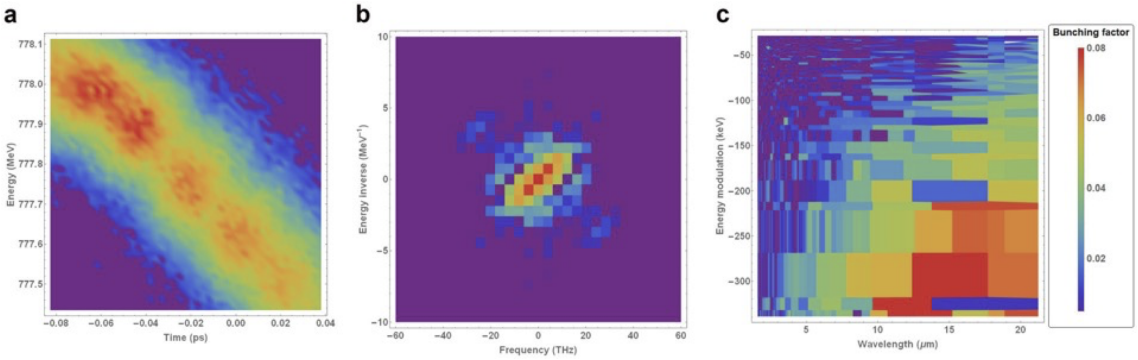

Figure 3.11: Example of 2D microbunching analysis for a bunch compressed using BC1 only, with the laser heater off. The two satellites located around in the middle plot represent the modulations in intensity that are visible in (**a**). (**a**) Longitudinal phase space. (**b**) Fourier spectrum of (**a**) in frequency space. (**c**) Zoomed-in Fourier spectrum of (**a**) in wavelength space (mean of 20 shots). Image from [22].

Table 3.4: Electron Beam and Machine Parameters

Bunch parameters	**Values**
Bunch charge	100 pC
Beam energy	787 MeV
Bunch length (rms)	54 fs
Chicane bending angle	105 mrad
R_{56}	-62.5 mm
Peak current	560 A
Relative energy spread (rms)	0.1%
Linear energy chirp at BC entrance	$\approx$-15.5 m^{-1}
Linear energy chirp at DBD	$\approx$-20 m^{-1}

while microbunching in energy corresponds to $\theta_p = \pi/2, 3\pi/2$. Any intermediate value between these pure

modulations along one axis indicates that there is some mixing between bunching in energy and in density (see again Fig. 3.11 as an example). In such cases, simply projecting the bunching along one axis will present a distorted picture of the microbunching period, which in principle would require two parameters, namely a radius and an angle in the frequencies space. The distance from the central term gives the periodicity along both axes. The arctangent of the ratio of these quantities, normalized with respect to the bunch length and energy spread of the beam, is defined as the normalized plasma oscillation phase.
Figure 3.11 shows an example of 2D microbunching analysis for a bunch compressed using BC1 only. Machine and beam parameters are specified in Table 3.4.
As mentioned above, manipulation of the longitudinal phase space, such as bunch compression or transport along dispersive sections, can cause shearing and rotation of the satellites. Therefore, any controlled variation of the beam parameters relevant for MBI (energy spread, charge, current, compression etc..) can be used as a knob to map the evolution in this 2-D space [22]. As a matter of fact, this technique can be used also for energy modulation superimposed by manipulating the electron bunch with the LH beating technique [23].
Figure 3.12 shows a comparison between two measurement of longitudinal phase space with initial beating frequencies of 1.2 and 2.4 THz in a double compression scheme. Machine and beam parameters are specified in Table 3.5. Notice that the number of microbunches present in the bunch increases with the beating

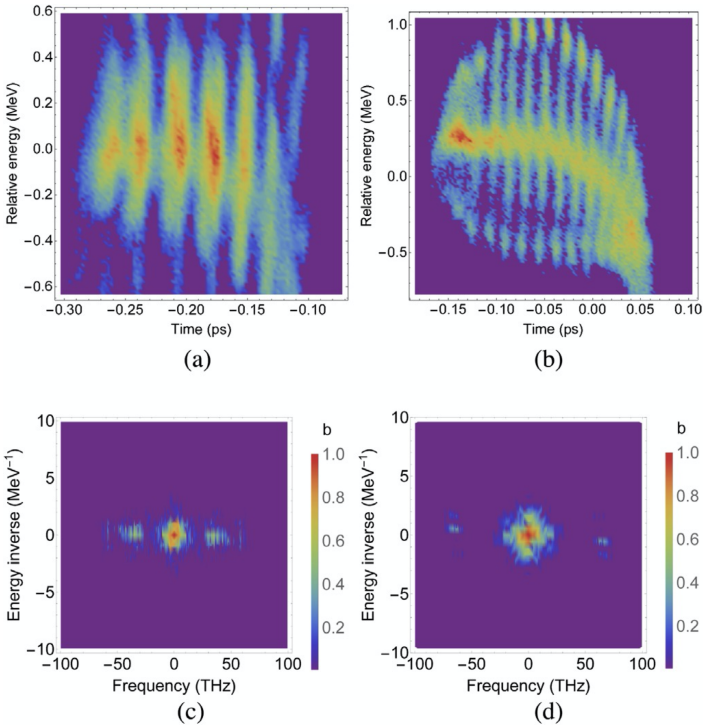

Figure 3.12: Single-shot measured longitudinal phase space and Fourier transform averaged over 20 shots. BC1 and BC2 bending angles are set to 105 and 28.5 mrad, respectively, with initial beating frequencies of 1.2 (a,c) and 2.4 (b,d) THz and an initial laser pulse energy of 3.5 μJ. Image from [23]

frequency. In this case, the beam is compressed twice for a total compression factor of 23. The predicted final bunching frequency are $1.2 \times 23 \approx 30$ and $2.4 \times 23 \approx 55$ THz, respectively.
The separation of the satellites from the dc term varies as a function of the initial modulation, and agreement between the predicted and measured final bunching frequency can clearly be seen. This prediction is consistent with the 1-D model because, in the case of the double compression scheme, the bunch exhibited a modulation almost entirely in density (considering that $\theta_p \approx 0$). Different is the case for the single compression scheme shown in Fig. 3.11, in which θ_p has a non-zero value.

Table 3.5: Electron Beam and Machine Parameters

Bunch parameters	**Values**
Bunch charge	100 pC
Beam energy	780 MeV
Bunch length (rms)	54 fs
Chicane bending angle	105, 28.5 mrad
R_{56}	-62.5, -22.5 mm
Peak current	650 A
Relative energy spread (rms)	0.05%
Linear energy chirp at DBD	$\approx$-1 $\%\text{m}^{-1}$

3.3.3 Infrared spectrometer

Experimental setup

The new diagnostics for MBI is installed in the FERMI Undulator Hall, on the FEL2 chain (see Appendix A). A diagnostics screen equipped via a 1 μm aluminum tensioned is installed at the center of a magnetic chicane just downstream to the FEL2 first stage. The screen is the source of transition radiation. Because of the presence of MBI, the radiation is coherent and is the dominant part of the transition radiation. Our instrument spectral range was chosen on the basis on theoretical works on beam dynamics to be in the range from 1 to 10 μm and to cover this range a CaF_2 prism spectrometer has been used. We installed the two detectors (PbSe based and a pyrodetector) on two different branches selectable by a remotely controlled flipper. Each detector is equipped with vertical slit set at about 200 micron to reach a resolution of the order of 100 nm. They are installed on a motorized translation stage and acquisition of the detector signal while scanning the translation stage produces a spectrum of coherent transition radiation (CTR) averaged on multiple bunches. More detail about the setup will be published in the near future.
Generally speaking, the spectrum of the CTR is a function of the whole electron phase space, including the eventual structures along the transverse section of the bunch. However, the homogeneity and constancy of the transverse properties of the beam, allows us to consider the CTR as a function of the longitudinal phase space only and factor out the dependence on the other spatial coordinates. For this reason, we conduct our studies considering only the dependence on the signal from the longitudinal properties of the bunch (duration and energy spread). Radiation coming from the whole electron bunch covers a range wider than that which is expected for MBI, and in principle could propagate co-axially with the interested signal. In particular, THz emission could have a strong impact on the detected signal. However, because of the geometry of the setup and the choice of the prism and detectors, the detection involves only the MBI-related signal.

Shot noise-driven MBI

Along the FERMI linac there are two main dispersive regions, the first bunch length compressor and the spreader line between the linac end and the Undulator Hall. Every development or enhancement of MBI has to be traced back to one of the two. In Fig. 3.13a, we characterize the variation in intensity and wavelength of the natural MBI as a function of the compression. The map is for a 1.3 GeV beam, avoiding the use of the laser heater. The variation in the compression factor is described by a parameter called PYRO: a PYRO equal to 1×10^6 translates into a compression factor $C = 6$ and is approximately linear, meaning that 2×10^6 corresponds to $C = 12$. This figure already reveals several features about the MBI at FERMI. Firstly, the fact that the main peak's wavelength is independent from compression is a strong suggestion that the dominant contribution that we register has its origin in the dispersive section after the bunch compressor. The intensity scales linearly with C as shown in Fig. 3.13b, confirming that the mechanism that relies behind the amplification is related to the current density.
Also the laser heater intensity or, equivalently, the energy spread of the beam was scanned. As expected from the theory, in Fig. 3.14a an increase in the energy spread enhances the Landau Damping and therefore reduces the growth of the instability. The optimal setting of heating for the MBI suppression is also compared with the one that optimizes the FEL performance using the same electron beam. Fig. 3.14b compares the integrated signal from the infrared spectrometer and the spurious harmonic content in the

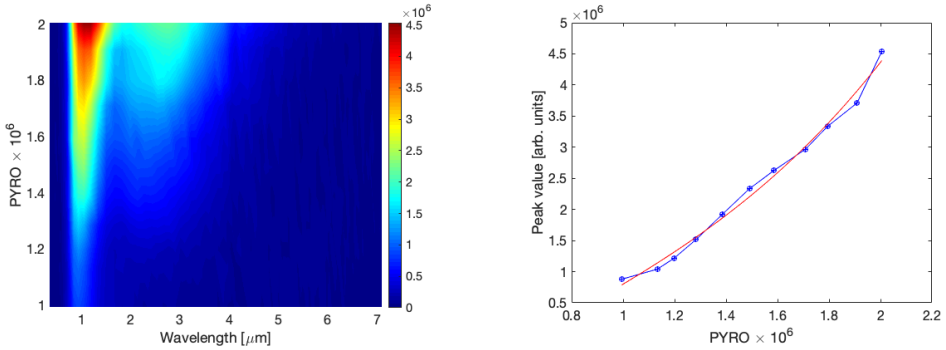

(a) (b)

Figure 3.13: On the left: map of the MBI content of the beam at 1.3 GeV, without the use of laser heater. The variation of the signal is characterized as a function of the compression factor.
On the right: variation of the maximum signal as a function of the compression factor.

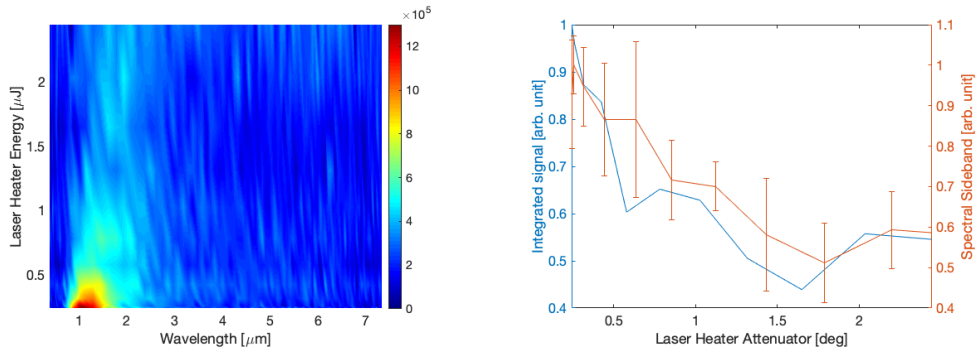

(a) (b)

Figure 3.14: On the left: map of the MBI content of the beam at 0.9 GeV with a highly compressed beam ($C > 15$). The variation of the signal is characterized as a function of the LH-induced energy spread. The enhancement of Landau damping exponentially reduces the signal.
On the right: Comparison between the reduction of the sideband of FEL and reduction of the integrated signal in Fig. 3.14a

FEL spectra, following the technique explained in [26]. FEL-2 was tuned at 13.3 nm, obtained as harmonic 6×3 of a 239.4 nm seed laser. The qualitative similarity between the two trends confirms that, as the laser heater reduces the MBI, the sideband signal decreases and so does the MBI signal on the spectrometer. Aside from the standard characterization, corroborated by theory, that can be performed to explore the MBI mechanism, we want to understand also if it develops uniformly along the bunch or if it is a slice property, affecting differently some portion of the beam. To do so we exploit the third operational mode of the laser heater at FERMI, *i.e.* the short pulse configuration, to investigate the local nature of the instability. As a matter of fact, it is possible to map the MBI strength along the bunch, correlating the elimination of MBI with the eventual reduction of the spectrometer signal. A more detailed presentation of this configuration will be given in a future paper.
Figures 3.15a and 3.15b display the impact of normal and short laser heater: the left figure, at a fixed delay, demonstrates that MBI signal can be reduced exponentially; the right figure, instead, is a scan of the temporal delay between electrons and the shortened laser pulse. Despite the fact that the LH is scanned along the whole bunch, no variation is registered. Reducing only locally the harmonic content of the beam is not enough to determine a significant reduction of the global signal, meaning that MBI is uniformly distributed along the whole bunch.

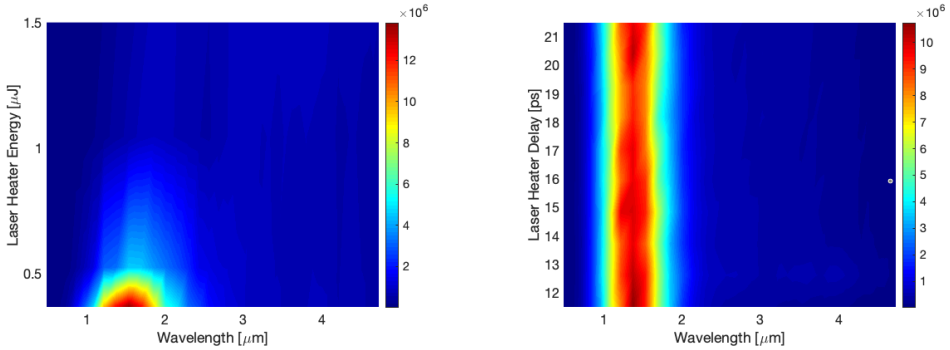

(a) (b)

Figure 3.15: Impact of the LH-induced energy spread in the nominal configuration and a delay scan of the shortened LH. The map on the left is performed at a fixed delay for the standard LH, showing the exponential decay of the signal. Passing through this delay with the short pulse, there is no evident impact of the local heating on the MBI.

Laser Heater seeded MBI

The spectrometer signal was exploited to characterize the MBI content as a function of the main parameters that affects its dynamics, namely bunch compression and energy spread. To confirm the reliability of the instrument and the correlation with the density modulations in the beam, we use the laser heater beating technique [65]. This method allows to artificially introduce a narrow modulation at a desired wavelength, tuning the delay between two chirped laser pulses inside the undulator section of a laser heater.

The two nearly identical pulses are shown in Fig. 3.16 with the corresponding beating region. These

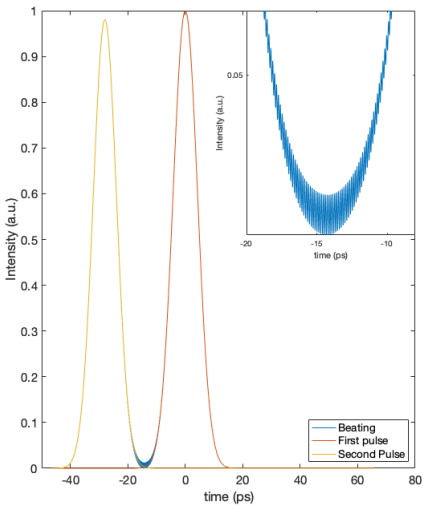

Figure 3.16: Laser Heater double pulses and beating for a delay of 28 ps. Profiles are fitted from measured laser profiles. Parameters are reported in Table 3.6.

profiles are simulated, based on the parameters shown in Table 3.6. In our experiment, the delay was set to 28 ps corresponding to an energy modulation at 38.4 μm. After the magnetic compressor, these modulations are translated into density modulations and blue-shifted by a factor $1/C$. As shown in Fig. 3.17a, it is possible to monitor this dynamics as a function of C for the fundamental wavelength up to the third harmonic on the spectrometer. From the map we extract the variation of the peak wavelength for the fundamental and the second harmonic, confirming the linear dependence on the compression factor, as demonstrated in Fig. 3.17b.

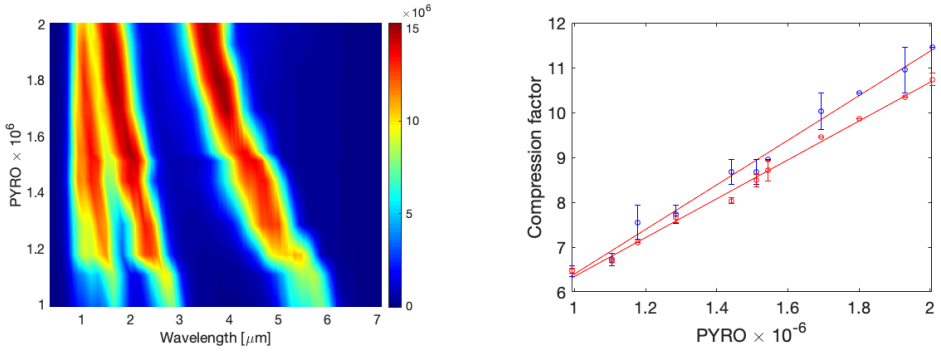

(a) (b)

Figure 3.17: On the left: map of the LH-induced MBI at 38.4 μm (before compression) for a beam at 1.3 GeV as function of the compression factor. The map shows 4 distinctive features, corresponding to the fundamental (extreme right), second and third harmonic and MBI residual contribution at 1.3 μm.
On the right: retrieval of the compression factor as a function of PYRO signal from the fundamental (blue line) and the second harmonic (red line).

Table 3.6: Laser Heater Beating parameters

Parameters	**First Laser Pulse**	**Second Laser Pulse**
Duration	9.9 ps	9.5 ps
Chirp	-2.59×10^{23} m/s^2	-2.79×10^{23}
Bandwidth (FWHM)	5.09 nm	5.26 nm

3.4 Interplay between MBI and FEL

In the next section, the impact of MBI on the performance of seeded FELs is demonstrated theoretically and experimentally, showing what we called indirect measurements of MBI. Together with the HGHG scheme, also the EEHG [99] (Echo-enabled Harmonic Generation) is considered.
Firstly we demonstrate how, a MBI-free electron beam could significantly improve the spectral purity and energy per pulse of an HGHG source, extending its wavelength range down to even higher harmonics. Then we show how the EEHG scheme is affected by spurious density and energy modulations and how its brightness can be enhanced by the use of a laser heater or by optimizing the transport along the transfer line between the linac and the FEL.

3.4.1 HGHG

FERMI experienced the possibility to lase with a MBI-free electron beam. For this reason, we termed it *cold beam*, referring to the low energy spread and energy modulation content [27]. "Measurements of the time-slice energy spread of the electron bunch are routinely performed by using the rf deflector in combination with the energy spectrometer [95]. As explained before, the measurement resolution depends on several parameters (beam optics, rf deflecting voltage, beam energy). In the specific case of FERMI, considering a beam energy in the range 1.0 - 1.5 GeV, the minimum energy spread value that can be resolved is about 100 keV [62]. Since the cold beam produced at FERMI has a slice energy spread well below this value and an alternative method is necessary to measure this parameter. As FERMI FEL2, FERMI FEL1 too can be operated in SASE as a high-gain optical klystron [42]. According to [40, 41] the maximum FEL intensity is obtained when:

$$\frac{R_{56} k_r \sigma_E}{E} = 1, \tag{3.68}$$

where R_{56} is the momentum compaction of the dispersive section, $k_r = 2\pi/\lambda_r$ and λ_r is FEL output wavelength. The SASE optical klystron is therefore a diagnostic tool to measure the beam energy spread that can be calculated from the value of the dispersion corresponding to the maximum FEL intensity.
The modulator and the radiator of FEL-1 were tuned to be resonant at 31.9 nm and the dispersive section

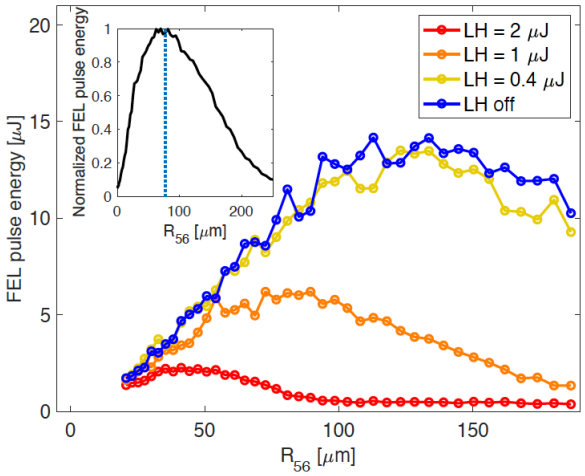

Figure 3.18: FEL pulse energy at 31.9 nm versus the dispersive section R_{56}, for different values of the laser heater energy. Inset reports, for comparison, the FEL normalized pulse energy at 32.1 nm versus R_{56} from previous experiments [42]. Image from [27]

strength between them has been scanned. Figure 3.18 shows the FEL pulse energy measured as a function of the dispersive section R_{56} for different values of the laser heater intensity, and for a beam energy $E = 1.32$ GeV. In order to have a high SASE intensity we initially compressed the electron beam more than in the nominal case reaching a peak current $I_p \approx 1.1$ kA.
The first indication of a reduced microbunching instability gain and of a low energy spread, is given by the fact that the best FEL performance, in terms of pulse energy, is obtained in the absence of the laser heater. This differs from what was observed in the past for a similar FEL configuration (see [42]). On that occasion, the FEL pulse energy was maximized for a low (but not zero) intensity of the laser heater,with an R_{56} value of 75 μm (see vertical dotted line on the inset of Fig. 3.18). In contrast, in the present situation the maximum FEL pulse energy decreases and shifts toward smaller values of R_{56} when the laser heater power is increased. This is a clear indication of a progressive and monotonic growth of the slice energy spread, without the typical minimum for nonzero heating. Similar measurements have been repeated for the nominal FERMI compressed beam, $I_p \approx 0.8$ kA and for higher compression $I_p \approx 1.3$ kA.
Applying Eq. 3.68, σ_E was retrieved in the mentioned cases and the results are summarized in Fig. 3.19. For the nominal case ($I_p \approx 0.8$ kA), a minimum σ_E of about 40 keV was measured, a value much lower

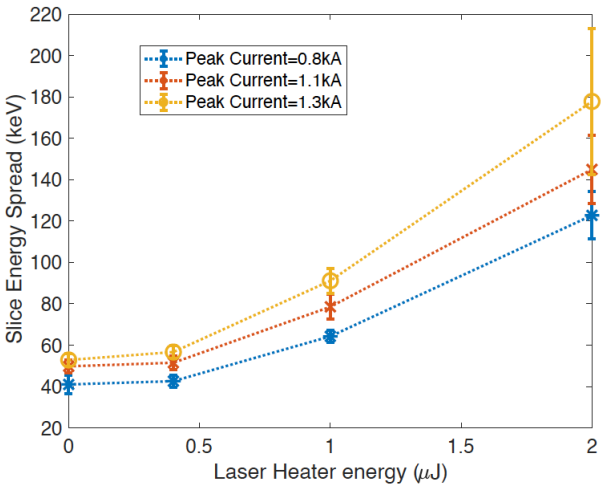

Figure 3.19: Measured time-slice energy spread obtained from Eq. (3.68). The error-bars refer to a confidence interval of 68% in evaluating the optimum value of R_{56}. Image from [27]

than what was usually obtained. Also in the strong compression case ($I_p \approx 1.3$ kA), σ_E is minimized with the laser heater off. This suggests that no microbunching structures have been amplified along the machine, at least to a level that affects the energy spread. In terms of energy spread mitigation, the laser heater is actually not required with this electron beam condition.
As has been reported in the literature [100], the σ_E parameter is of paramount importance. For a seeded FEL as FERMI based on the HGHG scheme, in order to be able to lase efficiently at a harmonic h of the seed laser frequency, the following condition has to be met

$$\frac{\sigma_E}{E} < \delta_{FEL} = \frac{1}{2}\frac{\rho}{\sqrt{1+h^2}} \tag{3.69}$$

where ρ is the FEL parameter, i.e., Pierce parameter [3].
Figure 3.20 shows the maximum tolerable relative energy spread δ_{FEL} calculated for FERMI FEL-1, from 40 nm to 10 nm, according to the inequality (3.69) that provides exponential gain. In the past, the FERMI FEL-1 gain suffered a strong reduction for harmonics (h) larger than $13-15$, indicating a slice energy spread of the order of 100-150 keV, in agreement with the past energy spread measurements [10, 42, 62]. A beam slice energy spread of 40 keV fulfills the condition (3.69) up to harmonic 26 ($\lambda_r = 10$ nm), $\sigma_E/E < 3 \times 10^{-5}$, for a beam energy of 1.32 GeV.
At FERMI, the LH has been exploited to control periodic structures in the electron beam, in order to gen-

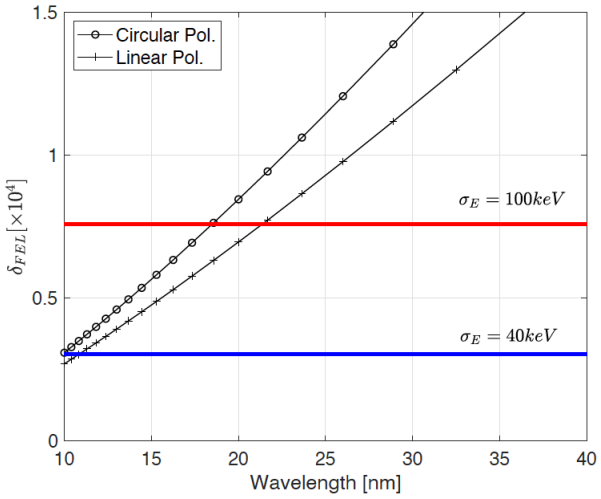

Figure 3.20: The maximum δ_{FEL} versus the FEL output wavelength calculated for FERMI FEL1 undulators tuned in circular and linear polarization, according to Eq. (3.69). The standard FERMI case ($\sigma_E = 100$ keV) and the actual condition ($\sigma_E = 40$ keV) are indicated with horizontal lines, assuming a beam energy of 1.32 GeV. Image from [27]

erate stable spectral sidebands, i.e., multicolor FEL pulses, or to shift the lasing frequency with respect to an integer harmonic of the seed [65], but its main application is the suppression of the microbunching instability [62]. The LH is usually considered essential in the optimization of the FEL aiming at maximizing the FEL intensity while preserving a single mode, Gaussian-shaped, stable from pulse to pulse, radiation spectrum. The impact of the LH on the FEL performance depends upon several parameters including the use of bunch compressor and the original content of microbunching structures and their amplification [61]. At FERMI, the absolute advantage provided by the LH, in terms of FEL intensity and spectral purity, has not been constant over the years, but a small amount of LH energy has been always necessary to optimize the FEL output. A typical case is represented in Fig. 3.21, where the FEL intensity (first row of Fig. 3.21a) and the FEL spectrum (second row of Fig. 3.21a) at 22.5 nm ($h = 11$) are reported as a function of the LH pulse energy controlled through an optical attenuator. When the LH energy is close to zero, the FEL presents a multi-spike spectrum and low pulse energy. It is necessary to increase the LH energy to about 1 μJ to get rid of the microbunching instability and maximize the FEL intensity with a "clean" spectrum. We observed a consistent reduction of the LH energy required to reach such a condition. Figures 3.21b show the same measurements in the new configuration: the FEL spectrum is a single line without evidence

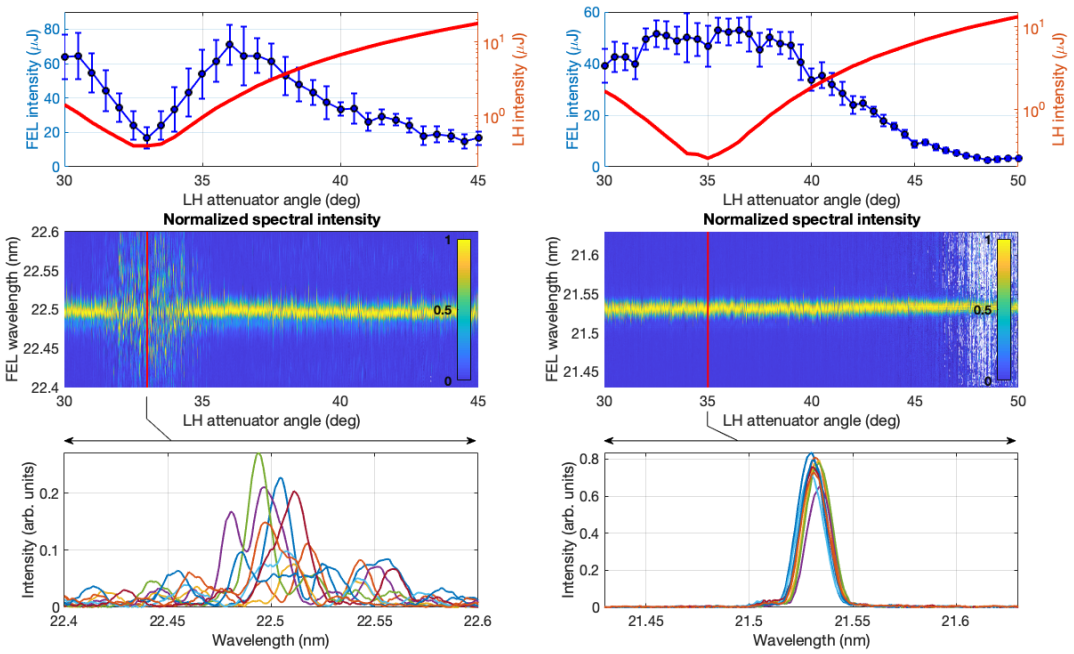

(a) (b)

Figure 3.21: FEL performance versus laser heater for a standard electron beam in 2018 (left column) and for the current one (right column). FEL intensity (blue curve) and laser heater intensity (red curve) (first row) are plotted as a function of the LH attenuator angle. FEL spectra versus LH attenuator angle are reported in the second row in false color scale (normalized for the maximum intensity value). A few spectra for the standard case and for the actual case (last row) have been randomly selected for the minimum value of the LH (≈0.2 μJ). Image from [27]

of microbunching-induced sidebands, and the maximum FEL intensity is obtained at the minimum LH intensity. Apparently, the LH has the effect of increasing the electron slice energy spread and consequently, reducing the FEL gain and the output intensity. This is consistent with the measurements reported in Fig. 3.19, where the minimum slice energy spread was observed for the LH at zero intensity.

Moreover, even in the case of the LH completely off, as shown in Fig. 3.20, the FEL at 21 nm is characterized by a shot-to-shot power stability of 10% (rms), with a bandwidth of 7×10^{-4} (FWHM) averaged over 1800 shots. A small fraction of shots (around 10%) have been filtered out as they were associated with a large jitter of the relative arrival time between seed and electron bunch, as measured by the bunch arrival monitor [101]. The measured spectral bandwidth corresponds to a Fourier limited pulse duration $\delta_t^{(FEL)}$ of about 45 fs (FWHM). This is in agreement with the expected pulse duration (51 fs) calculated from a seed pulse of about 100 fs (FWHM) at 260 nm, according to the rule $\delta_t^{(FEL)} = 7/6 \times \delta_t^{(seed)}/h^{1/3}$, where $h = 12$ is the harmonic order [102]. The residual difference may be due to a small chirp of the seed laser pulse that causes an increase of the time bandwidth product of the FEL pulse. Note also that the scaling relation with the seed pulse duration represents a rough estimate, since the effective pulse duration depends on the level of saturation reached by the amplifier. In fact, far away from the saturation the $\delta_t^{(FEL)}$ scales as $\delta_t^{(seed)}/h^{1/2}$. In presence of time-dependent energy modulation along the bunch, the FEL wavelength output is slightly shifted shot-to-shot according to the temporal jitter between seed and electrons that is about 50 fs [103]. However, in Fig. 3.22 the shot-to-shot wavelength stability (rms 7×10^{-6}) is anyway two orders of magnitude smaller than the FEL bandwidth, and this is another important signature that the beam has no microbunching structures.

The use of a cold electron beam (with $\sigma_E \approx 40$ keV) without microbunching structures at the undulator entrance provides further advantages. As shown in Fig. 3.19, the low slice energy spread enables the

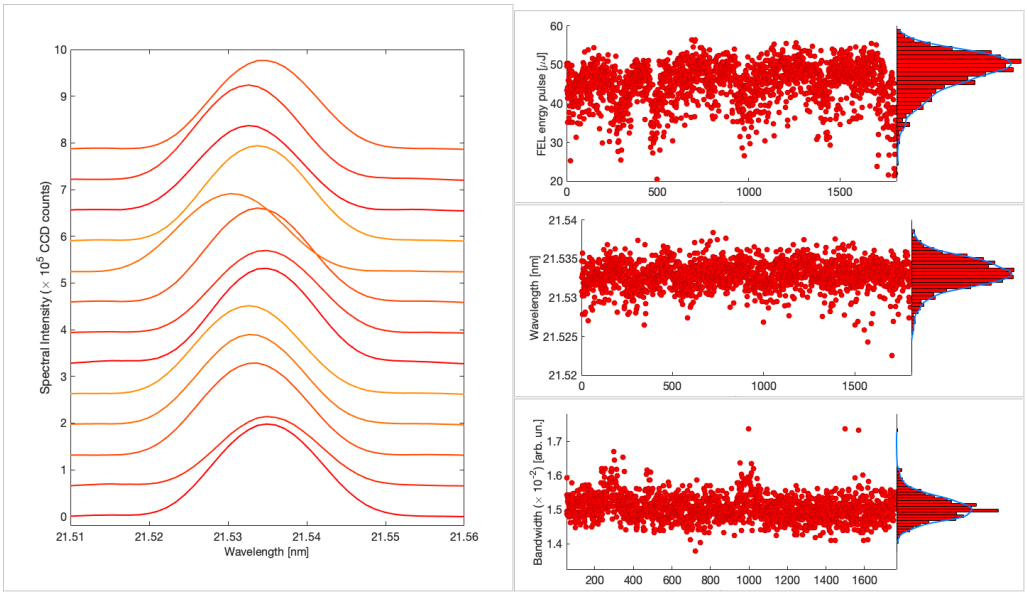

Figure 3.22: Characterization of FEL pulses at $h = 12$ ($\sim$ 21 nm) in linear horizontal polarization. Random selection of individual spectra and statistical analysis over 1800 shots showing energy per pulse, central wavelength and rms spectral bandwidth evolution. Few shots ($\sim$10%) have been removed from the analysis due to very different e-beam parameters. Image from [27]

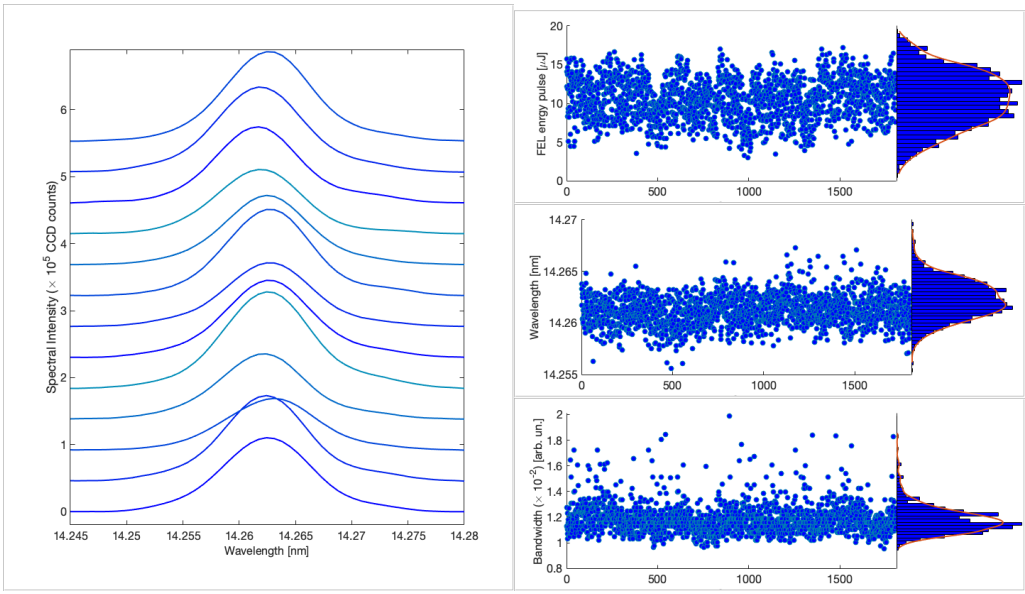

Figure 3.23: Characterization of FEL pulses at $h = 18$ ($\sim$ 14 nm) in linear horizontal polarization. Random selection of individual spectra and statistical analysis over 1800 shots showing energy per pulse, central wavelength and rms spectral bandwidth evolution. Few shots ($\sim$10%) have been removed from the analysis due to very different e-beam parameters. Image from [27]

amplification of shorter wavelengths, such as 14 nm ($h = 18$). FEL operation in this wavelength range was reported in [104], but with a substantially lower pulse energy, and implementing an harmonic cascade scheme. In the present conditions, more than 10 μJ per pulse were measured, with a relative (FWHM) FEL bandwidth of about 6.4×10^{-4}, as reported in Fig. 3.23. The measured FEL bandwidth corresponds to a Fourier limited pulse of about 32 fs (FWHM), in agreement with the aforementioned scaling law that foresees an FEL pulse duration ranging from 24 fs to 45 fs depending upon the level of saturation. Note that the data reported in Fig. 3.23 refer to linearly polarized light. More than a factor two of power increase

is expected in the case of a circularly polarized undulator.

We measured the FEL pulse energy at various wavelengths, in particular from 35 nm ($h = 7$) down to 10

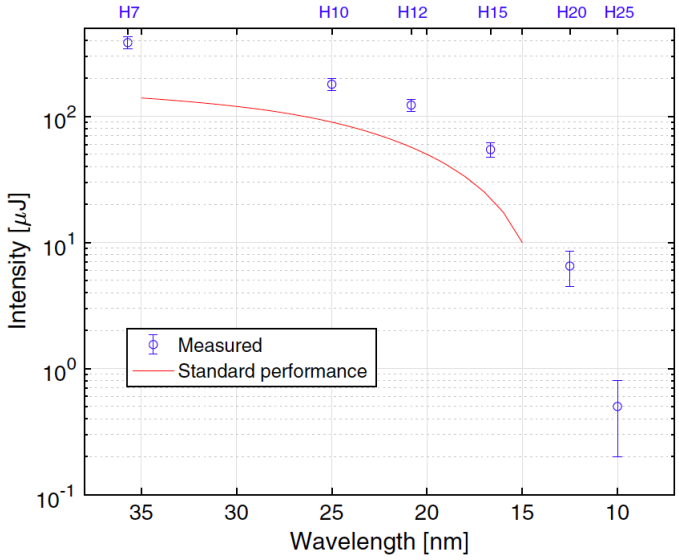

Figure 3.24: Average energy per pulse (blue dots) measured for FEL1 in circular polarization from $h = 7$ ($\sim$ 35 nm) down to $h = 25$ ($\sim$ 10 nm). Error bars correspond to the standard deviation over hundred of shots. Red line corresponds to the standard guaranteed FERMI FEL1. Image from [27]

nm ($h = 25$). The measurements down to 20 nm were carried out with the FERMI intensity monitor [105]. At shorter wavelengths, the pulse energy was estimated from the intensity of the spectrometer camera image [106], cross-calibrated with the intensity monitor. An average energy of about 0.5 μJ at 10 nm was estimated, with shots up to 1.5 μJ. The results are shown in Fig. 3.24. The red continuous line corresponds to the standard FEL pulse energy. The performances of the FEL with the cold beam significantly exceed the standard one in the whole range. Moreover, in this configuration we could measure a good signal down to 10 nm, thus extending the lasing range of FERMI FEL1.

The lower beam energy spread can be also exploited to increase the beam current with a stronger compres-

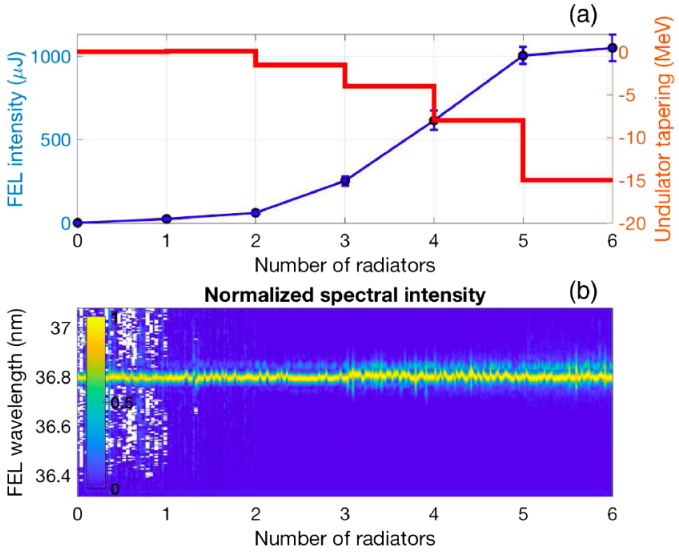

Figure 3.25: FEL gain curve for an highly compressed beam ($\sim$1.3 kA) at $h = 7$ ($\sim$ 37 nm) in circular polarization. (**a**) FEL energy growth as a function of the number of resonant undulators (blue curve) and applied tapering (red curve). (**b**) Normalized spectra along the gain curve. Image from [27]

sion. We operated the FEL with a bunch compressed by a factor 15 corresponding to a final peak current of about 1.3 kA. After optimization at $h = 7$ (*i.e.*, 37 nm) in circular polarization, the FEL intensity reached several hundreds of μJ. A taper of the final undulators and a careful optimization of the seeding parameters allowed to measure FEL pulses exceeding 1 mJ for the first time at FERMI. Taking into account the scaling law already mentioned [102], one can estimate an FEL pulse length of about 60 fs, and therefore an FEL peak power at 37 nm of about 16 GW. Figure 3.25 reports the FEL amplification (blue line) along the undulator chain, together with the energy offsets corresponding to the undulator taper (red line).
It must be noted that despite the stronger compression, only a small fraction of the bunch charge participates to lasing in a seeded FEL where the seed pulse is much shorter than the electron bunch. The energy offset of the resonance of the last radiator was 15 MeV, corresponding to more than 1% of energy loss for the emitting electrons. Considering a peak current of 1.3 kA and the mentioned energy loss, one can estimate an FEL peak power of about 20 GW, consistent with the previous estimation. Evolution of the FEL spectra as a function of the number of undulators is reported in Fig. 3.25. For each undulator setting, spectra are normalized to the corresponding maximum. This representation of the data allows identification of possible spectral structures even in case of weak spectra. Despite the very high compression and the fact that the laser heater was offline, FEL pulses show very stable and narrow spectra, without undesired features. The small sideband toward longer wavelength is expected to be the result of a combination between resonance tuning and FEL saturation." From one of my paper [27]

3.4.2 EEHG

"Echo-enabled harmonic generation free-electron lasers (EEHG FELs) is conceived as a seeding method with excellent high-harmonic conversion efficiency to generate transform-limited radiation pulses down to soft x rays [99, 107–109]. By utilizing two laser modulations and dispersive sections (DSs), a monochromatic (coherent) energy modulation is imprinted on to the relativistic electron beam and transformed to a high harmonic density modulation (see Fig. 3.26). The beam then enters the undulator radiator where the density-modulated (bunched) electrons radiate coherently at wavelengths up to ~ 100 times shorter than that of the ultraviolet (UV) seeding lasers. With sufficient gain, the radiation can be amplified up to saturation.
While EEHG is predicted to be more robust than other external seeding schemes to energy distortions that occur upstream, it is also demonstrated that distortions that occur between the EEHG chicanes can significantly impact the FEL spectrum. It is well known, in fact, that energy distortions in the electron beam can impact the EEHG bunching spectrum and, in particular, incoherent energy modulations [29, 110–112].
In what follows, we examine and compare the measured FEL performance with an analytical model that includes incoherent modulations in the electron beam longitudinal phase space that develop from the early beam acceleration process through the final EEHG transformations.

Theoretical background

The evolution of the electron beam longitudinal phase space through the EEHG line in the presence of energy distortions is described by the following equations [113, 114]

$$\begin{aligned} P_1 =& P + A_1(z)\sin(k_{s1}z) + \Delta p_1(z), \\ z_1 =& z + B_1 P_1/k_{s1}, \\ P_2 =& P_1 + A_2(z_1)\sin(k_{s2}z_1) + \Delta p_2(z_1), \\ z_2 =& z_1 + B_2 P_2/k_{s1}, \end{aligned} \tag{3.70}$$

where $A_{1,2}(z) = \Delta E_{1,2}(z)/\sigma_E$ is the normalized coherent energy modulation from seed lasers, and $B_{1,2} = k_{s1}R_{56}^{(1,2)}\sigma_E/E$ is the normalized energy dispersion in the chicanes, E is the electron beam mean energy and σ_E is the RMS slice energy spread, and $\Delta p_{1,2}(z)$ the energy distortions of the electron beam distribution.
In this description, Δp_1 represents any energy structure accumulated in the electron beam up to the entrance of the first EEHG chicane B_1. Δp_2 is used to capture the integrated effect of CSR from B_1 and of LSC in second modulator. They can be expressed as the superposition of monochromatic modulations of different

amplitudes [58, 114]:

$$\Delta p_{1,2}(z) \quad = \quad \sum_{\mu=0}^{\infty} p_{1,2}(k_\mu)\sin(k_\mu z + \phi_{1\mu,2\mu}), \tag{3.71}$$

where $\phi_{1\mu,2\mu}$ is a random phase. When the energy distortions $\Delta p_{1,2}$ are ignored and in the assumption of uniform lasers $A_{1,2}(z) = A_{1,2}$ (i.e., seed durations much longer than bunch duration), the Fourier transform of the electron beam density distribution - the so-called bunching factor - can be calculated at the exit of the second EEHG modulator according to [99]:

$$\bar{b}_{n,m}(k_E) = \mathrm{e}^{-\zeta_E^2/2} J_n(-\zeta_E A_1) J_m(-a_E A_2 B_2), \tag{3.72}$$

where $a_E = n + mk_{s2}/k_{s1}$ is the harmonic number with integer numbers n and m. The EEHG wave number is $k_E = a_E k_{s1}$, and $\zeta_E = nB_1 + a_E B_2$. This factor is known to help characterize the EEHG performance and is optimized approximately at $\zeta_E = j'_{n,1}/A_1$ where $j'_{n,1}$ is the first root of J'_n.
If the energy distortion Δp_2 and second laser A_2 are sufficiently slowly-varying longitudinally that we can approximate their functional dependence as $z_1 \approx z$, then the EEHG bunching factor close to the harmonic peak becomes [114, 115]:

$$b_{n,m}(k) = \mathrm{e}^{-\frac{1}{2}\left(\zeta_E + \frac{k-k_E}{k_{1s}} B\right)^2} \int_{-\infty}^{+\infty} dz\, f(z) J_m\left[-\frac{k}{k_{s1}} B_2 A_2(z)\right] \times$$
$$J_n\left[-\left(\zeta_E + \frac{k-k_E}{k_{s1}} B\right) A_1(z)\right] \mathrm{e}^{i(-\zeta_E \Delta p_1(z) - a_E B_2 \Delta p_2(z) + (k-k_E)z)}, \tag{3.73}$$

where $f(z)$ is electron beam density distribution function, and $B = B_1 + B_2$. In the first two gain lengths in the radiator (R in Fig.3.26) the intensity of the FEL radiation is estimated to grow like $\propto z^2 |b_{n,m}(k)|^2$. In the limit of negligible slippage the final radiation spectral pulse properties are given by $|b_{n,m}(k)|^2$. Thus, by virtue of the general expression for the energy modulations given in (3.71), this equation can be used to quantify the spectral effect of broadband energy modulations induced by MBI on the FEL output.

Bunching Phase

The z-dependent additional bunching phase due to electron beam energy distortions in Eq.(3.73) is:

$$\psi(z) = -\zeta_E \Delta p_1(z) - a_E B_2 \Delta p_2(z). \tag{3.74}$$

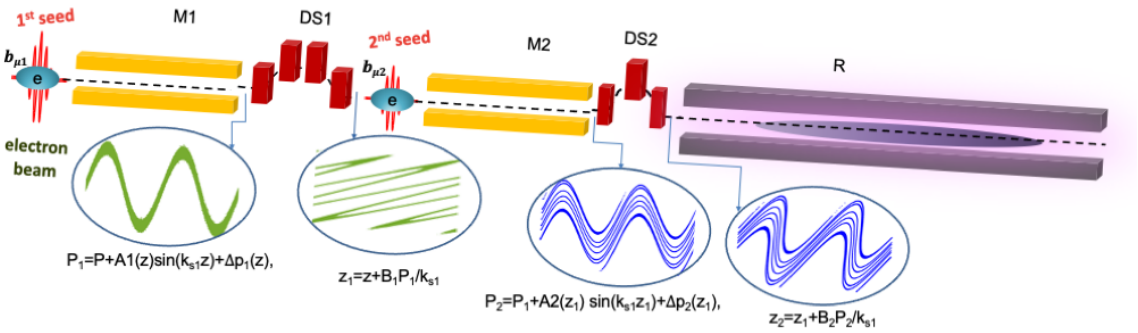

Figure 3.26: Main components of the EEHG scheme: first modulator (M1), strong first dispersive section (DS1), second modulator (M2), weaker second dispersive section (DS2). Equations refer to quantities of the electron beam longitudinal phase space introduced in eq.(3.70). In particular, $\Delta p_{1,2}$ is the incoherent energy modulation (see Eq. (3.71)) and $b_{\mu 1,\mu 2}$ is the incoherent bunching factor (see Eq. (3.9)). After DS2, the nano-bunched electron beam travels into the radiator (R) and emits coherent and powerful light pulse. Image from [29]

From this, one can obtain the moments of the spectral bunching distribution and gain insight into the relative magnitude of the contributions from $\Delta p_{1,2}$ [114].
MBI-induced energy modulations accumulated up to the exit of the first modulator, Δp_1, are multiplied by the small scaling parameter $|\zeta_E| \lesssim 1$. Linear, quadratic, and sinusoidally-shaped initial modulations were investigated in [113], where it was shown that the smallness of ζ_E accounts for the insensitivity of the EEHG bunching spectrum to small initial perturbations. However, as discussed in [114], energy modulations Δp_2 that develop between the EEHG chicanes are multiplied by the much larger factor $a_E B_2 \approx m/A_2 \gg 1$, and therefore can have a noticeable impact on the final bunching spectrum at high harmonics.
The RMS bandwidth of $|b_{n,m}(k)|^2$ in Eq.(3.73) is $\sigma_k^2 = \sigma_{ks}^2 + \sigma_{\psi'}^2$, where σ_{ks} is the transform-limited (TL) bandwidth and $\sigma_{\psi'^2} = \left\langle [\psi' - \langle \psi' \rangle]^2 \right\rangle$ is the bandwidth due to the nonlinear phase structure, where brackets denote integration over the z-dependent amplitudes in the integrand in (3.73).
Assuming the bunching longitudinal envelope is determined by the second seed laser and that it is a TL Gaussian pulse, the relative bandwidth in the case of optimized bunching absent MBI can be approximated as [115]:

$$\bar{\sigma}_{ks}^2 = \frac{4\bar{\sigma}_{ks2}^2}{3m^{4/3}}, \tag{3.75}$$

where $\bar{\sigma}_{ks2}$ is the relative bandwidth of the second seed laser.
Inserting Eq. (3.71) for broadband energy distortions into the phase in (3.74), the instantaneous spatial bunching frequency is $k_z = k_E + \psi'(z)$, where:

$$\psi'(z) = -\zeta_E \sum_{\mu=0}^{\infty} p_1(k_\mu)\, k_\mu \cos(k_\mu z + \phi_{1\mu}) - a_E B_2 \sum_{\mu=0}^{\infty} p_2(k_\mu)\, k_\mu \cos(k_\mu z + \phi_{2\mu}) \tag{3.76}$$

is the z- derivative of the additional phase. The mean bunching frequency is then $\langle k_z \rangle$. Thus, $\langle \psi' \rangle$ gives the spectral shift from k_E, and $\sigma_{\psi'}$ gives the excess bandwidth due to the distortions. Assuming that the characteristic MBI wavelengths are small compared the length of the bunching envelope (e.g, $k_\mu \gg \sigma_{ks}$) and that the individual phases $\phi_{1,2\mu}$ are uncorrelated over μ, bandwidth of $|b_{n,m}(k)|^2$ is therefore:

$$\sigma_k^2 = \sigma_{ks}^2 + \sum_{\mu=0}^{\infty} \left[\frac{\zeta_E^2}{2} (p_1(k_\mu)\, k_\mu)^2 + \frac{(a_E B_2)^2}{2} (p_2(k_\mu)\, k_\mu)^2 \right]. \tag{3.77}$$

Bunching Amplitude

Similarly to the phase, the bunching factor in Eq.(3.73) for generic energy distortions is here specialized for MBI-induced energy modulations described in Eq.(3.71). It becomes:

$$\begin{aligned} b_{n,m}(k) &= \int \chi(z,k)\, \mathrm{e}^{-i(z(k-k_E)+\psi(z))} dz \\ &= \int dz\, \chi(z,k) \prod_{\mu=0}^{\infty} \sum_{l_1=-\infty}^{\infty} \sum_{l_2==-\infty}^{\infty} J_{l_1}\left(-\zeta_E p_1(k_\mu)\right)\, J_{l_2}\left(-a_E B_2 p_2(k_\mu)\right) \times \\ &\qquad \mathrm{e}^{-iz[k_\mu(l_1+l_2)-(k-a_E k_{1s})]} \mathrm{e}^{-i(l_1\phi_{1\mu}+l_2\phi_{2\mu})}, \end{aligned} \tag{3.78}$$

where

$$\chi(z,k) = \mathrm{e}^{-\frac{1}{2}\left(\zeta_E + \frac{k-k_E}{k_{1s}} B\right)^2} J_m\left[-\frac{k}{k_{s1}} B_2 A_2(z) \right] J_n\left[-\left(\zeta_E + \frac{k-k_E}{k_{s1}} B \right) A_1(z) \right] f(z). \tag{3.79}$$

With the definition of the bunching spectrum $b_{n,m}(k)$, we can now quantify the presence of sidebands and/or of a broader spectral pedestal in EEHG. The EEHG bunching amplitude evaluated for $k = a_E k_{1s}$ can be calculated when $l_1 = -l_2$, so that:

$$b_{n,m}(a_E k_{1s}) = \grave{b}_{n,m} \prod_{\mu=0}^{\infty} \sum_{l_1=-\infty}^{\infty} (-1)^{l_1} J_{l_1}\left(-\zeta_E p_1(k_\mu)\right)\, J_{l_1}\left(-a_E B_2 p_2(k_\mu)\right) \mathrm{e}^{-il_1(\phi_{1\mu}-\phi_{2\mu})}, \tag{3.80}$$

where $\grave{b}_{n,m}$ is the z-integration of Eq.(3.79) for $k = a_E k_{1s}$ and demonstrates the bunching factor when MBI is absent. In above equation we use the Bessel function relationship for integer ν value $J_{-\nu}(x) = (-1)^{\nu} J_{\nu}(x)$. In the case of long seed lasers (i.e $A_{1,2}(z) = A_{1,2}$) and a uniform electron beam, it is easy to see that $\grave{b}_{n,m} = \bar{b}_{n,m}$. Note that the bunching is suppressed at the roots of the two Bessel functions. Assuming that the arguments of J_{l_1} in Eq.(3.80) are less than 1, the high order of Bessel functions can be ignored and the leading term can be expanded around 0. In doing so, the bunching factor can be simplified to:

$$
\begin{aligned}
b_{n,m}(a_E k_{1s}) &\approx \grave{b}_{n,m} \prod_{\mu=0}^{\infty} J_0\left(-\zeta_E p_1(k_\mu)\right) J_0\left(-a_E B_2 p_2(k_\mu)\right) \\
&\approx \grave{b}_{n,m} \prod_{\mu=0}^{\infty} \left[1 - \frac{1}{4}\left(\left(\zeta_E p_1(k_\mu)\right)^2 + \left(a_E B_2 p_2(k_\mu)\right)^2\right)\right].
\end{aligned}
\tag{3.81}
$$

Bandwidth Enlargement and Central Frequency Fluctuation

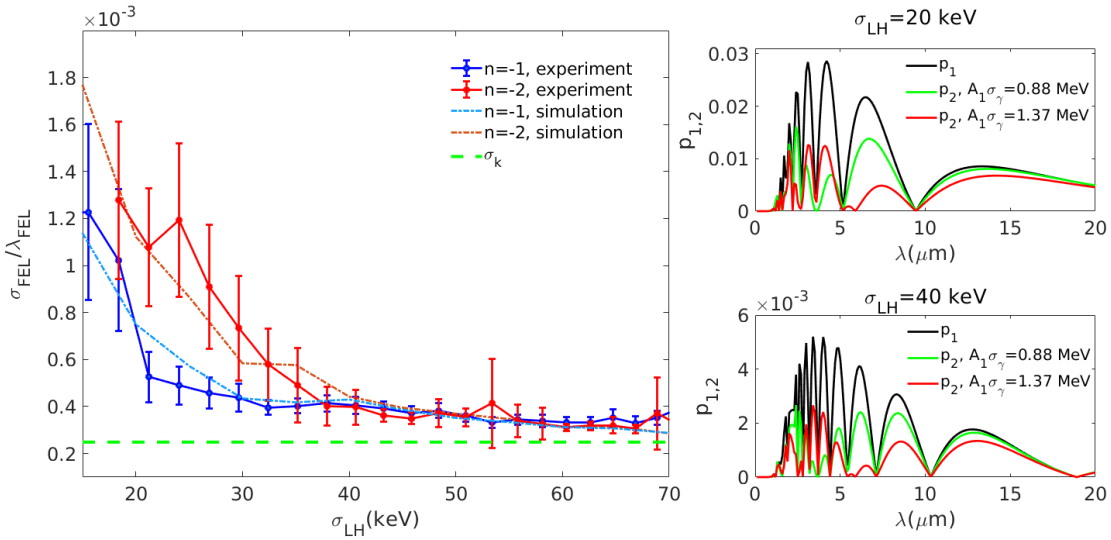

Figure 3.27: Left: Relative FEL RMS spectral bandwidth vs. LH-induced energy spread. Blue and red lines are experimental data (solid) and theoretical prediction (dashed-dotted, Eq.(3.77)) for $n = -1$ and $n = -2$, respectively. EEHG is tuned at $\lambda_{FEL} = 8.8$ nm. The dashed green line is from Eq.(3.75). In case of $n = -1$, the first seed energy is 8.3 μJ ($A_1\sigma_E = 0.88$ MeV) and for $n = -2$, it is 20 μJ ($A_1\sigma_E = 1.37$ MeV). Right: calculated energy modulation amplitude $p_1(\lambda_\mu)$ and $p_2(\lambda_\mu)$ from MBI modeling for $\sigma_{LH} = 20$ keV (top) and 40 keV (bottom). Image from [29]

The EEHG experiment was conducted with an electron beam accelerated through the FERMI linac to the final energy of E=1.32 GeV. The beam normalized emittance measured in front of the undulator amounts to approximately 1 mm mrad in both transverse planes. The electron bunch is compressed by a factor $C \sim$10 to reach a final peak current in the core of I=700 A.
Figure 3.27-left plot shows the RMS spectral bandwidth of the FEL at harmonic $a_E = 30$ of a UV seed laser ($\lambda_s = 264.54$ nm), as a function of the LH-induced energy spread. The dispersion of the first EEHG dispersive section was set to $R_{56}^{(1)} = 2.25$ mm. The blue curve shows the EEHG emission for $n = -1$ configuration or $R_{56}^{(2)} = 75$ μm; the red curve is for $n = -2$ or $R_{56}^{(2)} = 145$ μm (n defined in Eq.(3.72)). The error bars reflect the RMS fluctuation of experimental data collected over a series of 20 consecutive shots at 10 Hz machine repetition rate. The experimental data are compared with the theoretical bandwidth predicted by Eq.(3.77) for $n = -1$ and $n = -2$, illustrated by the the dashed-dotted blue and red line, respectively. For comparison, the green dashed line represents the bandwidth for optimized bunching absent MBI, Eq.(3.75), assuming TL seed laser pulses with a FWHM bandwidths of 2.01 nm and 1.35 nm, respectively.

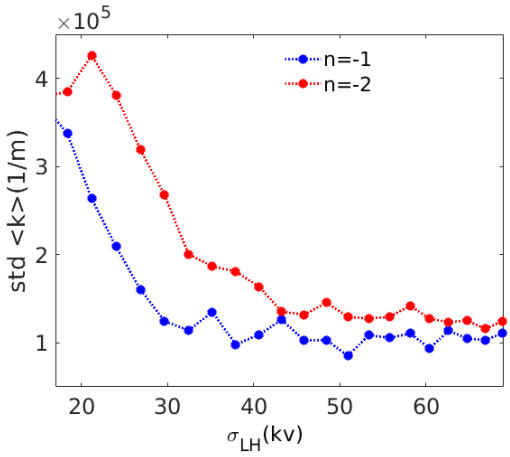

Figure 3.28: Comparison of standard deviation of frequency fluctuations of 50 shots $n = -1$ (blue) and 100 shots $n = -2$ (red) configurations in EEHG experiment with respect to the different induced LH energy spread. EEHG harmonic is 30 ($\lambda_{FEL} = 8.8$ nm). The FEL parameters are same as in Fig.3.27. Image from [29]

The spectra of the energy distortion amplitudes predicted by the MBI model for two different LH energy spread settings is shown in the right Fig. 3.27 subplots. The integrated impact of these distortions matches well the measured FEL bandwidth, which is substantially reduced for a LH-induced energy spread ≥ 30 keV. The model allows us to explain the observations on the basis of MBI-induced energy modulations augmented by the first EEHG dispersive section, where $p_2(\lambda_\mu)$ in absent of the first seed results always larger than $p_1(\lambda_\mu)$.

The different MBI sensitivity of the EEHG bandwidth for the cases $n = -1$ and $n = -2$ is explained by means of Eq.(3.77). On the one side, $p_1(\lambda_\mu)$ is multiplied by the EEHG scaling factor, which therefore can be modified to change the sensitivity of the final bunching to the electron beam energy perturbations coming from the accelerator. On the other side, $p_2(\lambda_\mu)$ is multiplied by $a_E B_2$, with $|B_2| \approx nB_1/a_E$, such that a higher value of $|n|$ forces larger values $R_{56}^{(2)}$ of the second dispersion section.
Equation (3.76) suggests that, by virtue of larger values of B_2 in the presence of MBI, frequency fluctuations in the configuration $n = -2$ for fixed ζ_E, should be larger than in $n = -1$. Figure 3.28 compares the range of the frequency fluctuation by showing the standard deviation (std) of 50 single shots of $n = -1$ (blue) and 100 shots of $n = -2$ (red) configurations in EEHG experiment at $\lambda_{FEL} = 8.8$ nm respect to the different induced LH energy spread. In other words, this figure shows the range of $\langle k_z \rangle$ fluctuations for different level of incoherent energy modulation. The larger fluctuations seen with the $n = -2$ setting align with expectations.

Pulse Intensity Reduction

Figure 3.29-top plot shows the the maximum measured FEL intensity for $n = -1$ (blue line) and $n = -2$ (red line). As mentioned the FEL intensity scales with $|b_{n,m}(k_E)|^2$. The bottom plot shows the values calculated from Eq.(3.82). The equation shows that when the MBI gain is suppressed by large LH pulse energies, the product function

$$\Gamma = \prod_{\mu=0}^{\infty} J_0\left(-\zeta_E p_1(k_\mu)\right) J_0\left(-a_E B_2 p_2(k_\mu)\right) \approx \prod_{\mu=0}^{\infty} \left[1 - \frac{1}{4}\left(\left(\zeta_E p_1(k_\mu)\right)^2 + \left(a_E B_2 p_2(k_\mu)\right)^2\right)\right] \tag{3.82}$$

tends to 1. Likewise, when the MBI is more pronounced at low LH pulse energies, the product function approaches zero. At the same time, owing to the large LH-induced energy spread (larger than 40 keV), the FEL gain is diminished and therefore the FEL intensity is reduced. We note that in the Γ function, $p_2(\lambda_\mu)$ is multiplied by $a_E B_2$, which explains the different behavior of the function for $n = -1$ and $n = -2$, in agreement with the experimental observation.

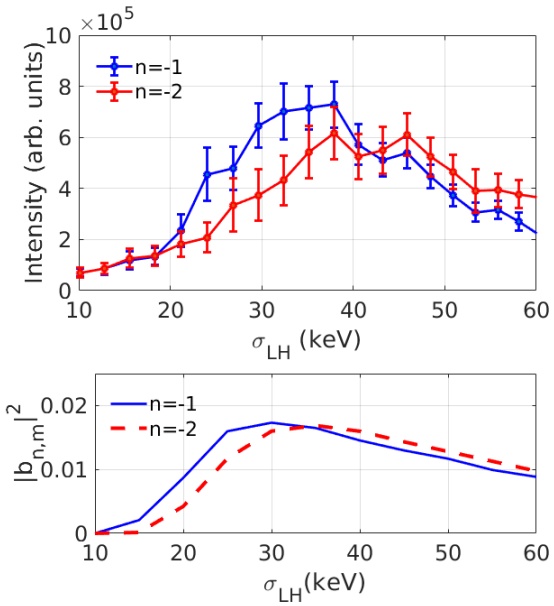

Figure 3.29: Top: FEL intensity vs. LH-induced energy spread. The FEL parameters are same as in Fig.3.27. Bottom: square bunching factor. The calculated value of $p_1(\lambda_\mu)$ and $p_2(\lambda_\mu)$ in Fig.3.27 are used to evaluate bunching factor. Image from [29]

Impact of first Seed Laser

It is well-known that in the processes of harmonic emission driven by an external laser, the seed laser-induced energy modulation has to exceed the uncorrelated energy spread of the beam at the undulator entrance. Moreover, the EEHG bunching becomes less sensitive to MBI with increased laser modulations. This leads to the question if and to what extent the seeding laser pulse energy could be increased in order to counteract the effect of MBI, before preventing any further lasing by exceeding the FEL normalized energy bandwidth.

To answer this question, Fig.3.30-left plot illustrates the FEL intensity recorded as function of the first seed laser pulse energy, for two values of the LH pulse energy. Since the bunching is more sensitive to the coherent energy modulation in the first modulator at higher harmonics, the experiment was done for harmonic 18. The beam energy was 1.1 GeV and the compression factor about 7, for approximately 550 A in the bunch core. EEHG was set in configuration $n = -1$ ($R_{56}^{(1)} = 1.9$ mm and $R_{56}^{(2)} = 98$ μm).

The figure shows that, once the FEL emission is built up for the seed laser pulse energy of $\sim$ 15-20 μJ ($A_1 \sim$ 2-4), the intensity is weakly affected by even larger seed energies. In particular, a stronger seed laser is not able to recover the intensity reduction due to a weaker heating effect. The right plots provide the theoretical explanation of the experimental data. They show the spectrum of broadband energy modulation at the exit of the second modulator for different coherent energy modulations from the first seed laser, at two LH pulse energies. The contour plots are generated by inserting the energy distribution modified by the first seed laser into Eq.(3.17), which allows us to calculate the MBI gain at the exit of the first DS. Using such spectral gain function as an input to Eq.(3.16), the spectrum of the MBI-induced broadband energy modulation at the exit of the second modulator is eventually derived as function of the first seed pulse energy. An increase of the first coherent modulation is effective in removing incoherent energy modulations at initial wavelengths shorter than 10 μm, or $\sim$1 μm at the entrance of the undulator. However, the effect becomes negligible immediately at longer wavelengths.

We plugged these two sets of energy modulation and different first seed energies into Eq.(3.72) and Eq.(3.82), thus calculated the bunching factor ($b_{-2,20}$) and the product function (Γ), see bottom plots. It is shown that, while a strong beam heating is able to shift the product function to 1 or so, an increase of A_1 is not able to recover a unitary product function (compare red starts and blue stars for $\sigma_{LH} = 16$ keV and $\sigma_{LH} = 24$ keV, respectively). The second plot of the second row compares the bunching factor with (dashed lines with stars, Eq.(3.82)) and without MBI (doted lines with circle, Eq.(3.72)). The plot illustrates the degradation of

the bunching factor by MBI, at different coherent energy modulation amplitudes from the first seed. Finally, we find that the measured FEL intensity (left plot) at the two LH pulse energies is in agreement with the theoretical behaviour of the bunching factor: by increasing the first seed energy, the FEL intensity grows up, to eventually fall down for excessive seeding energies." From one of my paper [29]

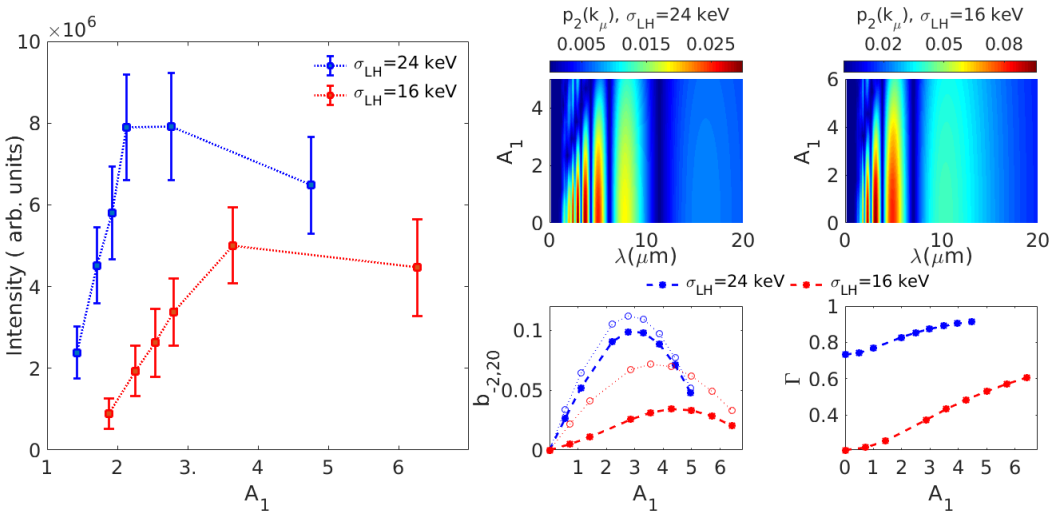

Figure 3.30: Left: FEL intensity vs. first seed laser pulse energy. Blue and red lines are experimental data for LH-induced energy spread $\sigma_{LH} = 24$ keV and $\sigma_{LH} = 16$ keV. Right-top row: beam energy modulation amplitude as function of the (compressed) MBI modulation wavelength and first seed coherent energy modulation amplitude (seed energy), at the exit of the second modulator. Right-bottom row: bunching factor and product function versus first seed coherent energy modulation amplitude. Dotted lines with circles show $\grave{b}_{-2,20}$; dashed lines with stars show $b_{-2,20}$ in Eq.(3.80). The two sub-plots refer to the LH inducing 24 keV and 16 keV RMS energy spread, respectively. Image from [29]

Brightness and Sidebands Control

"The mix of frequencies induced by microbunching instability and by the FEL coherent emission generates also shot-to-shot fluctuations of the multiline FEL spectrum [26, 49–51]. In a seeded FEL, this can be interpreted as the stochastic appearance of sidebands at frequencies [65]

$$k_{\text{FEL}} = nk_{\text{seed}} \pm mk_{\text{MBI}} \tag{3.83}$$

The spectral broadening averaged over many shots is sometimes referred to as a "pedestal." Strategies for the mitigation of the microbunching instability which do not rely on an increase of the beam energy spread would allow high-intensity FEL pulses and a stable, very narrow bandwidth. We can show that linear optics control can be an additional knob, complementary to the laser heater, for mitigation of the microbunching instability. The mitigation of the FEL sideband instability is possible by tuning the momentum compaction (or R_{56}) of a transfer line upstream of the undulator (or "spreader").
Each branch of the FERMI spreader line is made of two double bend achromatic cells separated by quadrupole magnets. The FERMI EEHG spectrum and intensity was recorded for three values of the spreader momentum compaction, i.e., $R_{56} = -2, 0, 2$ mm (four-dipole chicanes have negative R_{56} with this convention). The R_{56} along the line is shown in Fig. 3.31. For each setting of the quadrupole magnets devoted to produce a specific R_{56} value, the FEL intensity was re-optimized as a function of the electron beam optical Twiss parameters at the entrance of the undulator, seed laser parameters, and strength of the dispersive sections of the EEHG scheme. By virtue of the small correlated energy spread at the entrance of the spreader ($< 0.1\%$, rms value), the bunch length differences between datasets due to first- and higher order transport matrix terms were negligible ($< 2\%$). Finally, the spreader optics was tuned to also preserve the beam

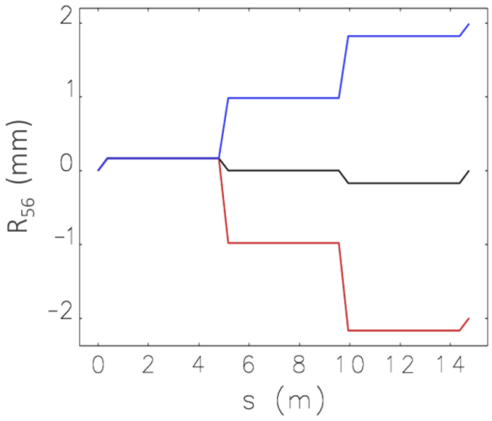

Figure 3.31: R_{56} along the spreader for three different optics. Image from [26]

bend-plane emittance from CSR emitted in the dipoles

The EEHG output was recorded on a single-shot basis at the on-line spectrometer. In the following, the

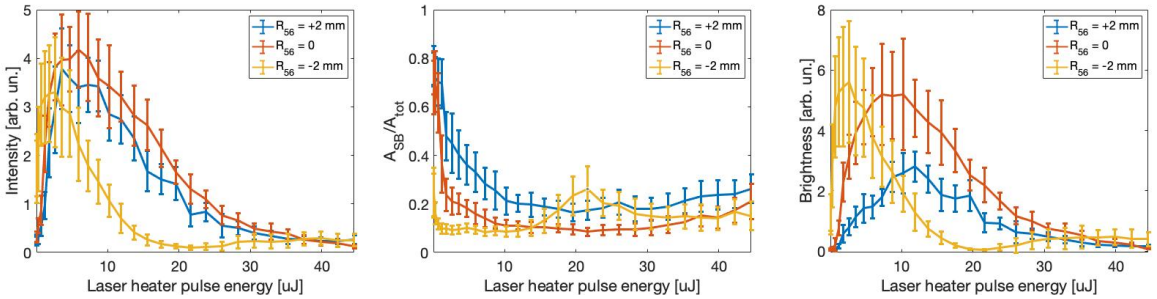

(a) (b) s (c)

Figure 3.32: EEHG signal recorded at 7.3 nm, for the three spreader optics, as a function of the laser heater pulse energy. From top to bottom: Total signal; ratio of the pedestal signal over the total FEL signal; total signal over FWHM bandwidth. All quantities are in arbitrary units. Image from [26]

FEL data refer to the average of 41 consecutive FEL shots recorded at 50 Hz. Each dataset was measured as a function of the laser heater pulse energy, as shown in Fig. 3.32a. The contribution of the pedestal to the spectrum was evaluated by fitting the central FEL line with a Gaussian. The area of the Gaussian was subtracted from the total integrated spectrum signal. Doing so, we calculated the ratio of the pedestal signal (A_{SB}) and the total FEL signal (A_tot), as shown in Fig. 3.32b. Finally, Fig. 3.32c shows the ratio of the FEL total signal and the spectral bandwidth. The latter quantity is the width of the spectrum image, corresponding to the interval containing 76% of the central profile area, in analogy to a Gaussian FWHM. Since the FEL signal is proportional to the pulse energy, and since the spatial, angular, and temporal width of the electron beam in the undulator does not change as the laser heater is varied, the quantity in Fig. 3.32c is proportional to the FEL spectral brightness (brilliance). In all plots, the error bars are dominated by fluctuations driven by electron beam shot-to-shot jitter. A closer look at the FEL spectrum at low and moderate laser heater pulse energy is given in Fig. 3.33.

Figure 3.33 highlights the improved spectral purity when passing from positive to null to negative R_{56} of the spreader line. In the latter case, however, there is no net increase of the brilliance compared to the isochronous optics, and the FEL intensity is reduced at the front of a higher spectral purity. The evident stronger dependence of the FEL intensity from the laser heater (LH) for the negative R_{56} compared to the other two cases might suggest an abrupt change of the experimental conditions, e.g., of the LH operational parameters. This has not been revealed by an analysis of the machine setting. Nevertheless, and in order to disentangle the results from the actual LH setting, an additional analysis is conducted by comparing the amount of relative FEL pulse energy distributed into the sidebands at the point of maximum FEL brilliance, *i.e.*, for the LH setting that optimizes the FEL performance in each of the three experimental sessions. The

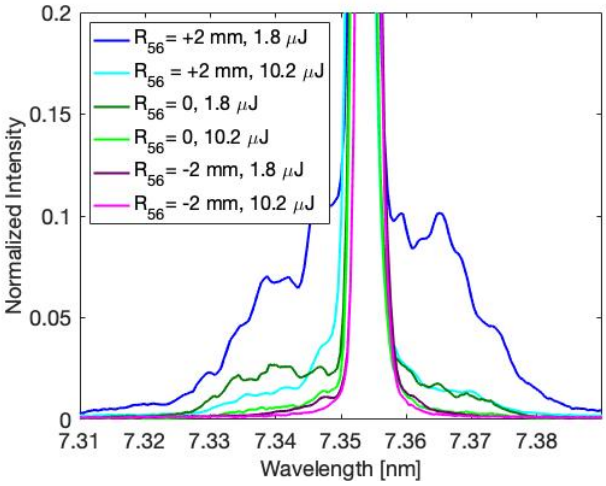

Figure 3.33: EEHG spectrum (average over 31 shots) for the three spreader optics, at two laser heater pulse energies. Image from [26]

same quantity is also calculated for the LH turned off. The results are shown in Fig. 3.34.

The trend of the experimental data with R_{56} is corroborated by a semi-analytical prediction based on the

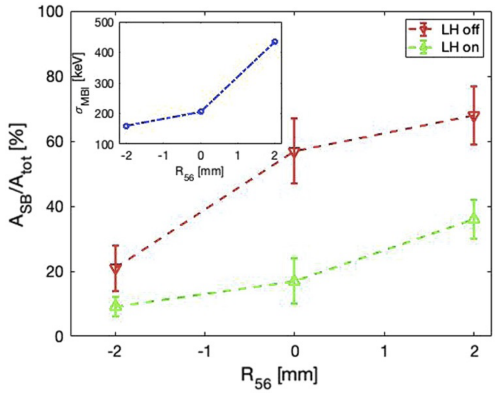

Figure 3.34: Measured average spectral area of sidebands with the laser heater turned off (red triangles) and on (green triangles), the latter being the value which maximizes the FEL brilliance. In the inset, predicted σ_{MBI} calculated for the laser heater off. Image from [26]

model for the microbunching instability introduced before [55]. Since the instability is broadband, but only modulation periods in the range $\sim$ 1-10 μm are expected to have a substantial impact on the FEL bandwidth, we collapsed the information of the microbunching instability "strength" into the spectral integral of the energy modulation curve in the aforementioned wavelength range, weighted by the instability gain [24, 58]. We refer to this quantity as σ_{MBI}. Although the calculated σ_{MBI} cannot be directly related to the measured FEL spectral purity, the weaker the instability gain is, the lower the σ_{MBI} is, and the smaller the amount of FEL energy is expected to be dispersed into sidebands.

The microbunching instability model suggests an interpretation of the experimental results for the negative R_{56} based on phase mixing [60]. When the beam reaches the spreader with a density modulation generated by the instability in the accelerator—this is the case of laser heater turned off—the longitudinal slippage of particles, generated by the nonzero R_{56} times the local energy chirp at the modulation scale, smoothens the beam longitudinal phase space. This translates into a redshift of the peak gain toward wavelengths that do not interference anymore with the FEL natural bandwidth. This picture is consistent with theoretical and numerical results reported also in Refs. [116, 117]. Contrary to energy Landau damping, the effect of phase mixing depends on the sign of R_{56}, which explains the asymmetry of the measured areas for positive and negative R_{56} values in Fig. 3.34. In general, the phase mixing has an optimal effect, i.e., R_{56} is at the op-

timum nonzero value, when the most harmful modulations incoming from the accelerator are smoothened out. Increasing further R_{56} would not provide any additional benefit, while enhancing the CSR-induced MBI due to the non-isochronous optics. Therefore, an optimum value of R_{56} is expected depending upon the actual machine configuration and the FEL wavelength range under consideration. We finally observe that, when the laser heater is turned on, phase mixing is less effective, and the sideband area in Fig. 3.34 decreases only from ~ 40 R_{56} scan, compared to a reduction from ~ 70 when the heater is off. " From one my paper [26]

3.5 Summary

In this chapter, we characterized experimentally the microbunching content in the electron beam directly and non directly. I derived analytically new formulas for the IBS-induced energy spread and couple them to microbunching instability dynamics in order to derive a comprehensive model for longitudinal phase space. The model is benchmarked with energy spread measurement and used to predict the linear MBI dynamics in dispersive sections and transport lines, with excellent agreement between the two in a vast range of machine configurations.
We exploited a 2-D Fourier analysis of the whole longitudinal phase space to demonstrate the possibility to monitor microbunching and energy modulations (shot-noise based or artificially introduced) status and evolution as a function of the machine parameters.
We showed the enhanced emission coming from a MBI-free electron beam. In such configuration, the possibility to avoid the energy spread increase due to the lack of MBI and the purity of the electron bunch nearly doubled the standard seeded FEL performance.
At the same time, we also showed the detrimental effect of MBI on a EEHG scheme, that, despite its robustness toward spurious harmonic content, is still visibly affected. In particular its brightness and bandwidth can be significantly improved when the MBI and strong energy modulations are suppressed. A possible additional knob proposed to increase the brightness was the manipulation of the optics along the long dispersive section before the undulator line. These measurements have been used also to benchmark a theoretical model for MBI evolution.

3.6 List of publications

- Brynes, A. D., Akkermans, I., Allaria, E., Badano, L., Brussaard, S., De Ninno, G., Gauthier, D., Gaio, G., Gianeesi, L., Mirian, N. S., Penco, G., **Perosa, G.**, Ribic, P. R., Setija, I., Spampinati, S., Spezzani, C., Trovó, M., Veronese, M., Williams, P.H., Wolski, A., Di Mitri, S., Characterisation of microbunching instability with 2D Fourier analysis. *Scientific Reports* **10**, 1–12 (2020).

- Brynes, A. D., Akkermans, I., Allaria, E., Badano, L., Brussaard, Danailov, M., Demidovich, A., De Ninno, G., Mirian, N. S., Penco, G., **Perosa, G.**, Ribic, P. R., Roussel, E., Setija, I., Smorenburg, P., Spampinati, S., Spezzani, C., Trovó, M., Williams, P. H., Wolski, A. and Di Mitri, S., Microbunching instability characterization via temporally modulated laser pulses. *Phys. Rev. Accel. Beams* **23**, 104401. (2020).

- Di Mitri, S., **Perosa, G.**, Brynes, A. D., Seija, I., Spampinati, S., Williams, P. H., Wolski, A., Allaria, E., Brussaard, S., Penco, G., Ribic, P. R. and Trovó, M., Experimental evidence of intrabeam scattering in a free-electron laser driver. *New Journal of Physics* **22**, 083053 (Aug. 2020).

- Di Mitri, S. & **Perosa, G.**, Electron Beam Transport in Plasma-Accelerator-Driven Free-Electron Lasers in the Presence of Coherent Synchrotron Radiation and Microbunching Instability. *Physics* **2**, 521–530. ISSN: 2624-8174. (2020).

- **Perosa, G.**, Allaria, E., Badano, L., Bruchon, N., Cinquegrana, P., Danailov, M. B., Demodovich, A., De Ninno, G., Mirian, N. S., Penco, G., Ribic, P. R., Roussel, E., Sigalotti, P., Spampinati, S., Veronese, M., Trovó, M. and Di Mitri, S., Linear optics control of sideband instability for improved free-electron laser spectral brightness. *Phys. Rev. Accel. Beams* **23**, 110703. (11 Nov. 2020).

- Penco, G., **Perosa, G.**, Allaria, E., Di Mitri, S., Ferrari, E., Giannessi, L., Spampinati, S., Spezzani, C. and Veronese, M., Enhanced seeded free electron laser performance with a "cold" electron beam. *Phys. Rev. Accel. Beams* **23**, 120704. (12 Dec. 2020).

- **Perosa, G.** & Di Mitri, S. Matrix model for collective phenomena in electron beam's longitudinal phase space. *Scientific reports* **11**, 1–10 (2021).

- Mirian, N. S., **Perosa, G.**, Hemsing, E., Allaria, E., Badano, L., Cinquegrana, P., Danailov, M. B., De Ninno, G., Giannesi, L., Penco, G., Spampinati, S., Spezzani, C., Roussel, E., Ribic, P. R., Trovó, M., Veronese, M. and Di Mitri S., Characterization of soft x-ray echo-enabled harmonic generation free-electron laser pulses in the presence of incoherent electron beam energy modulations. *Phys. Rev. Accel. Beams* **24**, 080702. (8 Aug. 2021).

- Prat, E., Craievich, P., Dijkstal, P., Di Mitri, S., Ferrari, E., Lucas, T. G., Malyzhenkov, A., **Perosa, G.**, Reiche , S. and Schietinger, T., Energy spread blowup by intrabeam scattering and microbunching at the SwissFEL injector. *Phys. Rev. Accel. Beams* **25**, 104401 (10 Oct. 2022).

Chapter 4

Quantum coherence

Because of the masslessness of photons, classical theory covers the vast majority of the festures of light. Even degrees of freedom such as spin and Orbital Angular Momentum (OAM), despite their quantized nature, can be described using the notion of classical electromagnetic fields without invoking Quantum Mechanics. However some aspects of light cannot be covered by classical theory. There are, in fact, situations in which the particle nature of light kicks in and its wave nature is no longer sufficient to describe them, the photon anti-bunching being one of the most glaring examples [33, 34, 118]. Coherence too falls under this umbrella of phenomena.
This chapter is devoted to introduce some of these aspects, focusing on the quantum states of light, the theory of quantum coherence and a reconstruction technique to retrieve or discriminate its quantum features. In particular, this method is applied to investigate, from a quantum-dynamical point of view, the photon states that can be associated with emission from SASE and seeded FELs. Via simulations, it is possible to demonstrate the capability to retrieve such states and some examples of reconstruction are shown. I prepared the simulations and the code for the reconstruction algorithm. In doing so, I determined some practical rules to run the algorithm in an efficient way. Finally, in the last part, the non-classical aspects of the light-electron interaction are investigated, deriving an evolution operator for the coupled dynamics valid for any photon and electron initial states. I conducted most of the calculations shown and, more importantly, I suggest the physical meaning of the strategy used to solve this problem. This formalism can be applied to tackle unsolved problems about the inheritance and transmission of light features via electron-photon coupling.
Overall, this chapter can be considered as the first step to answer the questions: "is it possible to introduce quantum features other in any process of harmonic generation from a coherent light pulse interacting with electrons? If yes, how could we measure them?"

4.1 Quantum theory of Coherence

Analogously to what we presented for classical fields, it is possible to construct the same formalism to describe the coherence of a quantum photon state. As already anticipated, although most of the formal expressions remain unchanged, some of their properties are different. These (sometimes) subtle differences belong therefore to a realm beyond classical electrodynamics and mandatorily involves the concept of field quantization, *i.e.* photons.
The first and most important difference in calculating the correlation functions for quantum fields is that the field components are now non-commuting operators [33, 34, 118]. These Hermitian operators are usually expressed by the sum of two non-Hermitian operators. One distinguishes between the positive frequencies and the negative frequencies components [33, 34, 118]:

$$E(\mathbf{r},t) = E_+(\mathbf{r},t) + E_-(\mathbf{r},t) \tag{4.1}$$

where

$$E_+(\mathbf{r},t) = (E_-(\mathbf{r},t))^\dagger = i\sum_{\mathbf{k}s}\sqrt{\left(\frac{\hbar\omega_{\mathbf{k}s}}{2\varepsilon_0 V}\right)}\boldsymbol{\epsilon}_{\mathbf{k}s}a_{\mathbf{k}s}\exp\{i(\mathbf{k}\cdot\mathbf{r}-\omega_{\mathbf{k}s}t)\} \tag{4.2}$$

such that the positive frequencies correspond to the absorption of a right-propagating photon annihilated by $a_{\mathbf{k}s}$ while the negative ones correspond to the emission of a left-propagating photon created by $a^\dagger_{\mathbf{k}s}$.
The annihilation and creation operators $a_{\mathbf{k}s}$ and $a^\dagger_{\mathbf{k}s}$ obey the bosonic commutation rules

$$[a_{\mathbf{k}s}, a^\dagger_{\mathbf{k}'s'}] = \delta(\mathbf{k}-\mathbf{k}')\delta_{ss'}, \quad [a_{\mathbf{k}s}, a_{\mathbf{k}'s'}] = [a^\dagger_{\mathbf{k}'s'}, a^\dagger_{\mathbf{k}'s'}] = 0. \tag{4.3}$$

The first and second order correlation functions are defined in terms of the normally ordered field operators. The normal ordering of the field operators means that all field creation operators stand to the left of all annihilation operators. The mean value in this case is calculated as

$$\langle f(\mathbf{r},t)\rangle = \mathrm{Tr}\left[\rho f(\mathbf{r},t)\right] \tag{4.4}$$

for a given state ρ and operator $f(\mathbf{r},t)$. Correlation functions of first- and second-order can be rewritten as

$$\gamma^{(1)}(x_1,x_2) = \frac{\mathrm{Tr}\left[\rho E_-(x_1)E_+(x_2)\right]}{\sqrt{\langle|E(x_1)|^2\rangle\langle|E(x_2)|^2\rangle}} \tag{4.5}$$

$$\gamma^{(2)}(x_1,x_2) = \frac{\mathrm{Tr}\left[\rho E_-(x_1)E_-(x_2)E_+(x_2)E_+(x_1)\right]}{\langle|E(x_1)|^2\rangle\langle|E(x_2)|^2\rangle}. \tag{4.6}$$

Although correlation functions are constructed in the same way, only first-order coherence is equivalent for quantum and classical electrodynamics, since from phase interference it is not possible to distinguish them. The correspondence is no longer true already for the second-order correlation function [34]. From the mathematical point of view, this is because of the non-commutativity of operators that prevents the existence of a correspondence, except for the first-order. Phenomena like the two- or single-photon interference pattern cannot be observed with classical fields [34].
To make explicit the operatorial dependence on the annihilation and creation operators, we can substitute the definitions (4.2) into the correlation functions. For simplicity, we limit ourselves to the single-mode case, and find

$$\gamma^{(1)}(x_1,x_2) = \frac{\langle a^\dagger(x_1)a(x_2)\rangle}{\langle a^\dagger a\rangle} \tag{4.7}$$

$$\gamma^{(2)}(x_1,x_2) = \frac{\langle a^\dagger(x_1)a^\dagger(x_2)a(x_2)a(x_1)\rangle}{\langle a^\dagger a\rangle^2} \tag{4.8}$$

where we used the short-hand notation $a(x) = ae^{ikx}$ for the Heisenberg representation of the operator.

4.1.1 Second order correlation function

In the classical interpretation of second-order coherence, the correlation function is a measure of the statistical correlation of electromagnetic waves with fluctuating intensity that leads to the discrimination between chaotic and coherent classical light. Passing from the formalism of fields to the concept of particles, $\gamma^{(2)}$ quantifies the coincidence count of one photon (therefore the conditional probability) after a certain amount of time from the detection of a previous one. This is true also in the case of zero delay, meaning that with an intensity interferometer we can access temporal coincidence counts of light states. In general, the violation of one of the two main properties of the second-order coherence function, namely equations 2.12, is the strongest indication of non-classical behavior of state. As we are going to see, $\gamma^{(2)}(0)$ is not always enough to discriminate different behaviors and categorize them.
Firstly, this parameter can be related to the variance of photon number [33, 34, 118]

$$\gamma^{(2)}(0) = \frac{\langle a^\dagger a^\dagger aa\rangle}{\langle a^\dagger a\rangle^2} = \frac{\langle n^2\rangle - \langle n\rangle}{\langle n\rangle^2} = \frac{(\Delta n)^2 + \langle n\rangle^2 - \langle n\rangle}{\langle n\rangle^2} = 1 + \frac{(\Delta n)^2 - \langle n\rangle}{\langle n\rangle^2} \tag{4.9}$$

The condition under which the correlation function is equal to 1 is $(\Delta n)^2 = \langle n\rangle$, relation in a one-to-one correspondence with the Poisson distribution. As we are going to show here and in the following sections, poissonianity could be used as an index for coherent states.
A state for which $\gamma^{(2)}(0) > 1$ is a classical state, in the sense that there exist a correspondence between the photon state described by ρ and a classical field with the same statistical properties. In this case, we talk

about super-poissonian states, since the condition $\gamma^{(2)}(0) > 1$ is realized for distribution with a variance bigger than a poissonian curve with the same mean number of photons, $(\Delta n)^2 > \langle n \rangle$.
Differently from the classical counterpart, the operatorial form of $\gamma^{(2)}(0)$ could in principle be less than 1, when a state has $(\Delta n)^2 < \langle n \rangle$. Since this is something that a classical field could not display, the states belonging to this specific category do not have a classical counterpart. In analogy to what we have defined before, we can term such states as sub-poissonian light. In this sense, poissonianity is not only an index to determine the proximity to the perfect coherence, but also a way to discriminate between classicality and quantumness of a light state.
We can interpret this results in terms of *photon bunching* [33, 34, 118]: having $\gamma^{(2)}(0) > 1$, as in the case of chaotic light ($\gamma^{(2)}(0) = 2$), can be explained assuming that photons travel in space grouped together, otherwise the presence of coincidence count cannot be explained. At the same time, having $\gamma^{(2)}(0) < 1$, corresponds to an anti-correlation, linked to the tendency of photon in this state to travel well-separated. We can therefore talk about photon bunching or anti-bunching, labeling in this way the likelihood of a light source to deliver grouped or regular bunch of photons. It is important to stress that anti-bunched light can occur whenever the condition of monotonicity of $\gamma^{(2)}$ is violated and therefore is not a synonym for sub-poissonian light. The quantum formulation of coherence enriches the plethora of classical phenomena beyond the sub-poissonianity statistics and anti-bunched light.
The most important examples are the two- and single photon interference patterns. In the former case, two single-mode fields of equal frequencies and polarizations is considered. Such state is the tensor product of two Fock states, indicated with $|1, 1\rangle$, and the equal time second-order correlation function is

$$\gamma^{(2)}(0) = \frac{\langle 1, 1|n^2|1, 1\rangle - \langle 1, 1|n|1, 1\rangle}{\langle 1, 1|n|1, 1\rangle^2} = \frac{1}{2}. \tag{4.10}$$

This means that the interference intensity pattern, even at second order, is perfectly visibile, *i.e.* $C^{(2)} = 1$, contrary to the limitation given in the classical case ($C^{(2)} < 1/2$). This is true even when the two photons are produced by two independent sources [34].
What about Dirac's remark "*Interference between different photons never occurs*"? Particles do not interfere, as correctly stated by Glauber, but probability amplitude does [119]. We can accept the synecdoche of saying that two photons interfere, meaning that the probability amplitude, adding up as a complex number, could generate interference.
Finally, single photon interference, is even more subtle: in a first-order (phase) interference experiment, a single photon state would behave as a classical field. In fact, the interferometric patterns are equivalently determined by the superposition of complex probability amplitudes or the amplitudes of complex classical modes, even for non-classical states [120]. Yet, anti-correlation is still present and discriminates between a classical and quantum realm. In an intensity-correlation measurement for a single photon state, $\gamma^{(2)}(0) = 0$, meaning that there is a perfect anti-correlation, symptom of non-classicality of the input state [121].

4.2 Quantum states of light

In this section we present a survey of quantum states of light that are relevant for describing the vast majority of light encountered in our studies and their properties.
A monochromatic, linearly polarized plane-wave of frequency ω is described by single-mode creation and annihilation operators a and $a^\dagger$ satisfying the commutation relations $[a\,,\,a^\dagger] = 1$. The absence of photons of frequency ω is associated with the vacuum state $|0\rangle$ which is annihilated by the annihilation operator: $a|0\rangle = 0$, whereas the so-called number state, or Fock state, describing n photons with frequency ω is obtained by acting n times on the vacuum with the creation operator $a^\dagger$:

$$|n\rangle = \frac{(a^\dagger)^n}{\sqrt{n!}}|0\rangle\,. \tag{4.11}$$

The number states are orthogonal $\langle n|m\rangle = \delta_{nm}$ and such that

$$a\,|n\rangle \;=\; \sqrt{n}\,|n\rangle\,, \qquad a^\dagger|n\rangle \;=\; \sqrt{n+1}\,|n+1\rangle\,, \tag{4.12}$$

whence they possess definite photon number $N = a^\dagger a$ and thus definite energy $E = \omega N$ ($\hbar = 1$):

$$N\,|n\rangle \;=\; n\,|n\rangle\,. \tag{4.13}$$

To the other extreme with respect to Fock states, one finds the so-called coherent states $|\alpha\rangle$, with complex amplitudes $\alpha \in \mathbb{C}$; they are eigenstates of the annihilation operator and their intensities are given by the their mean photon number:

$$a\,|\alpha\rangle = \alpha\,|\alpha\rangle\ , \quad |\alpha|^2 = \langle\alpha|a^\dagger\,a|\alpha\rangle\ , \tag{4.14}$$

where we can introduce the displacement operator $D(\alpha)$

$$D(\alpha) = \mathrm{e}^{\alpha\,a^\dagger\,-\,\alpha^*\,a} = \mathrm{e}^{-|\alpha|^2/2}\,\mathrm{e}^{\alpha\,a^\dagger}\,\mathrm{e}^{-\alpha^*\,a} \tag{4.15}$$

such that, acting on the vacuum state, the operator displaces it

$$D(\alpha)\,|0\rangle = |\alpha\rangle\,. \tag{4.16}$$

Any quantum state of light described by mode-operators a and $a^\dagger$ is representable as a density matrix ρ acting on the Fock space space spanned by the number states, which in that representation reads:

$$\rho = \sum_{k,\ell} \rho_{k\ell}\,|k\rangle\langle\ell|\ , \quad \rho_{k\ell} = \langle k|\rho|\ell\rangle\ . \tag{4.17}$$

In turn, any such density matrix can always be written as [39]:

$$\rho = \int_{\mathbb{C}} \mathrm{d}^2\alpha\,\mathcal{P}_\rho(\alpha)\,|\alpha\rangle\langle\alpha| \quad \text{with} \quad \int_{\mathbb{C}} \mathrm{d}^2\alpha\,\mathcal{P}_\rho(\alpha) = 1 \tag{4.18}$$

where $\mathcal{P}_\rho(\alpha)$ is the so-called Glauber-Sudarshan P-function (see e.g. [32] for details) associated with the quantum state ρ and the integration is performed with respect to the real and imaginary parts of $\alpha = \alpha_x + i\alpha_y$, $\mathrm{d}^2\alpha = \mathrm{d}\alpha_x\,\mathrm{d}\alpha_y$.
Therefore any single-mode state of light reads as a linear combination of projectors $|\alpha\rangle\langle\alpha|$ onto coherent states with a function $\mathcal{P}_\rho(\alpha)$ that, though being normalized, need not necessarily amount to a smooth probability distribution over the complex plane. Indeed, $\mathcal{P}_\rho(\alpha)$ may not only degenerate into a highly singular distribution, but even become non-positive. As a consequence, a quantum state of light is said to be

- classical if the Glauber–Sudarshan P-function is a *bona fide* distribution

$$\mathcal{P}_\rho(\alpha) \geq 0\ , \tag{4.19}$$

  with $\mathcal{P}_\rho(\alpha)$ a smooth function or no more singular than a Dirac delta.

For instance, as we are going to see, for coherent states, that is when $\rho = |\beta\rangle\langle\beta|$, $\mathcal{P}_\rho(\alpha)$ reduces to a Dirac delta $\delta^2(\alpha) = \delta(\alpha_x)\delta(\alpha_y)$ on the complex plane, while, for thermal states $\mathcal{P}_\rho(\alpha)$ reduces to a Gaussian distribution. Instead, a quantum state of light is called

- non-classical or, in other words, genuinely quantum, if the function $\mathcal{P}_\rho(\alpha)$ is either non-positive

$$\mathcal{P}_\rho(\alpha) \ngeq 0, \tag{4.20}$$

  or more singular than a Dirac delta distribution.

Indeed, the non-classical behavior of Fock number states is accompanied by a highly singular distributional Glauber-Sudarshan $\mathcal{P}_\rho$ function, as shown in Appendix B,

$$\mathcal{P}_n(\alpha) = \frac{\mathrm{e}^{|\alpha|^2}}{n!}\,\frac{\partial^{2n}}{\partial_\alpha^n\partial_{\alpha^*}^n}\,\delta^2(\alpha)\ . \tag{4.21}$$

The P-function being an increasingly (with n) singular distribution, its behavior has to be tested by integration against suitably differentiable trial functions $g(\alpha,\alpha^*)$ vanishing at infinity, that is by computing

$$\mathcal{P}_n[g] = \int_{\mathbb{C}^2} \mathrm{d}^2\alpha\,\mathrm{d}^2\alpha^*\,\mathcal{P}_n(\alpha)\,g(\alpha,\alpha^*) = \frac{\mathrm{e}^{|\alpha|^2}}{n!}\,\frac{\partial^{2n} g(\alpha,\alpha^*)}{\partial_\alpha^n\partial_{\alpha^*}^n}\ . \tag{4.22}$$

Evidently, these integrations can yield negative values even for positive trial functions, thus the P-function $\mathcal{P}_n(\alpha)$ cannot be a positive distribution, whence the Fock number states are highly non-classical.
We shall now examine some quantum states associated with different degrees of coherence and discuss which ones among them are good candidates for the quantum description of the radiation emitted by SASE and seeded-FELs. Technical details on how to derive their mathematical properties are given in the Appendices.

Coherent states and laser radiation As we have seen in (4.14), coherent states are eigenstates of the annihilation operator and have thus the following expansion over the orthonormal basis of number states (4.15):

$$|\alpha\rangle = \mathrm{e}^{-|\alpha|^2/2} \sum_{n=0}^{\infty} \frac{\alpha^n}{\sqrt{n!}} \, |n\rangle \ , \quad \alpha \in \mathbb{C} \, , \tag{4.23}$$

whence the associated number or energy distribution is Poissonian:

$$|\langle n|\alpha\rangle|^2 = \mathrm{e}^{-|\alpha|^2} \frac{|\alpha|^{2n}}{n!} \ . \tag{4.24}$$

Though their quantum granularity is embodied by the Poissonian distribution (4.24), coherent states $\rho_\gamma = |\gamma\rangle\langle\gamma|$ are nevertheless classical according to the definition comprising equation (4.19). Indeed, (see Appendix B), their Glauber-Sudarshan P-function $\mathcal{P}_\gamma(\alpha)$ (4.18) is a Dirac delta at the point γ in the complex plane:

$$\mathcal{P}_\gamma(\alpha) = \delta^2(\alpha - \gamma) \, . \tag{4.25}$$

Given the complex amplitude $\alpha = \alpha_x + i\alpha_y$, its phase-angle $\varphi = \arctan \alpha_y/\alpha_x$ cannot be determined; therefore, the states of monochromatic laser light are obtained by averaging uniformly over all possible φ. Such a procedure yields a uniform mixture of coherent states, but also a Poissonian mixture of number state projectors [122]. Writing $\alpha_\varphi = \alpha \, \mathrm{e}^{i\varphi}$, $\alpha \geq 0$,

$$\begin{aligned} \rho_L &= \frac{1}{2\pi} \int_0^{2\pi} \mathrm{d}\varphi \, |\alpha_\varphi\rangle \, \langle\alpha_\varphi| = \mathrm{e}^{-\alpha^2} \sum_{m,n=0}^{\infty} \frac{\alpha^{m+n}}{\sqrt{m!n!}} \, |n\rangle \, \langle m| \, \frac{1}{2\pi} \int_0^{2\pi} \mathrm{d}\varphi \, \mathrm{e}^{i\varphi(n-m)} \\ &= \mathrm{e}^{-\alpha^2} \sum_{n=0}^{\infty} \frac{\alpha^{2n}}{n!} \, |n\rangle \, \langle n| \, . \end{aligned} \tag{4.26}$$

As the name suggests, these states satisfies the Glauber criterion for coherence and it is possible to demonstrate that, $\forall n$,

$$|\gamma^{(n)}(x_1, ..., x_{2n})| = 1. \tag{4.27}$$

Since they share this property, such states can be considered as the quantum counterpart of a classical plane wave. As stated before, poissonianity of such states becomes the discriminant between classical (super-poissonian) and quantum (sub-poissonian) behavior and also an index for proximity to coherence.

Single mode thermal light A single mode thermal state of light at temperature T is described by the Gibbs density matrix (setting the Boltzmann constant $\kappa_B = 1$)

$$\rho_T = \left(1 - \mathrm{e}^{-\omega/T}\right) \mathrm{e}^{-\omega/T \, a^\dagger \, a} = \frac{1}{1+n_T} \sum_{n=0}^{\infty} \left(\frac{n_T}{1+n_T}\right)^n \, |n\rangle\langle n| \ , \ n_T \equiv \langle N \rangle = \frac{1}{\mathrm{e}^{\omega/T} - 1} \ . \tag{4.28}$$

As regards the thermal Glauber-Sudarshan P-function, one gets a P-function which is a Gaussian distribution (see (B.12) in Appendix B) so that the corresponding quantum state can thus be interpreted as a classical one:

$$\mathcal{P}_T(\alpha) = \frac{1}{\pi} \frac{\mathrm{e}^{-\frac{|\alpha|^2}{n_T}}}{n_T} \ . \tag{4.29}$$

Indeed, thermal light can be seen as a mixture of coherent states with respect to a Gaussian distribution in the amplitude modulus $|\alpha| = \sqrt{\alpha_x^2 + \alpha_y^2}$ of the amplitude $\alpha = |\alpha| \, \mathrm{e}^{i\varphi} = \alpha_x + i\alpha_y$ and a uniform distribution with respect to the phase-angle $\varphi = \arctan \alpha_y/\alpha_x$:

$$\rho_T = \int_{\mathbb{R}^2} \mathrm{d}\alpha_x \mathrm{d}\alpha_y \, \frac{\mathrm{e}^{-(\alpha_x^2+\alpha_y^2)/n_T}}{\pi n_T} \, |\alpha_x + i\alpha_y\rangle\langle\alpha_x + i\alpha_y| \, . \tag{4.30}$$

Finally, if one computes

$$\langle N^2 \rangle = \frac{\mathrm{e}^{\omega/T} + 1}{\left(\mathrm{e}^{\omega/T} - 1\right)^2} \ , \quad \text{and, as a consequence} \quad \langle N^2 \rangle - \langle N \rangle = 2 \, \langle N \rangle^2 \ , \tag{4.31}$$

the second expression in (4.31) can be rewritten to express the variance of a thermal source:

$$(\Delta n)^2 = \langle N^2\rangle - \langle N\rangle^2 = \langle N\rangle^2 + \langle N\rangle. \tag{4.32}$$

Recalling the relation (4.9) between variance and second order coherence function, we see that

$$\gamma^{(2)}(0) = 1 + \left(\frac{\langle N\rangle^2 + \langle N\rangle - \langle N\rangle}{\langle N\rangle^2}\right) = 2, \tag{4.33}$$

meaning that thermal light is not only classical, but corresponds to classical chaotic light.

Displaced thermal states The randomness of thermal states expressed by their Gaussian Glauber-Sudarshan P-function can be diminished by displacing them via the displacement operators $D(\alpha)$ in (4.15):

$$\rho_{T,\alpha} := D(\alpha)\,\rho_T\,D^\dagger(\alpha)\,. \tag{4.34}$$

Indeed, coherent states can also be obtained by displacing the vacuum state, $|\alpha\rangle = D(\alpha)|0\rangle$; therefore, by means of $D(\alpha)$, thermal states acquire a coherent contribution; this is particularly evident for vanishing temperatures, when n_T vanishes as well and thermal states behave as the vacuum state which is turned into a fully coherent state by $D(\alpha)$ as in (4.16). A more formal characterizaton of this interpretation follows by using (4.30) and (B.5) in the next section; indeed, one gets

$$\rho_{T,\alpha} = \int_{\mathbb{C}} \mathrm{d}^2\beta \frac{\mathrm{e}^{-|\beta|^2/n_T}}{\pi n_T}\,|\alpha+\beta\rangle\langle\alpha+\beta| = \int_{\mathbb{C}} \mathrm{d}^2\beta \frac{\mathrm{e}^{-|\beta-\alpha|^2/n_T}}{\pi n_T}\,|\beta\rangle\langle\beta|\,, \tag{4.35}$$

where one sees that the displacement introduces a coherent bias into the Gaussian distribution that originates chaotic thermal light.
A concrete consequence of this coherent bias emerges when one looks at the mean energy which also gets a coherent contribution; indeed, using (4.15), one computes

$$\langle a^\dagger a\rangle = \mathrm{Tr}\left(\rho_{T,\alpha}\,a^\dagger a\right) = n_T + |\alpha|^2\,. \tag{4.36}$$

4.2.1 Displaced thermal states representation

Sometimes, instead of their Glauber-Sudarshan representation in terms of projectors onto coherent states, it proves convenient to represent quantum states by means of their characteristic function $\mathrm{Tr}(\rho\,D(-\alpha))$ and of the displacement operators. In the case of thermal states, this representation reads

$$\rho_T = \int_{\mathbb{C}} \mathrm{d}^2\beta\,\frac{1}{\pi}\mathrm{e}^{-|\beta|^2\,(\frac{1}{2}+n_T)}\,D(\beta)\,, \tag{4.37}$$

whence, using the algebraic relation (B.5), it yields

$$\rho_{T,\alpha} = \int_{\mathbb{C}} \mathrm{d}^2\beta\,\frac{1}{\pi}\mathrm{e}^{-|\beta|^2\,(\frac{1}{2}+n_T)}\,\mathrm{e}^{\beta\alpha^*-\beta^*\alpha}D(\beta) \tag{4.38}$$

for displaced thermal states. These representations are obtained by firstly noticing that any single-mode density matrix ρ can be written as

$$\rho = \int_{\mathbb{C}} \frac{\mathrm{d}^2\beta}{\pi}\,\mathrm{Tr}\left(\rho\,D^\dagger(\alpha)\right)\,D(\alpha)\,. \tag{4.39}$$

This follows from using (B.5) and the overcompleteness relation (B.2) to prove that

$$\mathrm{Tr}\left(D^\dagger(\beta)\,D(\alpha)\right) = \int_{\mathbb{C}} \frac{\mathrm{d}^2\gamma}{\pi}\,\langle\gamma|D^\dagger(\beta)\,D(\alpha)|\gamma\rangle = \pi\,\delta^2(\alpha-\beta)\,.$$

Then, using the P-function (4.29) and the Glauber-Sudarshan representation together with the coherent state overcompleteness and Gaussian integration, yield

$$\mathrm{Tr}\left(D^\dagger(\beta)\,\rho_T\right) = \frac{1}{\pi\,n_T}\int_{\mathbb{C}} \mathrm{d}^2\gamma\,\mathrm{e}^{-|\gamma|^2/n_T}\,\langle\gamma|D^\dagger(\beta)|\gamma\rangle = \exp\left(-|\beta|^2\Big(\frac{1}{2}+n_T\Big)\right)\,. \tag{4.40}$$

Given a displacement operator $D(\alpha)$ and a coherent state $|\beta\rangle = D(\beta)|0\rangle$ (see (B.3)), using (B.2) and then (4.23), one computes in two ways the scalar products with Fock number states $|n\rangle$, $a^\dagger a\,|n\rangle = n\,|n\rangle$:

$$\begin{aligned}\langle n|D(\alpha)|\beta\rangle &= \mathrm{e}^{(\alpha\beta^*-\alpha^*\beta)/2}\,\langle n|D(\alpha+\beta)|0\rangle = \frac{(\alpha+\beta)^n}{\sqrt{n!}}\,\mathrm{e}^{-(|\alpha|^2+|\beta|^2+2\alpha^*\beta)/2}\\ &= \mathrm{e}^{-|\beta|^2/2}\sum_{m=0}^{\infty}\frac{\beta^m}{\sqrt{m!}}\,\langle n|D(\alpha)|m\rangle\ .\end{aligned}$$

It thus follows that

$$(\alpha+\beta)^n\,\mathrm{e}^{-\alpha^*\beta} = \mathrm{e}^{|\alpha|^2/2}\sum_{m=0}^{\infty}\sqrt{\frac{n!}{m!}}\beta^m\,\langle n|\,D(\alpha)\,|m\rangle\ .$$

By setting $\beta = \alpha\,y$, the equality reads

$$(1+y)^n\,\mathrm{e}^{-y|\alpha|^2} = \sum_{m=0}^{\infty}\left(\mathrm{e}^{|\alpha|^2/2}\,\alpha^{m-n}\sqrt{\frac{n!}{m!}}\,\langle n|\,D(\alpha)\,|m\rangle\right)\,y^m\ ,$$

whose right hand side is recognizable as one of the generating functions of the associated Laguerre polynomials $L_n^{(\alpha)}(y)$ [123],

$$(1+t)^\lambda\,\mathrm{e}^{-xt} = \sum_{m=0}^{\infty}L_m^{(\lambda-m)}(x)\,t^m\ .$$

The identification

$$\mathrm{e}^{|\alpha|^2/2}\alpha^{m-n}\sqrt{\frac{n!}{m!}}\,\langle n|D(\alpha)|m\rangle = L_m^{(n-m)}(|\alpha|^2) \tag{4.41}$$

finally yields

$$\langle n|D(\alpha)|m\rangle = \mathrm{e}^{-|\alpha|^2/2}\alpha^{n-m}\sqrt{\frac{m!}{n!}}\,L_m^{(n-m)}(|\alpha|^2)\ . \tag{4.42}$$

From (4.37) and (4.42) one gets

$$\begin{aligned}\rho_{T,\alpha}(n) &= \langle n|\rho_{T,\alpha}|n\rangle = \int_{\mathbb{C}}\mathrm{d}^2\beta\,\frac{1}{\pi}\mathrm{e}^{-|\beta|^2\,(\frac{1}{2}+n_T)}\,\mathrm{e}^{\beta\alpha^*-\beta^*\alpha}\langle n|D(\beta)|n\rangle\\ &= \int_{\mathbb{C}}\mathrm{d}^2\beta\,\frac{1}{\pi}\mathrm{e}^{-|\beta|^2\,(\frac{1}{2}+n_T)}\,\mathrm{e}^{\beta\alpha^*-\beta^*\alpha}\mathrm{e}^{-|\alpha|^2/2}\,L_n(|\alpha|^2)\ ,\end{aligned} \tag{4.43}$$

where $L_n(x) = L_n^{(0)}(x)$ are the Laguerre polynomials.

By passing to polar coordinates, $\mathrm{d}^2\beta = r\mathrm{d}r\mathrm{d}\varphi$ and setting $\alpha = |\alpha|\mathrm{e}^{i\psi}$, one rewrites

$$\rho_{T,\alpha}(n) = \int_0^\infty\frac{\mathrm{d}}{\pi}\,r\,\mathrm{e}^{-r^2(1+n_T)}\,L_n(r^2)\,\int_0^{2\pi}\mathrm{d}\varphi\,\mathrm{e}^{2ir|\alpha|\,\sin(\varphi-\psi))}\ . \tag{4.44}$$

The last integral equals the Bessel function $J_0(2r|\alpha|)$ so that one can use the relation [123]

$$\int_0^{+\infty}\mathrm{d}x\,x\,\mathrm{e}^{-\alpha x^2/2}\,L_n(\beta x^2/2)\,J_0(xy) = \frac{(\alpha-\beta)^n}{x^{n+1}}\,\mathrm{e}^{y^2/(2\alpha)}\,L_n\left(\frac{\beta y^2}{2\alpha(\beta-\alpha)}\right)$$

and get

$$\rho_{T,\alpha}(n) = \left(\frac{n_T}{1+n_T}\right)^n\,\frac{\mathrm{e}^{-\frac{|\alpha|^2}{1+n_T}}}{1+n_T}\,L_n\left(-\frac{|\alpha|^2}{n_T(1+n_T)}\right)\ .$$

4.3 No-click quantum state reconstruction

The quantum nature of light is mostly encoded in the photon statistics. A very satisfactory reconstruction of the statistics quantum optical states may be obtained exploiting the counts of on/off detectors operating in the Geiger mode [9, 124, 125]. In such setup, as the name suggests, the outcome of a measurement could be either a click ("on") if one or more photons are detected or an "off-click", corresponding to the absence

of photons.
Since this kind of measurement has a binary outcome, it is possible to associate two projection operators to the measuring process:

$$\Pi_0 = |0\rangle\langle 0| \tag{4.45}$$

$$\Pi_1 = \sum_{n=1}^{\infty} |n\rangle\langle n|. \tag{4.46}$$

The first corresponds to the projection onto Fock subspace without photons, i.e. the vacuum, while the second is the projection onto the subspace spanned by occupied photon states. Following the Born rule, the probability of measure absence of photons, for an ideal detector is given by

$$P_0 = \Pi_0[\rho] = \sum_n \sum_m \rho_{nm}\langle n|0\rangle\langle 0|m\rangle = \rho_{00}. \tag{4.47}$$

However, real detectors are inevitably affect by imperfections, and therefore are characterized by a detection efficiency η always smaller than 1. For this reason, the projection on the vacuum $|0\rangle$ is modified and the probability of no-click is given by

$$P_0(\eta) = \Pi_0(\eta)[\rho] = \sum_{n=0}^{\infty}(1-\eta)^n \rho_n. \tag{4.48}$$

As a consequence, no-click probability carries information about the diagonal terms of the density matrix, since it can be expressed as a linear combination of them. From now on, we make the reasonable assumption that there exist a number $\tilde{n}$ such that ρ_n is negligible when $n > \tilde{n}$. The use of different detection efficiencies η_ν, with $\nu = 1, .., L$, can be exploited to define a statistical model for $\{\rho_n\}$:

$$P_\ell(\{\rho_n\}_n) = \sum_{k=0}^{N}(1-\eta_\ell)^k \rho_k \ , \quad \ell = 1, 2, \ldots, L \ . \tag{4.49}$$

We now illustrate, from the analytical point of view, how the structure of a photon state diagonal with respect to the number representation can be reconstructed by means of the empirically measured probability of no-click events from photodetectors in on/off experiments with varying detector efficiencies η.

4.3.1 Monochromatic light

We first consider the case of a single mode radiation, a monochromatic beam of photons of frequency ω described by a density matrix as in (4.17). If photons are detected by L detectors with different efficiencies $\eta_1, \eta_2, \ldots, \eta_L$, one collects L linear equations

$$P_\ell(\{\rho_n\}_n) = \sum_{k=0}^{N}(1-\eta_\ell)^k \rho_k \ , \quad \ell = 1, 2, \ldots, L \ , \tag{4.50}$$

that, as we shall presently show, can be used to infer the N unknown parameters ρ_n via a Maximum Likelihood method.

Remark 1 *The number L of efficiencies to be considered has to be evaluated in reference with the specific reconstruction problem: in the case of visible light, as well as in the case of the simulations discussed in the main text, $L = 20$ appears to be sufficient. The fact that the number N of unknowns is larger than the number of equations L makes the problem underestimated with a non-unique solution, in general. This issue can be overcome with an external energy constraint as discussed below.*

For each efficiency η_ℓ one counts the no-click events $\mathcal{N}_\ell$ out of a total number $\mathcal{N}$ of impinging photons coming from a radiation beam described by a state ρ, thus collecting L empirical frequencies

$$f_\ell := \frac{\mathcal{N}_\ell}{\mathcal{N}} \ . \tag{4.51}$$

Usually, once the empirical frequencies f_ℓ of a set of independent events x_ℓ are measured, the event probabilities $p_\ell := p(x_\ell)$ are derived from the log-likelihood function

$$L(\{p_n\}_n, \{f_n\}_n, \lambda) = \frac{1}{\mathcal{N}} \log \prod_\ell (p_\ell)^{\mathcal{N}_\ell} \, + \, \lambda \Big(\sum_\ell p_\ell - 1 \Big) \, , \tag{4.52}$$

where the Lagrange multiplier λ ensures normalization. Then, maximizing with respect to the unknown p_ℓ one gets

$$\partial_{p_\ell} L(\{p_n\}_n, \{f_n\}_n, \lambda) = \frac{f_\ell}{p_\ell} \, + \, \lambda = 0 \, , \tag{4.53}$$

whence, from $\sum_\ell f_\ell = 1 = \sum_\ell p_\ell$, one retrieves $\lambda = -1$ and $p_\ell = f_\ell$, as expected.
In the case of (4.50), the unknown parameters to be found by optimization are the populations ρ_n of the n-photon states, given the overall radiation state ρ. Then, one firstly introduces the normalized no-click probabilities

$$\widetilde{P}_\ell(\{\rho_n\}_n) := \frac{P_\ell(\{\rho_n\}_n)}{P(\{\rho_n\}_n)} \, , \quad \text{where} \quad P(\{\rho_n\}_n) := \sum_{\ell=1}^{L} P_\ell(\{\rho_n\}_n) \, , \tag{4.54}$$

and then the log-likelihood

$$L\left(\{\rho_n\}_n, \{f_n\}_n, \lambda\right) := \sum_{\ell=1}^{L} f_\ell \, \log \widetilde{P}_\ell(\{\rho_n\}_n) \, + \lambda \Big(\sum_{n=1}^{N} \rho_n - 1 \Big) \, . \tag{4.55}$$

Setting $\partial_{\rho_n} L\left(\{\rho_n\}_n, \{f_n\}_n, \lambda\right) = 0$, from $\sum_{k=0}^{N} \rho_k = 1$, one obtains $\lambda = 0$ and the following N equalities

$$\frac{P(\{\rho_n\}_n)}{F} \sum_{\ell=1}^{L} \frac{(1-\eta_\ell)^n}{\sum_{k=1}^{L}(1-\eta_k)^n} \, \frac{f_\ell}{P_\ell(\{\rho_n\}_n)} = 1 \, , \qquad F := \sum_{\ell=1}^{L} f_\ell, \quad n = 1, 2, \ldots, N \, . \tag{4.56}$$

Setting

$$\rho'_k = \frac{F}{P(\{\rho_n\}_n)} \, \rho_k \Longrightarrow P_\ell(\{\rho'_n\}_n) = \frac{F}{P(\{\rho_n\}_n)} \, P_\ell(\{\rho_n\}_n) \tag{4.57}$$

one recasts (4.56) as

$$\sum_{\ell=1}^{L} \frac{(1-\eta_\ell)^n}{\sum_{k=1}^{L}(1-\eta_k)^n} \, \frac{f_\ell}{P_\ell(\{\rho'_n\}_n)} = 1 \, , \tag{4.58}$$

where the quantities ρ'_k are positive but not normalized:

$$\sum_{k=1}^{N} \rho'_k = \frac{F}{P(\{\rho_n\}_n)} \neq 1 \, . \tag{4.59}$$

Notice that the equality (4.56) can be turned into a fixed point relation

$$\sum_{\ell=1}^{L} \frac{(1-\eta_\ell)^p}{\sum_{k=1}^{L}(1-\eta_k)^p} \, \frac{f_\ell}{P_\ell(\{\rho'_n\}_n)} \rho'_p \, = \, \rho'_p \, , \tag{4.60}$$

whence the probabilities

$$\rho_p = \frac{\rho'_p}{\sum_{k=0}^{N} \rho'_k} \tag{4.61}$$

can be achieved by the iteration procedure

$$\sum_{\ell=1}^{L} \frac{(1-\eta_\ell)^p}{\sum_{j=1}^{L}(1-\eta_j)^p} \, \frac{f_\ell}{P_\ell(\{\rho_n(h)\})_n} \, \frac{\rho_p(h)}{\sum_{k=1}^{N} \rho_k(h)} \, = \, \rho_p(h+1) \, , \tag{4.62}$$

where $\rho_p(h) / \sum_{k=0}^{N} \rho_k(h)$ are the probabilities at the h-th iteration step.
Due to the fact that in general the number of efficiencies L is much smaller than the number N of probabilities to be determined, the linear problem (4.50) is underestimated. Especially in the multi-mode case to

be treated in the next section, it could happen that more than one diagonal distribution $\{\rho_n\}_n$ may fit the same experimental no-click probabilities. In order to sort the true distribution out, it proves convenient to constrain the energy through one more Lagrange multiplier β, changing the functional $L\left(\{\rho_n\}_n, \{f_n\}_n, \lambda\right)$ in (4.55) into

$$L_\beta\left(\{\rho_n\}_n, \{f_n\}_n, \lambda\right) := L\left(\{\rho_n\}_n, \{f_n\}_n, \lambda\right) + \beta\Big(\sum_{k=1}^{N} k\,\rho_k - E\Big)\,. \tag{4.63}$$

The optimization procedure leads to the following constrained version of (4.56)

$$\frac{P(\{\rho_n\}_n)}{F}\sum_{\ell=1}^{L}\frac{(1-\eta_\ell)^p}{\sum_{k=1}^{L}(1-\eta_k)^p - \frac{P(\{\rho_n\}_n)}{F}\beta(p-E)}\,\frac{f_\ell}{P_\ell(\{\rho_n\}_n)} = 1\,. \tag{4.64}$$

Then, the reconstruction algorithm proceeds as above, iteratively tuning β starting from $\beta = 0$ as suggested in [125], in order to eliminate configurations not compatible with the mean energy E.

4.3.2 Multi-mode case

In the non-monochromatic case, let us suppose the beam contains $M > 1$ different independent modes corresponding to photons with M different frequencies $\omega_1, \omega_2, \ldots, \omega_M$. The quantum state of the beam is then factorized:

$$\rho = \bigotimes_{j=1}^{M}\rho^{(j)}\,, \tag{4.65}$$

where $\rho^{(j)}$ denotes the state associated with the j-th mode. Given a same detector efficiency η for all modes, the joint probability of having $\bar{n}$ photons distributed over the M modes together with no clicks reads

$$\Pi_{\bar{n}}(M,\eta) = \sum_{n_1+n_2+\cdots+n_M=\bar{n}}\left[\prod_{j=1}^{M}(1-\eta)^{n_j}\rho_{n_j}^{(j)}\right]\,, \tag{4.66}$$

where n_j, $j = 1, 2, \ldots, M$, is the occupation number of the mode of frequency ω_j, $\rho_{n_j}^{(j)}$ is the probability of having n_j photons with that frequency in the state $\rho^{(j)}$ and the summation is over all possible occupation numbers of those modes conditioned on the total number of photons being $\bar{n}$. Then, the total probability of no-clicks is given by

$$P_M(\eta) = \sum_{\bar{n}=0}^{\infty}\Pi_{\bar{n}}(M,\eta)\,, \tag{4.67}$$

Notice that normalization asks for

$$\sum_{\bar{n}=0}^{\infty}\sum_{n_1+n_2+\cdots+n_M=\bar{n}}\left[\prod_{j=1}^{M}\rho_{n_j}^{(j)}\right] = 1\,,$$

whence as in the one-mode case, one chooses a suitable accuracy parameter ϵ and truncates the summation at $\bar{n}_{max}$ such that

$$\sum_{\bar{n}=0}^{\bar{n}_{max}}\sum_{n_1+n_2+\cdots+n_M=\bar{n}}\prod_{j=1}^{M}\rho_{n_j}^{(j)} \geq 1-\epsilon\,. \tag{4.68}$$

Then, varying over a number of quantum efficiencies $\eta_1, \eta_2\ \ldots, \eta_L$, $L \geq \bar{n}_{max}$, one obtains the following multimode system of equations similar to (4.50):

$$P_M(\eta_j) = \sum_{\bar{n}=0}^{\bar{n}_{max}}\Pi_{\bar{n}}(M,\eta_j)\,,\quad j = 1, 2, \ldots, L\,. \tag{4.69}$$

The recursive algorithm can then reproduce the probabilities $\Pi_{\bar{n}}(M,\eta_j)$ by means of the no-click probabilities $P_M(\eta_j)$ after renormalization as in (4.54).

Notice that, by recursion, the probabilities $\Pi_{\bar{n}}(\eta)$ can be turned into discrete nested convolutions

$$\Pi_{\bar{n}}(M,\eta) = \sum_{n_1=0}^{\bar{n}} (1-\eta)^{n_1} \rho_{n_1}^{(1)} \, \Pi_{\bar{n}-n_1}(M-1,\eta) \tag{4.70}$$

$$= \sum_{n_1=0}^{\bar{n}} \sum_{n_2=0}^{\bar{n}-n_1} (1-\eta)^{n_1+n_2} \, \rho_{n_1}^{(1)} \rho_{n_2}^{(2)} \, \Pi_{\bar{n}-n_1-n_2}(M-2,\eta) \tag{4.71}$$

$$= (1-\eta)^{\bar{n}} \sum_{n_1=0}^{\bar{n}} \sum_{n_2=0}^{\bar{n}-n_1} \cdots \sum_{n_{M-1}=0}^{\bar{n}-\sum_{k=1}^{M-2} n_k} \prod_{j=1}^{M} \rho_{n_j}^{(j)} \, , \quad n_M = \bar{n} - \sum_{j=1}^{M-1} n_j \, . \tag{4.72}$$

Multi-mode coherent states

As a concrete case, let us imagine that the photons are in coherent states of amplitudes α_j relative to the modes in the beam; namely, from (4.24), the occupation numbers read

$$\rho_{n_j}^{(j)} = \mathrm{e}^{-|\alpha_j|^2} \, \frac{|\alpha_j|^{2n_j}}{n_j!} \, . \tag{4.73}$$

In such a case, from (4.72) and (4.67) one obtains

$$\Pi_{\bar{n}}(M,\eta) = (1-\eta)^{\bar{n}} \mathrm{e}^{-\sum_{j=1}^{M} |\alpha_j|^2} \sum_{n_1=0}^{N} \sum_{n_2=0}^{N-n_1} \cdots \sum_{n_{M-1}=0}^{\bar{n}-\sum_{k=1}^{M-2} n_k} \prod_{j=1}^{M} \frac{|\alpha_j|^{2n_j}}{n_j!} \tag{4.74}$$

$$= \mathrm{e}^{-\sum_{j=1}^{M} |\alpha_j|^2} \, \frac{(1-\eta)^{\bar{n}}}{\bar{n}!} \left(\sum_{k=1}^{M} |\alpha_j|^2 \right)^{\bar{n}} \, , \quad n_M = \bar{n} - \sum_{j=1}^{M-1} n_j \, , \tag{4.75}$$

namely a damped Poisson distribution, whence the no-click probabilities are the multimode Gaussians

$$P_M(\eta) = \sum_{\bar{n}=0}^{\bar{n}_{max}} \Pi_{\bar{n}}(M,\eta) \simeq \mathrm{e}^{-\eta \sum_{j=1}^{M} |\alpha_j|^2} \, . \tag{4.76}$$

It is important to emphasize that the above result also holds when the coherent state projections $\rho^{(j)}$ are replaced by the uniform phase-averages ρ_L in (4.26); indeed, both these states have the same diagonal elements in the Fock number state representation. Therefore, $P_M(\eta)$ in (4.76) represents the no-click probability for a multi-mode laser beam.

Multimode-displaced thermal states

Let us suppose that the M-mode state consist of thermal states ρ_{T,α_j} at a same temperature T but displaced by different amplitudes α_j. The single-mode occupation probability of the n-th Fock number state is (see Section 4.2.1)

$$\rho_{T,\alpha}(n) = \left(\frac{n_T}{1+n_T} \right)^n \frac{\mathrm{e}^{-\frac{|\alpha|^2}{1+n_T}}}{1+n_T} \, L_n \left(-\frac{|\alpha|^2}{n_T(1+n_T)} \right) \, , \tag{4.77}$$

where $L_n(x) = L_n^{(0)}(x)$ are the Laguerre polynomials.

Insert the displaced thermal states ρ_{T,α_j} in the place of all $\rho^{(j)}$ in (4.70) and consider the last sum over n_{M-1}:

$$\Sigma_M := \sum_{n_{M-1}=0}^{\bar{n}-\sum_{k=1}^{M-2} n_k} \rho_{n_{M-1}}^{(M-1)} \rho_{\bar{n}-\sum_{k=1}^{M-1} n_k}^{(M)} \, .$$

Using (4.77), one obtains

$$\Sigma_M = \frac{1}{(1+n_T)^2} \, \mathrm{e}^{-2\frac{|\alpha|^2}{1+n_T}} \left(\frac{n_T}{1+n_T} \right)^{\bar{n}-\sum_{k=1}^{M-2} n_k} \times$$

$$\times \sum_{n_{M-1}=0}^{\bar{n}-\sum_{k=1}^{M-2} n_k} L_{n_{M-1}} \left(-\frac{|\alpha_{M-1}|^2}{n_T(1+n_T)} \right) L_{\bar{n}-\sum_{k=1}^{M-2} n_k - n_{M-1}} \left(-\frac{|\alpha_M|^2}{n_T(1+n_T)} \right) \, .$$

Using the sum rule [123]

$$L_n^{(\alpha+\beta+1)}(x+y) = \sum_{k=0}^{n} L_k^{(\alpha)}(x)\, L_{n-k}^{(\beta)}(y)\ , \tag{4.78}$$

one finally gets

$$\Sigma_M = \frac{1}{(1+n_T)^2}\, \mathrm{e}^{-2\frac{|\alpha|^2}{1+n_T}} \left(\frac{n_T}{1+n_T}\right)^{\bar{n}-\sum_{k=1}^{M-2} n_k} L^{(1)}_{\bar{n}-\sum_{k=1}^{M-2} n_k - n_{M-1}} \left(-\frac{|\alpha_{M-1}|^2 + |\alpha_M|^2}{n_T(1+n_T)}\right)\ . \tag{4.79}$$

Iterating this procedure yields

$$\Pi_{\bar{n}}(M,\eta) = \frac{1}{(1+n_T)^M}\, \mathrm{e}^{-\frac{\sum_{j=1}^{M}|\alpha_j|^2}{1+n_T}} \left(\frac{(1-\eta)n_T}{1+n_T}\right)^{\bar{n}} L_{\bar{n}}^{(M-1)}\left(-\frac{\sum_{j=1}^{M}|\alpha_j|^2}{n_T(1+n_T)}\right)\ . \tag{4.80}$$

Thence the no-click probability at efficiency η results

$$P_M(\eta) \simeq \sum_{\bar{n}=0}^{\infty} P_{\bar{n}}^{(M)}(\eta) = \frac{1}{(1+\eta n_T)^M}\, \exp\Big(-\frac{\eta\, \sum_{j=1}^{M}|\alpha_j|^2}{1+\eta\, n_T}\Big)\ . \tag{4.81}$$

The last equality follows from using the associated Laguerre polynomials generating the equation

$$(1-t)^{-1-\lambda}\, \exp\Big(-\frac{x\,t}{1-t}\Big) = \sum_{n=0}^{\infty} L_n^{(\lambda)}(x)\, t^n\ . \tag{4.82}$$

4.4 SASE and Seeded FEL states reconstruction

"Coherence of SASE and seeded FEL radiation has been investigated experimentally [8, 19, 20], focussing upon the Glauber correlation functions, revealing typical chaotic light behaviour in the first case and values of $|g_2|$ rather close to 1 in the second one. We instead propose to shift the focus from Glauber correlation functions to reconstructing the statistical properties of the FEL radiation related to the photon occupation numbers [9]. This shift would then provide a first step towards a reliable investigation of the quantum signatures of FEL light, ultimately able to discriminate between Poissonian and non-Poissonian features.
As we have seen, the presence of Poissonian statistics, though not sufficient, would in any case provide solid ground to attributing "lasing properties" to the mechanism behind the generation of radiation by relativistic electrons wiggling in a series of magnetic devices. It would also give support to the conjecture that the lasing properties are imprinted upon the seeded-FEL radiation by the coherence features of the seeding pulse. From a more general perspective, the consequences of the confirmation of the lasing properties of the seeded FEL light will be of two types: it will open the way to experiments in quantum optics with X-ray radiation and it will foster the experimental investigation of light-matter interactions in the high energy quantum regime.
However, photon-counting techniques have many drawbacks in the X-ray regimes and, in general, if the average number of photons increases, as in the case of high intensity sources, photon counting becomes challenging, even for attenuated FEL radiation. We therefore resort to the approach described above to retrieve the actual photon number distribution.
As explained in the introduction of this chapter, simulations has been used in order to test the algorithm. Once the input quantum state ρ^{in} has been established, the first step consists in the computation of the no-click probabilities. Since the problem is one-dimensional, the simplest way to generate observations of the distribution $P_\ell(\{\rho_j\}_j)$ is the rejection sampling technique [126]. The occurrences of generated points, normalized to the total number of data, coincides with the desired no-click frequencies f_ℓ. From datasets of thousands of values, we extract a subset of L elements with the corresponding efficiencies. In the following examples, L is chosen to be equal to 20. Such choice is consistent with previous use of the algorithm [124, 125]. The range of selected efficiencies is chosen more carefully, avoiding region in which the off-probability is flat. This condition translates in the exclusion of points with a low Fisher information. With the aim of mimicking a real experiment, small random perturbations were added to the no-click frequencies. The stability of the algorithm has been tested also corrupting the simulated frequencies with systematic perturbations. The iteration procedure in (4.62) is fed with the off-click probabilities and $\rho_n(0)$, i.e. the

starting quantum state, taken as a uniform distribution. As suggested in [125], the value of constraint β is found starting from 0 and tuning it to discard solutions whose energies do not match with the theoretical value E. Finally, the similarity of the photon distribution reconstructed by the algorithm and the theoretical one is evaluated by means of the "fidelity" index:

$$F = \sum_{j=1}^{N} \sqrt{\rho_j^{in} \rho_j^{out}}. \tag{4.83}$$

The algorithm was applied to two distinct dataset scenarios. The datasets parameters were chosen in adherence to the performance of a short wavelength high gain free-electron laser, run in SASE [45, 127] and external seeding mode [2], respectively. The FEL pulse photon distribution is assumed to be captured in proximity of power saturation in both regimes.
In the following, left plots display a comparison between simulated, reconstructed and theoretical off-click frequencies, while right plots compare reconstructed and theoretical photon distributions.
EUV seeded FELs are ideally capable of producing Fourier-transform limited light pulses, thus a single

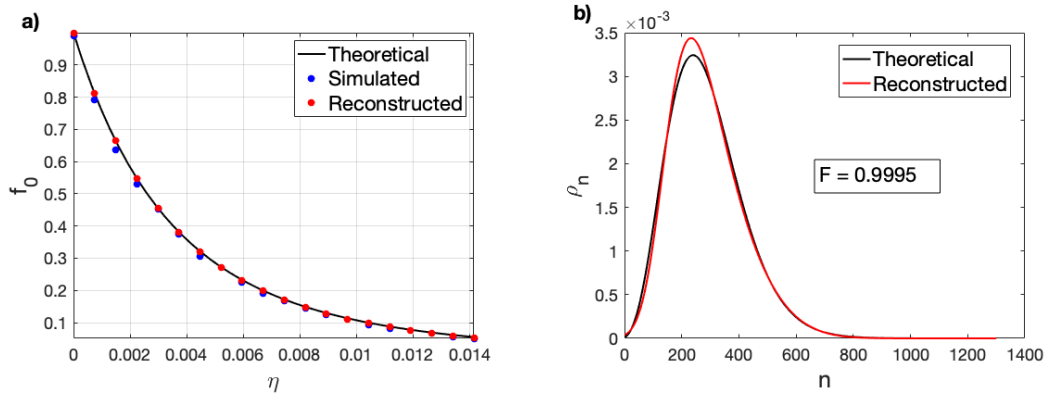

Figure 4.1: Left plot: off-click frequencies f_ℓ given by single mode-displaced thermal state $\alpha = 16$, $n_T = 30$ as a function of the efficiency η. Blue dots are the simulated frequencies, obtained with the sampling rejection technique; red dots are outputs of the reconstruction algorithm; the solid line corresponds to (4.81) with M equal to 1 and the parameters shown before. Right plot: red line is the reconstructed photon distribution and black line is the photon distribution given by (4.77). Fidelity F is also shown. Image from [9]

transverse and longitudinal mode. The natural relative spectral bandwidth can be as low as 10^{-4} [10, 11]. In practice, micron-scale modulations of the electrons' energy distribution, accumulated during the acceleration process, can add a statistically meaningful pedestal to the FEL spectrum [26, 49–51]. The ideal and the perturbed seeded FEL performance is represented in our algorithm through a single mode-displaced thermal state ($M = 1, \alpha = 16$), and a multi-mode-displaced thermal state ($M = 3, \alpha = 7, 8, 12$). In both cases, $n_t = 30$. The algorithm-reconstructed no-click frequencies and photon distribution are compared with theoretical and simulated data in Figures 4.1 and 4.2.
SASE FELs are driven by shot noise in the electron distribution. Spontaneous undulator radiation is amplified and, eventually, a large number of longitudinal modes - each individually coherent - is emitted. A single transverse mode is selected by the amplification process in proximity of saturation [128]. The number of longitudinal modes is basically given by the portion of bunch length contribution to FEL emission (~ 100 μm) divided by the FEL coherence length [129] ($\sim 1 - 3$ μm in EUV).
The SASE FEL is therefore modeled with $M = 30$ and randomly distributed displacements. Moreover, two thermal configurations were considered to test the algorithm: in the first example α_j are chosen in the interval $1 - 8$ with $n_t = 10$ and in the interval $1 - 5$ with $n_t = 100$ in the second one. Results are shown in Figures 4.3 and 4.4.
The overall procedure requires less than 200 iterations, to reach a fidelity level $L = (1 - F)$ better than 10^{-4}. Similarly high fidelity levels have been obtained for a larger number of datasets (not shown), so demonstrating the capability of the algorithm in retrieving the input state in a wide range of configurations.
" From one of my paper [9]

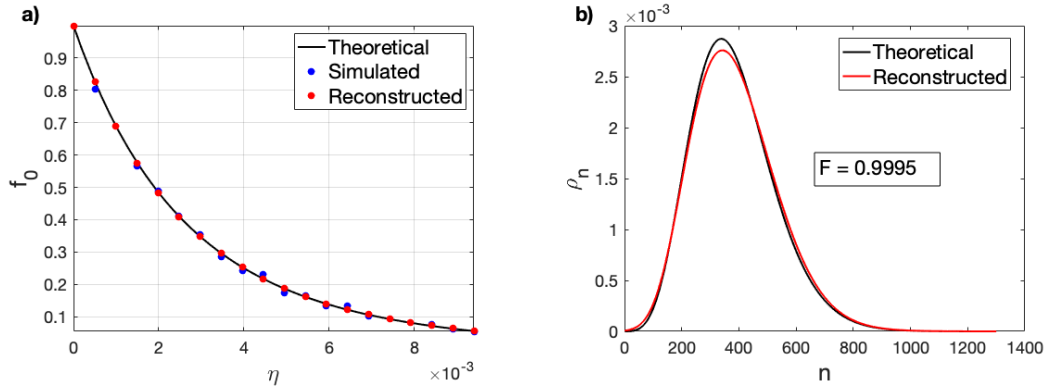

Figure 4.2: Left plot: off-click frequencies f_ℓ given by multimode-displaced thermal state, $M = 3$, $\alpha = [7, 8, 12]$ and $n_T = 30$, as a function of the efficiency η. Blue dots are the simulated frequencies, obtained with the sampling rejection technique; red dots are outputs of the reconstruction algorithm; the solid line corresponds to (4.81) substituting the parameters shown before. Right plot: red line is the reconstructed photon distribution and black line is the photon distribution given by (4.77). Fidelity F is also shown. Image from [9]

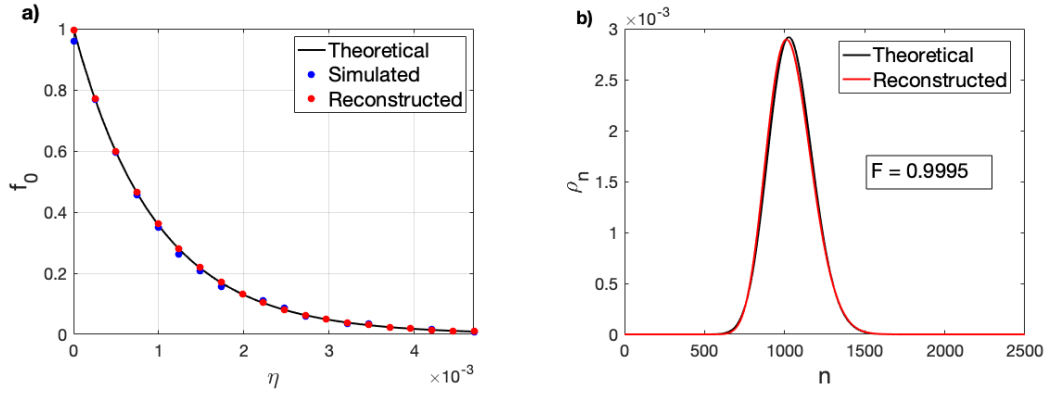

Figure 4.3: Left plot: off-click frequencies f_ℓ given by multimode-displaced thermal state, $M = 30$, α_j chosen randomly in the range $[1, 8]$ and $n_T = 10$, as a function of the efficiency η. Blue dots are the simulated frequencies, obtained with the sampling rejection technique; red dots are outputs of the reconstruction algorithm; the solid line corresponds to (4.81) substituting the parameters shown before. Right plot: red line the reconstructed photon distribution and black line is the photon distribution given by (4.77). Fidelity F is also shown. Image from [9]

4.5 Non-classicality in light-electron interaction

The interaction of a laser pulse with a free charge is an issue that has been studied for decades. Nevertheless, it continues to show new and fascinating aspects. Among other open questions, only recently the one concerning the possibility of transferring the quantum properties of a laser field, e.g., quantum statistics and/or quantum squeezed states, to a free electron, has been raised. Addressing this problem will unlock the gate for understanding if the quantum behavior of an original laser field can be transferred, to some extent, to a free electron and eventually to the final electromagnetic radiation re-emitted by it.

The foundation of the theory of laser-assisted phenomena, ranging from strong fields limit of quantum electrodynamics (QED) to light-matter interaction and manipulation, resides in the description of the interaction of electromagnetic radiation with electric charges and fields. In this context, the Dirac equation becomes the basis to describe both free electrons and electrons in matter.

This is a well established strategy for both free and bounded charges: in the former it is the natural language to investigate the high-energy perturbation provided by lasers; in the latter, there is a plethora of low energy systems that behaves as relativistic Dirac or Majorana fermions [130].

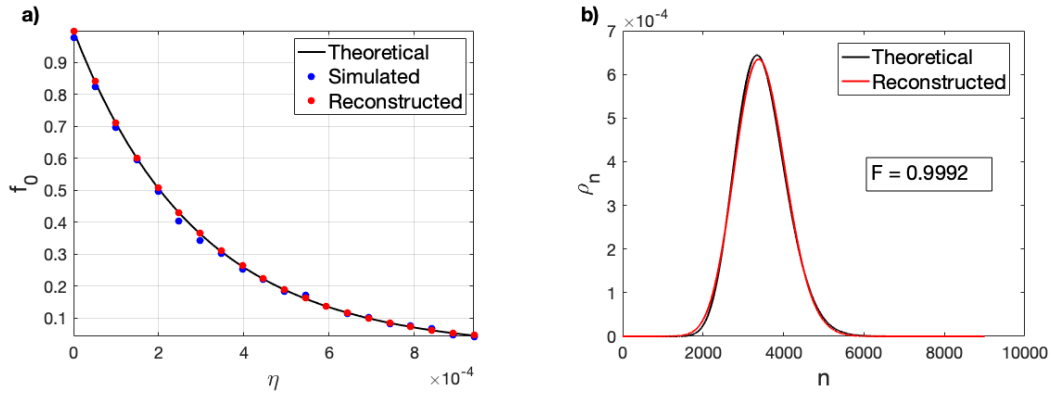

Figure 4.4: Left plot: off-click frequencies f_ℓ given by multimode-displaced thermal state, $M = 30$, α_j chosen randomly in the range $[1, 5]$ and $n_T = 100$, as a function of the efficiency η. Blue dots are the simulated frequencies, obtained with the sampling rejection technique; red dots are outputs of the reconstruction algorithm; the solid line corresponds to (4.81) substituting the parameters shown before. Right plot: red line is the reconstructed photon distribution and black line is the photon distribution given by (4.77). Fidelity F is also shown. Image from [9]

Volkov was the first to find an exact solution for a Dirac electron with given momentum in a classical plane wave field [131]. Its solution still plays a pivotal role in the modeling of electrons in electromagnetic fields or electromagnetic background, such as in the "Furry picture" or strong fields limit of QED. Several authors started to extend his treatment using the second quantization approach for the plane field [132] or applying the language of group [133] and representation theory [134] to deepen the physics hidden behind the Volkov ansatz and the importance of the spin-field interaction [135].
Here, our aim is to extend previous works describing the interaction of an electronic wave packet with a quantized plane wave field. Differently from other references, we propose to solve the Dirac equation to admit a more general initial conditions for both light and electron. In fact, the analytical solution we found can be used to describe both electron and photons density matrix starting from a generic electronic wave function and an initial photon distribution.
Worth noting here is the fact that because of the general initial conditions imposed for solving the Dirac equation, our results open the possibility to investigate multiple aspects of laser-assisted dynamics. Last but not least, the transmission of classical coherence and non-classical features of light absorbed and re-emitted by a free electron.
Regarding this last point, this section also comes as the first step towards the description of the free-electron lasers process in a quantum dynamical fashion that includes the effect of electron's spin. Finally, there are generalizations that are quite straightforward: *in primis* the use of electron Wigner function or electron coherent state to approach a phase space or semi-classical description that still take into account the spin effect; secondly, the inclusion of external fields, such as magnetic or Coulomb fields. The former can be used to describe Landau levels or undulator dynamics, while the latter can be exploited to include atomic potential, indispensable to achieve a faithful model for high harmonic generation.

4.5.1 Evolution operator

The minimal coupling of a single electron with a quantized monochromatic electromagnetic field is described by the following Hamiltonian:

$$\hat{H} = m\,c^2\,\hat{\beta} \,+\, c\,\hat{\boldsymbol{\alpha}}\hat{\mathbf{p}} + \hbar\,\omega\,\hat{a}^\dagger\,\hat{a} \,-\, e\,\hat{\mathbf{A}}(\hat{\mathbf{r}})\,, \tag{4.84}$$

where

$$\hat{\boldsymbol{\alpha}} = \begin{pmatrix} 0 & \boldsymbol{\sigma} \\ \boldsymbol{\sigma} & 0 \end{pmatrix}, \quad \hat{\beta} = \begin{pmatrix} I_2 & 0 \\ 0 & -I_2 \end{pmatrix}, \quad \{\hat{\alpha}_i, \hat{\alpha}_j\} = 2\delta_{ij}, \quad \{\hat{\alpha}_i, \hat{\beta}\} = 0\,,$$

electron vector momentum operator $\hat{\mathbf{p}}$, field annihilation and creation operators $\hat{a}$, $\hat{a}^\dagger$ such that $[\hat{a}\,,\,\hat{a}^\dagger]=1$ and quantized vector potential at the electron position operator $\hat{\mathbf{r}}$ given by

$$\hat{\mathbf{A}}(\hat{\mathbf{r}})=\sqrt{\frac{2\pi c^2\hbar}{\omega V}}\left(\boldsymbol{\varepsilon}\,\mathrm{e}^{i\mathbf{k}\hat{\mathbf{r}}}\,\hat{a}\,+\,\boldsymbol{\varepsilon}^*\,\mathrm{e}^{-i\mathbf{k}\hat{\mathbf{r}}}\,\hat{a}^\dagger\right) \tag{4.85}$$

where $\mathbf{k}$ is the field wave-vector such that $\omega=c\|\mathbf{k}\|$ and, in the Coulomb gauge, $\boldsymbol{\varepsilon}\mathbf{k}=0$.
The Hamiltonian $\hat{H}$ acts on the tensor product $\mathcal{H}=\mathcal{H}_{el}\otimes\mathcal{H}_{ph}$ of the Hilbert space $\mathcal{H}_{el}=L^2(\mathbf{R}^3)\otimes\mathbb{C}^4$ of the relativistic electron and the Fock space $\mathcal{H}_{ph}$ describing the monochromatic photons associated with the electromagnetic field.
Given an initial electron-photon state $|\Psi\rangle$ or a more general mixed state of the form

$$\rho=\sum_\alpha\lambda_\alpha\,|\Psi_\alpha\rangle\langle\Psi_\alpha|\,,\quad\lambda_\alpha\geq 0\,,\;\sum_\alpha\lambda_\alpha=1\,, \tag{4.86}$$

its time evolution is given by

$$\rho\mapsto\rho(t)\equiv\hat{W}_t\,\rho\,\hat{W}_t^\dagger\,,\quad\hat{W}_t\equiv\exp\left(-\frac{i}{\hbar}\,t\,\hat{H}\right)\,. \tag{4.87}$$

From such an expression one can derive any property of the compound electron-photon system associated with suitable observables $\hat{X}$ acting on $\mathcal{H}$, for instance the probability of evolving into another state $|\Phi\rangle$ at time t, $\hat{X}=|\Phi\rangle\langle\Phi|$, by computing quantities of the form

$$\langle\hat{X}\rangle_t\equiv\mathrm{Tr}\Big(\rho(t)\,\hat{X}\Big)\,. \tag{4.88}$$

In what follows we aim at providing a manageable expression for $\hat{W}_t$ that might allow us to inspect properties like the quantumness of the light re-emitted by the electron when its generic initial sates are impinged by light with specific photon properties. The derivation of such an expression for the dynamical unitary map $\hat{W}_t$ will be pursued by successive diagonalizing steps.
The action of the electron-photon unitary operator

$$\hat{V}=\exp\left(-i\mathbf{k}\hat{\mathbf{r}}\otimes\hat{a}^\dagger\,\hat{a}\right) \tag{4.89}$$

is such that

$$\hat{\mathbf{A}}(\hat{\mathbf{r}})\,=\,\sqrt{\frac{2\pi c^2\hbar}{\omega V}}\,\hat{V}\,\left(\boldsymbol{\varepsilon}\,\hat{a}\,+\,\boldsymbol{\varepsilon}^*\,\hat{a}^\dagger\right)\,\hat{V}^\dagger\,,\quad\hat{V}^\dagger\,\hat{\mathbf{p}}\,\hat{V}=\hat{\mathbf{p}}-\hbar\,\mathbf{k}\,\hat{a}^\dagger\,\hat{a}\,. \tag{4.90}$$

Then, by means of the Dirac matrices

$$\hat{\gamma}^0=\hat{\beta}\,,\quad\hat{\boldsymbol{\gamma}}=(\hat{\gamma}^1,\hat{\gamma}^2,\hat{\gamma}^2)=\hat{\gamma}^0\hat{\boldsymbol{\alpha}}\quad\{\hat{\gamma}^\mu\,,\,\hat{\gamma}^\nu\}=2\,g^{\mu\nu}\,\hat{\mathbb{I}}\,, \tag{4.91}$$

where $\hat{g}=[g^{\mu\nu}]$ is the diagonal 4×4 matrix $[1,-1,-1,-1]$, the Hamiltonian can be rewritten as follows

$$\hat{H}=\hat{V}\,\left(c\,\hat{\gamma}^0\left(\hat{\boldsymbol{\gamma}}\hat{\mathbf{p}}+m\,c+\hbar\Big(\gamma^0\,k_0-\mathbf{k}\hat{\boldsymbol{\gamma}}\Big)\hat{a}^\dagger\,\hat{a}-g\,\hat{\boldsymbol{\gamma}}\hat{\mathbf{A}}\right)\right)\,\hat{V}^\dagger\,, \tag{4.92}$$

where we have set

$$g\equiv\sqrt{\frac{2\pi\mathrm{e}^2\hbar}{\omega V}}\,,\quad\hat{\mathbf{A}}\equiv\boldsymbol{\varepsilon}\,\hat{a}\,+\,\boldsymbol{\varepsilon}^*\,\hat{a}^\dagger\,. \tag{4.93}$$

In the following we shall use the slash notation,

$$\not{a}=\hat{\gamma}a\equiv\sum_{\mu=0}^{3}\hat{\gamma}^\mu a_\mu=\hat{\gamma}^0a_0-\hat{\boldsymbol{\gamma}}\mathbf{a}\,, \tag{4.94}$$

where a stands for the 4-dimensional vector $(a^\mu)=(a_0,\mathbf{a})$ so that $(a_\mu)=(a_0,-\mathbf{a})$.
Taking into account that, in the Coulomb gauge, the time-component $\hat{A}^0$ of the potential 4-vector vanishes, we will now concentrate on the Hamiltonian

$$\hat{K}\equiv\,c\,\hat{\gamma}^0\left(\hat{\boldsymbol{\gamma}}\hat{\mathbf{p}}+m\,c+\hbar\not{k}\,\hat{a}^\dagger\,\hat{a}+g\not{\hat{\mathbf{A}}}\right)\,, \tag{4.95}$$

where, with the 4-polarization vector $\varepsilon = (\varepsilon^\mu) = (0, \boldsymbol{\varepsilon})$,

$$\not{k} = \hat{\gamma}^0 \frac{\omega}{c} - \hat{\boldsymbol{\gamma}}\mathbf{k} \,, \quad \not{\mathbf{A}} = \not{\varepsilon}\, \hat{a} \,+\, \not{\varepsilon}^*\, \hat{a}^\dagger \,, \quad \not{\varepsilon} = -\hat{\boldsymbol{\gamma}}\boldsymbol{\varepsilon} \,. \tag{4.96}$$

By expanding along pseudo-eigenprojectors $|\mathbf{p}\rangle\langle\mathbf{p}|$ of $\hat{\mathbf{p}}$, $\hat{\mathbf{p}}|\mathbf{p}\rangle = \mathbf{p}|\mathbf{p}\rangle$, one rewrites

$$\hat{K} = \int_{\mathbf{R}^3} \mathrm{d}\mathbf{p}\, |\mathbf{p}\rangle\langle\mathbf{p}| \otimes \hat{K}(\mathbf{p}) \,, \quad \hat{K}(\mathbf{p}) \equiv c\hat{\gamma}^0 \, \left(\hat{\boldsymbol{\gamma}}\mathbf{p} + m\, c + \hbar \not{k}\, \hat{a}^\dagger\, \hat{a} + g\, \not{\mathbf{A}}\right) \,, \tag{4.97}$$

where the momentum operator $\hat{\mathbf{p}}$ has become a vector $\mathbf{p} \in \mathbb{R}^3$ and the Hamiltonians $\hat{K}(\mathbf{p})$ are now operators on $\mathbb{C}^4 \otimes \mathcal{H}_{ph}$.
Using that $\hat{\gamma}^0\hat{\gamma}^0 = \hat{\mathbb{I}}$, the eigenvalue equation for such $\hat{K}(\mathbf{p})$,

$$\hat{K}(\mathbf{p})|E(\mathbf{p})\rangle \;=\; E(\mathbf{p})\, |E(\mathbf{p})\rangle \,, \tag{4.98}$$

can be recast as

$$\Big(\not{p} \;-\; m\, c \;-\hbar \not{k}\, \hat{a}^\dagger\, \hat{a} - g\, \not{\mathbf{A}}\Big)\, |E(\mathbf{p})\rangle = 0 \,, \tag{4.99}$$

where

$$\not{p} = \hat{\gamma}^0\, E(\mathbf{p}) \;-\; \hat{\boldsymbol{\gamma}}\mathbf{p} \,. \tag{4.100}$$

Once (4.99) has been solved, the dynamical map $\hat{W}_t$ in (4.87) will be of the form

$$\hat{W}_t = \int_{\mathbb{R}^3} \mathrm{d}\mathbf{p} \sum_{E(\mathbf{p})} \mathrm{e}^{-i\, t\, E(\mathbf{p})}\, \hat{V}\, |\mathbf{p}\rangle\langle\mathbf{p}| \otimes |E(\mathbf{p})\rangle\langle E(\mathbf{p})|\, \hat{V}^\dagger \,. \tag{4.101}$$

In order to solve (4.99), one first introduces the following unitary operator on $\mathbb{C}^4 \otimes \mathcal{H}_{ph}$,

$$\hat{U}(\mathbf{p}) = \hat{\mathbb{I}} + \frac{g}{2pk}\, \not{k}\not{\mathbf{A}} \,, \quad pk = E(\mathbf{p})\frac{\omega}{c} - \mathbf{p}\mathbf{k} \,. \tag{4.102}$$

The unitarity of $\hat{U}(\mathbf{p})$ follows from the fact that, in the Coulomb gauge,

$$\not{k}\not{\varepsilon} = -\frac{1}{2}\sum_{i,j=1}^{3} k^i \varepsilon^j \left[\hat{\gamma}^i \,,\, \hat{\gamma}^j\right] \Longrightarrow \Big(\not{k}\not{\varepsilon}\Big)^\dagger \;=\; -\not{k}\, \not{\varepsilon}^* \,, \tag{4.103}$$

which implies

$$\hat{U}^\dagger(\mathbf{p}) = \hat{U}^{-1}(\mathbf{p}) = \hat{\mathbb{I}} \;-\; \frac{g}{2pk}\, \not{k}\not{\mathbf{A}} \,. \tag{4.104}$$

One explicitly finds

$$\hat{U}^\dagger(\mathbf{p})\Big(\not{p} \;-\; m\, c \;-\hbar \not{k}\, \hat{a}^\dagger\, \hat{a} - g\, \not{\mathbf{A}}\Big)\hat{U}(\mathbf{p}) = \not{p} \;-\; m\, c \;-\hbar \not{k}\, \hat{a}^\dagger\, \hat{a} - g\, \not{\mathbf{A}} - \frac{g}{2pk}\not{k}\not{\mathbf{A}}\not{p} \tag{4.105}$$

$$+\frac{g^2}{2pk}\not{k}\not{\mathbf{A}}^2 + \frac{g}{2pk}\not{p}\not{k}\not{\mathbf{A}} + \frac{g^2}{2pk}\not{k}\not{\mathbf{A}}^2 - \frac{g^2}{(2pk)^2}\not{k}\not{\mathbf{A}}\not{p}\not{k}\not{\mathbf{A}} \,. \tag{4.106}$$

Then using that

$$\not{k}^2 = 0 \,, \quad \not{p}\not{k} = 2pk - \not{k}\not{p} \,, \quad \text{and} \quad \not{k}\, \not{\mathbf{A}} \;=\; -\not{k}\not{\mathbf{A}} \quad \text{in the Coulomb gauge} \,, \tag{4.107}$$

one finds

$$\not{k}\not{\mathbf{A}}\not{p}\not{k}\not{\mathbf{A}} = 2pk\, \not{k}\not{\mathbf{A}}^2 \,, \tag{4.108}$$

so that the electronic spinorial factor $\not{k}$ can be brought to multiply an operator $\hat{K}(\mathbf{p})$ that acts solely on $\mathcal{H}_{ph}$:

$$\not{p} \;-\; m\, c \;-\hbar \not{k}\, \hat{a}^\dagger\, \hat{a} - g\, \not{\mathbf{A}} = \hat{U}(\mathbf{p})\Big(\not{p} - mc \;-\; \not{k}\, \hat{K}_{ph}(\mathbf{p})\Big)\hat{U}^\dagger(\mathbf{p}) \,, \tag{4.109}$$

$$\hat{K}_{ph}(\mathbf{p}) \equiv \Gamma \hat{a}^\dagger \hat{a} + \left(\alpha \hat{a} + \alpha^* \hat{a}^\dagger\right) + \left(\mu \hat{a}^2 + \mu^* (\hat{a}^\dagger)^2\right) + \eta_1, \tag{4.110}$$

$$\Gamma = \left(\hbar - g^2 \frac{\varepsilon^* \varepsilon}{pk}\right), \quad \alpha = g\frac{\varepsilon p}{pk}, \quad \mu = -\frac{g^2}{2pk}\varepsilon^2, \quad \eta_1 = -g^2 \frac{\not{\varepsilon}\not{\varepsilon}^*}{2pk} \tag{4.111}$$

and can be diagonalized by means of squeezing and displacement operators,

$$\hat{S}(\Theta(\mathbf{p})) \equiv \exp\left(\Theta(\mathbf{p})\,\hat{a}^2 - \Theta^*(\mathbf{p})\,(\hat{a}^\dagger)^2\right) , \tag{4.112}$$

$$\hat{D}(\sigma(\mathbf{p})) \equiv \exp\left(\sigma(\mathbf{p})\hat{a}^\dagger - \sigma^*(\mathbf{p})\hat{a}\right) , \tag{4.113}$$

such that

$$\hat{K}_{ph}(\mathbf{p}) = \hat{S}(\Theta(\mathbf{p}))\,\hat{D}(\sigma(\mathbf{p}))\left(\hbar\,\Omega(\mathbf{p})\,\hat{a}^\dagger\,\hat{a} \,+\, \eta(\mathbf{p})\right)\hat{D}^\dagger(\sigma(\mathbf{p}))\,S^\dagger(\Theta(\mathbf{p}))\,. \tag{4.114}$$

where the energies $\hbar\,\Omega(\mathbf{p})$ and the complex parameters $\Theta(\mathbf{p})$ and $\sigma(\mathbf{p})$ depend on $\mathbf{p}$.
The expression for $\Theta(\mathbf{p})$ and $\sigma(\mathbf{p})$ in the case of linear polarization, *i.e.* $\varepsilon^* = \varepsilon$ and referring the coefficients defined in Eq. 4.111

$$\tanh\left[2\Theta(\mathbf{p})\right] = \frac{2\mu}{\Gamma} = \frac{g^2}{g^2 + \hbar p k} \tag{4.115}$$

$$\sigma(\mathbf{p}) = -\frac{\alpha(\cosh\Theta(\mathbf{p}) - \sinh\Theta(\mathbf{p}))}{\sqrt{\Gamma^2 + (2\mu)^2}} \tag{4.116}$$

where we have used the fact that $\varepsilon^*\varepsilon = \varepsilon^2 = -1$. In the case of circular polarization, instead, $\varepsilon^2 = 0$ implies $\mu = 0$ and there are no quadratic terms in Eq. (4.110), except for the first one. In this situation the squeezing operator is not necessary.
Finally, the energies are determined by

$$\Omega(\mathbf{p}) = \frac{1}{\hbar}\sqrt{\Gamma^2 + (2\mu)^2} = \frac{1}{\hbar}\Gamma\sqrt{1 + \tanh\left[2\Theta(\mathbf{p})\right]^2} = \frac{1}{\hbar p k}\sqrt{(\hbar p k + g^2)^2 + g^4}. \tag{4.117}$$

Observe that, by means of the photon number eigenstates,

$$\hat{a}\,|0\rangle = 0\,, \quad |n\rangle \equiv \frac{(\hat{a}^\dagger)^n}{\sqrt{n!}}|0\rangle \quad \text{such that} \quad \hat{a}^\dagger\,\hat{a}\,|n\rangle = \,n\,|n\rangle\,, \tag{4.118}$$

one can rewrite

$$\hat{K}_{ph}(\mathbf{p}) = \sum_{n=0}^{+\infty}\Big(\hbar\Omega(\mathbf{p})\,n \,+\, \eta(\mathbf{p})\Big)\hat{D}(\sigma(\mathbf{p}))\,\hat{S}(\Theta(\mathbf{p}))\,|n\rangle\langle n|\,\hat{S}^\dagger(\Theta(\mathbf{p}))\,\hat{D}^\dagger(\sigma(\mathbf{p}))\,. \tag{4.119}$$

Then, (4.109) can be recast as

$$\not{p} - mc - \hbar\not{k}\hat{a}^\dagger\,\hat{a} - g\not{A} = \sum_{n=0}^{+\infty}\hat{T}_1(\mathbf{p})\Big[\not{p} \,-\, mc \,-\, \not{k}\Big(\hbar\,\Omega(\mathbf{p})\,n + \eta(\mathbf{p})\Big) \otimes |n\rangle\langle n|\Big]\hat{T}_1^\dagger(\mathbf{p})$$

where the operators

$$\hat{K}_{sp}(\mathbf{p}) \equiv \not{p} \,-\, mc \,-\, \not{k}\left(\hbar\,\Omega(\mathbf{p})\,n \,+\, \eta(\mathbf{p})\right) \tag{4.120}$$

is a 4×4 matrix acting on the spinorial electronic Hilbert space $\mathbb{C}^4$ and

$$\hat{T}_1(\mathbf{p}) = \hat{U}(\mathbf{p})\,\hat{S}(\Theta(\mathbf{p}))\,\hat{D}(\sigma(\mathbf{p})). \tag{4.121}$$

Once the 4-vectors $|\chi_\alpha(n,\mathbf{p})\rangle$, $\alpha = 1,2,3,4$, satisfying the eigenvalue equation

$$\hat{K}_{sp}(\mathbf{p})\,|\chi_\alpha(n,\mathbf{p})\rangle = 0\,, \tag{4.122}$$

have been found, the sought after eigenvectors $|E(\mathbf{p})\rangle$ in (4.99) are given by

$$|E_{n,\alpha}(\mathbf{p})\rangle = \hat{U}(\mathbf{p})\,\hat{S}(\Theta(\mathbf{p}))\,\hat{D}(\sigma(\mathbf{p}))\,|n\rangle \otimes |\chi_\alpha(n,\mathbf{p})\rangle\,, \tag{4.123}$$

and the dynamical operator $\hat{W}_t$ in (4.101) finally reads

$$\hat{W}_t = \textstyle\int_{\mathbb{R}^3}\mathrm{d}\mathbf{p}\,\sum_{n=0}^{+\infty}\sum_{\alpha=1}^{4}\mathrm{e}^{-i\,t\,E_{n,\alpha}(\mathbf{p})}\,\hat{T}(\mathbf{p})\left(|\mathbf{p}\rangle\langle\mathbf{p}| \otimes |n\rangle\langle n| \otimes |\chi_\alpha(n,\mathbf{p})\rangle\langle\chi_\alpha(n,\mathbf{p})|\right)\hat{T}^\dagger(\mathbf{p})\,, \tag{4.124}$$

$$\hat{T}(\mathbf{p}) \equiv \hat{V}\,\hat{U}(\mathbf{p})\,\hat{S}(\Theta(\mathbf{p}))\,\hat{D}(\sigma(\mathbf{p}))\,. \tag{4.125}$$

It is possible to prove some fundamental properties of $\hat{W}_t$, namely

$$\hat{W}_0 = \hat{\mathbb{I}} \qquad \hat{W}_t^\dagger \hat{W}_t = \hat{\mathbb{I}} \tag{4.126}$$

confirming that such operator is unitary and that the solutions satisfies the completeness relation. The dispersion of the global system and the eigenvalues in 4.125 can be derived from the spinorial equation 4.122, applying $\hat{K}_{sp}(\mathbf{p})^\dagger$ to the left. The resulting equation is cubic in $E_{n,\alpha}$ and can be solved analytically or numerically.
There are some comments that can be pointed out about the four operators contained in $\hat{T}(\mathbf{p})$ and used to write the time-evolution operator. Operator $\hat{V}$ is exploited to remove the dependence on electron variables and acts as a shift in the momentum, proportional to the momentum of the photon state. Operator $\hat{U}(\mathbf{p})$ has been characterized in literature as the transformation from the non-interacting to interacting representation of the Dirac equation, or, equivalently, to the transformation that defines a new set of gamma function [133]. This is, indeed, also the transformation from the Dirac to the Majorana representation [135]. There is however another interpretation that we propose for the ambivalent action on electronic and photonic degrees of freedom. In the former case, $\hat{U}(\mathbf{p})$ act as a Lorentz transformation. This is confirmed by the fact that it is a function of $\gamma^\mu\gamma^\nu$, a product that can be used as the generator for the $(1/2, 0) \oplus (0, 1/2)$ representation of the Lorentz group. In the photonic case, instead, $\hat{U}(\mathbf{p})$ is a displacement operator, and can be written as the exponential of a Grassman number. The presence of such operator is responsible for the non-minimal coupling that Pauli equation and Dirac equation in the Newton-Wigner representation display. This also suggests a way to generalize the decoupling from spin in the interaction with the electromagnetic field, independently from the value of the spin.
Because of the coupling with both spin and charge, the interaction between an electromagnetic field and a single electron is always non-classical. As we have shown in the diagonalization, the interaction Hamiltonian has a group structure, namely $SU(1,1) \rtimes H$, that does not preserve coherent states. In particular, this kind of Hamiltonian modifies the statistical properties of Glauber states, possibly introducing a non-poissonian behavior [136]. For this reason, the eigenstate for the photonic part are written in terms of squeezed coherent state, obtained from $\hat{S}(\Theta(\mathbf{p}))\,\hat{D}(\sigma(\mathbf{p}))$.

4.6 Summary

In this chapter, we introduced a reconstruction algorithm based on the off-clicks distribution of a Geiger-like detector for photons. We showed that this technique can be extended to a significantly higher number of photons with respect to the one proposed in literature and applied to the case of SASE and seeded FELs. We determined the possible quantum states of light that could be associated with the light produced in these two different schemes and used it as the input distribution for the algorithm. The reconstructions were all characterized by a high fidelity.
In the second part, we derived some useful results regarding the determination of light and electron properties in a simple system: a single electron in a quantized electromagnetic field. It is shown that the electron behaves in a non-classical manner when interacting with photons because of the spin degree of freedom. The formalism developed can be applied to any initial condition, including quantum light interacting with an electron wavefunction.

4.7 List of publications

- Benatti, F., Olivares, S., **Perosa, G.**, Bajoni, D., Di Mitri, S., Floreanini, R., Ratti, L. and Parmigiani, F., Quantum state features of the FEL radiation from the occupation number statistics. *Optics Express* **29**, 40374–40396 (2021).

Chapter 5

Conclusions and perspectives

The aim of this thesis, organized in an introduction and three chapters, is to highlight the role of the electron dynamics on the coherence of short wavelength high-gain free-electron lasers. In particular, we focused our attention on some of the most relevant collective phenomena affecting the electron dynamics and consequently the FEL light coherence. Recent experiments have shown that seeded FELs display a high degree of longitudinal coherence, but are still affected by the electron bunch dynamics. Furthermore, the FEL seeding process with an external laser is clearly determining a higher degree of longitudinal coherence with respect to the conventional SASE FELs. Nonetheless, even for laser seeded FELs, spurious harmonic content in the beam, as detailed in this work, are at the origin of longitudinal coherence deterioration. The effect of spurious harmonic content can be mitigated once a comprehensive description of the electron dynamics is achieved. This becomes even more evident when the statistical behavior of the emitters has to be taken into account. Conversely, the measure of the photon beam coherence is suitable for the characterization of the electron bunch.
The second chapter is dedicated to the measurement of transverse and longitudinal coherence. Measurements of phase correlation show that transverse coherence is developed differently in SASE and seeded FELs. While the former is dominated by the thermal behavior of accelerated electrons, the seed laser imprint dominates the features of the latter. However, microbunching instability significantly affects the seed FEL longitudinal coherence as measured by second-order correlation function.
In fact, microbunching instability (MBI) has proven to be one of the most relevant showstoppers to improve FEL performance, including FEL brightness and coherence. This issue is discussed in the third chapter.
MBI was described theoretically and characterized experimentally. By measuring the bunch energy spread at the exit of FERMI linac, we benchmarked the model for longitudinal phase space dynamics to which I gave a major contribution. This formalism includes also intrabeam scattering (IBS), which is an unexplored mechanism in electron linear accelerators so far. In particular, including IBS into the MBI models brings a good agreement between the measured and calculated energy spread.
As a direct evidence of MBI, 2-D Fourier analysis of longitudinal phase space provided new information about MBI and energy modulations after compression. This technique has been used for both shot-noise-based MBI and for the artificially injected one. MBI spectral gain has also been measured with an infrared spectrometer and characterized as a function of the machine parameters such as induced energy spread and compression. With this second diagnostic station, positioned after the spreader line of FERMI FEL-2, we were able to determine the impact of such long dispersive section.
We also demonstrate that MBI is not localized in a portion of the electron bunch, but uniformly distributed along the current profile.
We showed that there is a clear correlation between the MBI content and FEL performance by comparing the reduction of spurious harmonic content in the emitted light and the reduction of the signal on the spectrometer. Finally, the performances of seeded FELs in the HGHG and EEHG configurations in presence or absence of MBI have been characterized. In this regards, we showed that spreader optics is an additional knob to control and reduce the MBI impact.
The comparison between 2-D Fourier analysis, spectrometer data and the FEL spectral purity, with the same beam condition, could become a standard procedure to gain more information about this plasma-like dynamics. This in turn, will become helpful to further develop the theoretical apparatus for the description of MBI and related phenomena.

In perspective, we are planning to use the measurement of second-order correlation function to associate the statistical behavior of FEL sidebands with the modulations in the electron bunch. This allows to promote the measurement of FEL spectral content into a novel diagnostic for microbunching instability.
The last chapter dealt with the characterization of FEL coherence from a quantum-mechanical point of view. In our pioneering work, we proposed to shift the attention towards the poissonianity of a source, instead of the degrees of coherence, promoting it as an alternative method to investigate the coherence of seeded FELs longitudinal and transverse. To do so, we tested a reconstruction algorithm by feeding it with simulated photon number distributions that represent possible FEL classical states. This method has proven to be very efficient in retrieving the deviation from Poisson distribution of highly populated photon states.
All this considered, we are planning to exploit such algorithm also for experimental no-click frequencies to measure poissonianity of light sources, first in the visible and then in the XUV regime.
To include the impact of electron on quantum coherence, a fully quantum picture is needed. The fundamental building block to achieve a QED description of emission processes stimulated by an external coherent source is the interaction of a Dirac fermion, *i.e.* an electron, with a quantized electromagnetic field. We therefore derived a new solution to this problem, interpreting all the components of such expression.
Interestingly, the formalism proposed can be used to calculate the evolution of both light and electron properties, such as the second order correlation function. With our apparatus it is possible to determine if and how the free-electron wave function is affected by these statistics of the interacting photon and how this statistics is modified by the interaction. Calculations of this type will become the first theoretical description of how quantum coherence is transferred from photons to electron and vice versa.
We are already planning the next steps by including a many-body treatment for electrons and non-monochromatic quantized electromagnetic field. The former is necessary to describe processes in which more than one electron is involved, while the latter allows us to include any form of external fields (classical or not). This result is versatile enough to be adapted to describe HHG and inverse Compton scattering.

Appendix A

FERMI layout

The FERMI [137] is an international user linac-driven FEL facility delivering short pulses (in the range between 100 fs and 10 fs) close to the Fourier limit with tunable wavelength and polarization in the range from 100 to 4 nm.

FERMI Linac

FERMI linac is shown in Figure A.1.
FERMI photo-injector delivers 10 ps long pulse with a bunch charge in the range between 500 and 700

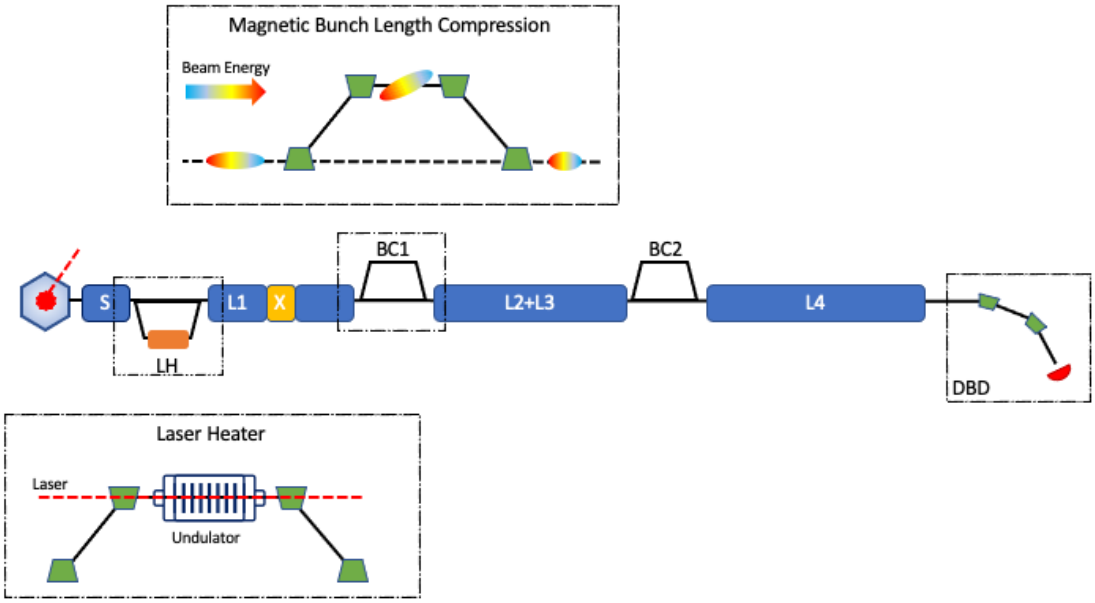

Figure A.1: Overview of FERMI linac (not to scale). The insets show the geometry of Laser Heater (lower) and Bunch Length Compressor (upper). The Diagnostic Beam Dump is also indicated in the scheme.

pC (standard operation) and a repetition rate of 50 Hz with a rms normalized transverse emittance of 1.2 mm-mrad at 100 MeV. A laser system provides an UV laser pulse for the electron extraction and the laser heater (LH) [62].
The laser heater is a device installed to heat the beam, increasing by a fixed amount the uncorrelated energy spread of the electron beam. The heating is provided by the interaction of the laser with the electron bunch in an undulator, placed in the middle of a four dipoles chicane. The parameters are provided in Table A.1.
The prescription of artificially increase the energy spread is motivated by the high sensitivity of microbunching instability to such parameter.
After reaching 100 MeV with two S-band rf sections, the beam is injected in the main linac. The linac is

Table A.1: FERMI Laser Heater Parameters

Parameters	Values
Undulator period	40 mm
Number of periods	12
Undulator parameter	0.8-1.17
Laser wavelength	783 nm
Laser pulse duration	8-15 ps
Laser energy	$< 160\,\mu$J
Laser transverse size	130-220 μJ
Horizontal offset in the chicane	30 mm
Chicane bending angle	3.5 deg

composed of four accelerating sections (L1 to L4) and two bunch compressors (BC1 and BC2) before the transfer section which transports the beam to the two FEL lines, known as a "spreader". The final energy of the beam ranges from 0.9 to 1.35 GeV. The off-crest acceleration before compression, the non-linearities of the correlated momentum distribution along the bunch and the longitudinal wakefields are compensated by an X-band rf structure placed in L1.
Bunch compressors are designed to increase the beam peak current. They are four-dipole chicanes that exploit the linear chirp introduced by off-crest acceleration, before the first bending magnet, to decrease the path travelled by lower energy particles and increase it for higher energy particles. This strategy shorten the bunch length and, since the charge is conserved, increase the overall current. In typical operations only BC1 is employed, in order to prevent the enhancement of microbunching instability. The current after compression is of the order of 500 A and the bunch duration is less than 1 ps.

Diagnostic Beam Dump

Before the two branches of the transfer line, FERMI possess also a Diagnostic Beam Dump (DBD), positioned at the end of the linac. A couple of bending magnets deflect the beam along this beamline in which the longitudinal phase space of the beam is characterized with the help of a vertical RF deflector (VRFD) and a horizontal spectrometer magnet [95]. After the dipoles, the beam is intercepted by a screen, whose horizontal and vertical physical axis can be calibrated to be proportional, respectively, to the energy and arrival time of the particles. As a matter of fact, the presence of a dispersive region introduce a correlation between energy and position, while the use of the deflecting cavity, correlates time and position. For this reason, images of the bunches at the screen can be used to retrieve the bunch duration, current profile, the energy spread and energy chirps.

Free Electron Lasers

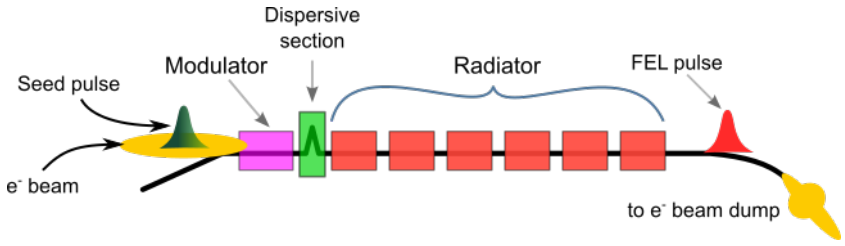

Figure A.2: FERMI FEL1. Image from [138]

Each branch of the transfer line is assigned to one of the two externally seeded FELs, called FEL-1 (in Fig. A.2) and FEL-2 (in Fig. A.3). Both switchyard are composed of four dipoles and the first two are common.
FEL-1 is a single-stage high gain harmonic generation FEL which covers the wavelength range 100-20 nm, while FEL-2 is a double-stage high gain harmonic generation FEL, covering the range the range 20-4 nm.

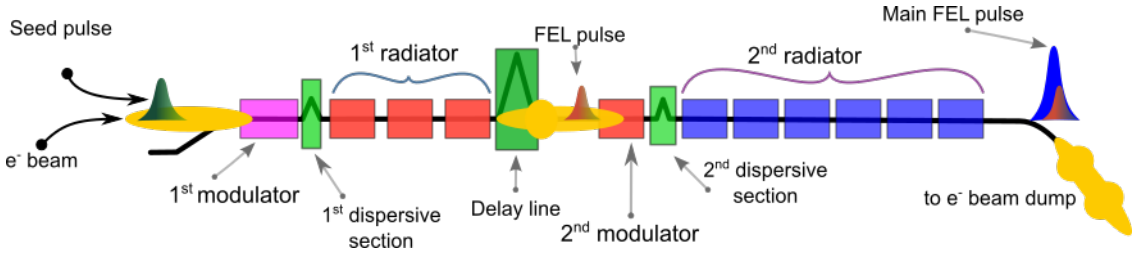

Figure A.3: FERMI FEL2. Image from [138]

They both rely on a conventional, high peak-power pulsed laser as external seed. The energy modulation coming from the laser-electron interaction in a first undulator section, called the modulator, is converted into density modulation by crossing dispersive section. In this process, modulation occurs at the fundamental seed wavelength, as well as at its higher harmonics. The following radiators are then tuned to resonate at one of these harmonics so that high intensity FEL emission is radiated.
In the case of FEL-2 the process is repeated twice: in a second modulator, light produced by the first stage is used as an external seed to further increase the harmonic jump. The FEL process takes place in a second radiator section. A magnetic delay line between the two stages is inserted in order to seed, in the second stage, a portion of the electron beam that has not been spoiled by the previous emission process.

Appendix B

P-function: coherent, thermal and number states

Coherent states form a continuous non-orthogonal family,

$$\langle\alpha|\beta\rangle = \mathrm{e}^{-\frac{1}{2}(|\alpha|^2+|\beta|^2-2\alpha^*\beta)} , \tag{B.1}$$

which is however over-complete in the sense that the corresponding projectors integrate to the identity operator

$$\int_{\mathbb{C}} \frac{\mathrm{d}^2\alpha}{\pi}\ |\alpha\rangle\,\langle\alpha| = \mathbb{I}\,. \tag{B.2}$$

Coherent states are obtained by displacing the vacuum $|0\rangle$,

$$D(\alpha)\,|0\rangle = |\alpha\rangle\ , \tag{B.3}$$

by means of the displacement operators

$$D(\alpha) = \mathrm{e}^{\alpha\,a^\dagger\,-\,\alpha^*\,a} = \mathrm{e}^{-|\alpha|^2/2}\,\mathrm{e}^{\alpha\,a^\dagger}\,\mathrm{e}^{-\alpha^*\,a}\ , \tag{B.4}$$

which are such that

$$D(\beta)\,D(\alpha) = \mathrm{e}^{(\beta^*\alpha-\beta\alpha^*)/2}\,D(\alpha+\beta)\ , \quad D^\dagger(\beta)\,D(\alpha)\,D(\beta) = \mathrm{e}^{\beta^*\alpha-\beta\alpha^*}\,D(\alpha)\ . \tag{B.5}$$

whence $D^\dagger(\alpha)\,a\,D(\alpha) = a+\alpha$.
Let ρ be the density matrix of a monochromatic light beam; its Glauber-Sudarshan representation reads as a continuous linear combination of coherent-state projectors

$$\rho = \int_{\mathbb{C}} \mathrm{d}^2\alpha\,\mathcal{P}_\rho(\alpha)\,|\alpha\rangle\langle\alpha|\ .$$

Using the scalar product (B.1), with $\alpha = x+iy$ and $\beta = u+iv$, one obtains

$$\begin{aligned}\mathrm{e}^{|\beta|^2}\,\langle-\beta|\rho|\beta\rangle &= \int_{\mathbb{C}} \mathrm{d}^2\alpha\,\mathcal{P}_\rho(\alpha)\,\mathrm{e}^{-|\alpha|^2-\alpha\beta^*+\alpha^*\beta} \\ &= \int_{\mathbb{R}^2} \mathrm{d}x\mathrm{d}y\,\mathcal{P}_\rho(x+iy)\,\mathrm{e}^{-x^2-y^2}\,\mathrm{e}^{2i(xv-yu)}\ ,\end{aligned} \tag{B.6}$$

whence, by anti-Fourier transformation,

$$\int_{\mathbb{R}^2} \frac{\mathrm{d}(2u)\mathrm{d}(2v)}{4\pi^2}\,\mathrm{e}^{u^2+v^2}\,\langle-u-iv|\rho|u+iv\rangle\,\mathrm{e}^{2i(xv-yu)} = \mathrm{e}^{-x^2-y^2}\,\mathcal{P}_\rho(x+iy)\ . \tag{B.7}$$

Then, the Glauber-Sudarshan P-function $\mathcal{P}_\rho(\alpha)$ can be expressed by means of the matrix elements $\langle-\beta|\rho|\beta\rangle$:

$$\mathcal{P}_\rho(\alpha) = \frac{\mathrm{e}^{|\alpha|^2}}{\pi^2}\int_{\mathbb{C}} \mathrm{d}^2\beta\,\mathrm{e}^{|\beta|^2}\,\mathrm{e}^{\alpha\beta^*-\alpha^*\beta}\,\langle-\beta|\rho|\beta\rangle\ , \tag{B.8}$$

where $|\pm\beta\rangle$ are coherent states.
If ρ is itself a coherent state $\rho_\gamma = |\gamma\rangle\langle\gamma|$, the scalar product (B.1) yields

$$\langle -\beta|\rho_\gamma|\beta\rangle = \mathrm{e}^{-|\beta|^2-|\gamma|^2-\gamma\beta^*+\gamma^*\beta} \,. \tag{B.9}$$

Using (B.8) and the fact that, with $\alpha = x + iy$ and $\beta = u + iv$,

$$\frac{1}{\pi^2}\int_{\mathbb{C}} \mathrm{d}^2\beta\, \mathrm{e}^{\alpha\beta^*-\alpha^*\beta} = \int_{-\infty}^{+\infty}\int_{-\infty}^{+\infty} \frac{\mathrm{d}x}{\pi}\frac{\mathrm{d}y}{\pi}\mathrm{e}^{2i(yu-xv)} = \delta(x)\delta(y) = \delta^2(\alpha)\,, \tag{B.10}$$

one then obtains

$$\mathcal{P}_{\rho_\gamma}(\alpha) = \frac{\mathrm{e}^{|\alpha|^2-|\gamma|^2}}{\pi^2}\int_{\mathbb{C}^2} \mathrm{d}^2\beta\, \mathrm{e}^{-(\gamma-\alpha)\beta^*+(\gamma^*-\alpha^*)\beta} = \delta^2(\alpha-\gamma)\,. \tag{B.11}$$

For thermal states as in (4.28), by Gaussian integration one obtains

$$\langle -\beta|\rho_T|\beta\rangle = \frac{\mathrm{e}^{-|\beta|^2\frac{1+2n_T}{1+n_T}}}{1+n_T} \Longrightarrow \mathcal{P}_T(\alpha) = \frac{1}{\pi}\frac{\mathrm{e}^{-\frac{|\alpha|^2}{n_T}}}{n_T}\,. \tag{B.12}$$

On the other hand, when $\rho = |n\rangle\langle n|$, one computes

$$\langle -\beta|\rho|\beta\rangle = \frac{\mathrm{e}^{-|\beta|^2}}{\pi^2}(-)^n\frac{|\beta|^2}{n!}\,, \tag{B.13}$$

whence, using (B.10), the P-function becomes a highly singular distribution:

$$\mathcal{P}_n(\alpha) = \frac{\mathrm{e}^{|\alpha|^2}}{\pi^2}\int_{\mathbb{C}} \mathrm{d}^2\beta\,(-)^n\frac{|\beta|^2}{n!}\,\mathrm{e}^{\alpha\beta^*-\alpha^*\beta} = \frac{\mathrm{e}^{|\alpha|^2}}{n!}\frac{\partial^{2n}}{\partial_\alpha^n\partial_{\alpha^*}^n}\delta^2(\alpha)\,. \tag{B.14}$$

Appendix C

Geiger-like detectors

When considering the detectors that should measure no-click probabilities, several requirements need to be satisfied. The detector should have fast response ($<$ 1 ns) and a relatively small dead time (ideally $< 100\,ns$) to accommodate for the laser dynamics, especially in the case of FELs with high repetition rates. The quantum efficiency should be high (> 10). One of the most employed single photon detectors are photomultiplier tubes [139]. The figures of merit for photomultipliers are close to those specified above, even if response times are often larger than 1 ns and dead times in the range between 100 ns and 1 μs. One disadvantage of photomultiplier tubes is the need to bias the devices at voltages of the order of 1 kV, making gated operation extremely difficult.
Recent years have seen the development of monolithically integrated CMOS detectors. Monolithic integration of the photosensitive area with the readout electronics offers unprecedented accuracy in the processing of the detected signal and engineering freedom on the sensor characteristics in term of size and electronic response. Fully depleted p-n junctions have been used for X-ray detection and have sensitivities that can reach the single photon level [140, 141]. Different materials can be employed for the sensor area via wafer bonding [142].
Monolithic CMOS detectors can operate in Geiger mode in the case of CMOS single photon avalanche photodiodes (SPADs) [143]. CMOS SPADS have very fast response times (generally $<$ 100 ps) with short dead times (of the order of some tens of ns) and can be operated at low voltage of the order of 10 V. Furthermore their integration can ensure that arrays of photon counting pixels can be easily integrated on chip to the side of the electronic circuits used for counting [144]. Such pixels can be as small as 10 μm in size, giving the possibility of engineering arrays comprising tens or hundreds of single photon counting pixels within the FEL spot diameter. The counts from such an array can then be summed by the on-chip electronics (in a configuration similar to silicon photomultipliers [145]) and pixels can be selectively turned off thus directly controlling the detection efficiency.

Total list of pubblications

- Brynes, A. D., Akkermans, I., Allaria, E., Badano, L., Brussaard, S., De Ninno, G., Gauthier, D., Gaio, G., Gianeesi, L., Mirian, N. S., Penco, G., **Perosa, G.**, Ribic, P. R., Setija, I., Spampinati, S., Spezzani, C., Trovó, M., Veronese, M., Williams, P.H., Wolski, A., Di Mitri, S., Characterisation of microbunching instability with 2D Fourier analysis. *Scientific Reports* **10**, 1–12 (2020).

- Brynes, A. D., Akkermans, I., Allaria, E., Badano, L., Brussaard, Danailov, M., Demidovich, A., De Ninno, G., Mirian, N. S., Penco, G., **Perosa, G.**, Ribic, P. R., Roussel, E., Setija, I., Smorenburg, P., Spampinati, S., Spezzani, C., Trovó, M., Williams, P. H., Wolski, A. and Di Mitri, S., Microbunching instability characterization via temporally modulated laser pulses. *Phys. Rev. Accel. Beams* **23**, 104401. (2020).

- Di Mitri, S., **Perosa, G.**, Brynes, A. D., Seija, I., Spampinati, S., Williams, P. H., Wolski, A., Allaria, E., Brussaard, S., Penco, G., Ribic, P. R. and Trovó, M., Experimental evidence of intrabeam scattering in a free-electron laser driver. *New Journal of Physics* **22**, 083053 (Aug. 2020).

- Di Mitri, S. & **Perosa, G.**, Electron Beam Transport in Plasma-Accelerator-Driven Free-Electron Lasers in the Presence of Coherent Synchrotron Radiation and Microbunching Instability. *Physics* **2**, 521–530. ISSN: 2624-8174. (2020).

- **Perosa, G.**, Allaria, E., Badano, L., Bruchon, N., Cinquegrana, P., Danailov, M. B., Demodovich, A., De Ninno, G., Mirian, N. S., Penco, G., Ribic, P. R., Roussel, E., Sigalotti, P., Spampinati, S., Veronese, M., Trovó, M. and Di Mitri, S., Linear optics control of sideband instability for improved free-electron laser spectral brightness. *Phys. Rev. Accel. Beams* **23**, 110703. (11 Nov. 2020).

- Penco, G., **Perosa, G.**, Allaria, E., Di Mitri, S., Ferrari, E., Giannessi, L., Spampinati, S., Spezzani, C. and Veronese, M., Enhanced seeded free electron laser performance with a "cold" electron beam. *Phys. Rev. Accel. Beams* **23**, 120704. (12 Dec. 2020).

- **Perosa, G.** & Di Mitri, S. Matrix model for collective phenomena in electron beam's longitudinal phase space. *Scientific reports* **11**, 1–10 (2021).

- Di Mitri, S., Cornacchia, M., Diviacco, B., **Perosa, G.**, Sottocorona, F. and Spampinati, S., Bridging the gap of storage ring light sources and linac-driven free-electron lasers, *Phys. Rev. Accel. Beams* **24**, 060702. (28 June 2021)

- Mirian, N. S., **Perosa, G.**, Hemsing, E., Allaria, E., Badano, L., Cinquegrana, P., Danailov, M. B., De Ninno, G., Giannesi, L., Penco, G., Spampinati, S., Spezzani, C., Roussel, E., Ribic, P. R., Trovó, M., Veronese, M. and Di Mitri S., Characterization of soft x-ray echo-enabled harmonic generation free-electron laser pulses in the presence of incoherent electron beam energy modulations. *Phys. Rev. Accel. Beams* **24**, 080702. (8 Aug. 2021).

- Benatti, F., Olivares, S., **Perosa, G.**, Bajoni, D., Di Mitri, S., Floreanini, R., Ratti, L. and Parmigiani, F., Quantum state features of the FEL radiation from the occupation number statistics. *Optics Express* **29**, 40374–40396 (2021).

- Pop, M., Allaria, E., Curbis, F., Geloni, G., Manfredda, M., Di Mitri, S., Foglia, L., Garzella, D., Giannessi, L., Mahieu, B., Mahne, N., Mirian, N., Penco, G., **Perosa, G.**, Ribic, P.R., Simoncig, A., Spezzani, C., Trovó, M., Werin, S., Zangrando, M. and De Ninno, G., Single-shot transverse coherence in seeded and unseeded free-electron lasers: A com- parison. *Phys. Rev. Accel. Beams* **25**, 040701. (4 Apr. 2022).

- Penco, G., **Perosa, G.**, Allaria, E., Badano, L., Bencivenga, F., Brynes, A. D., Callegari, C., Capotondi, F., Caretta, A., Cinquegrana, P., Dal Zilio, S., Danailov, M. B., De Angelis, D., Demidovich, A., Di Mitri, S., Foglia, L., Gaio , G., Gessini, A., Giannessi, L., Kurdi, G., Manfredda, M., Malvestuto, M., Masciovecchio, C., Mincigrucci, R., Nikolov, I., Pedersoli, E., Pelli Cresi, S., Principi, E., Ribic, P. R., Simoncig, A., Spampinati, S., Spezzani, C., Sottocorona, F., Trovó, M., Zangrando, M., Chardonnet, V., Hennes, M., Luning, J., Vodungbo, B., Bougiatioti, P., Davis, C., Roesner, B., Sacchi, M., Roussel, E., Jal, E. and De Ninno, g., Nonlinear harmonics of a seeded free-electron laser as a coherent and ultrafast probe to investigate matter at the water window and beyond. *Phys. Rev. A* **105**, 053524. (5 May 2022).
- Prat, E., Craievich, P., Dijkstal, P., Di Mitri, S., Ferrari, E., Lucas, T. G., Malyzhenkov, A., **Perosa, G.**, Reiche , S. and Schietinger, T., Energy spread blowup by intrabeam scattering and microbunching at the SwissFEL injector. *Phys. Rev. Accel. Beams* **25**, 104401 (10 Oct. 2022).
- **Perosa, G.**, Di Mitri, S., Barletta, W.A., Parmigiani, F., Doppler signature in electrodynamic retarded potentials, *PHYSO*, 100136 (2023).

Acknowledgement

This thesis is dedicated to my siblings Giulia and Andrea, for their constant "enantiodromic" presence in my life. The lessons learnt by looking at you are invaluable.
I would like to express my gratitude to Professor Di Mitri, who accepted the burdensome task to supervise me and has invested a lot in teaching me how to be a real scientist. You never failed to be a great example of integrity and conscientiousness and I will treasure your advice. I am grateful because you never doubted my worth and you always recognized my merit.
I am grateful to Professor Masciovecchio, that gave me several opportunities to get involved in research activities at FERMI, allowing me to grasp how actual scientists work and cooperate and letting me experienced the thrill of pioneering research.
I am indebted to Professor Parmigiani for mentoring me during these years. You hadn't save yourself any time and effort to engage with me, without a second thought. The effort put into the correction of this thesis, despite not being your job, is just one of many examples. You nurtured my creativity and polished me up. I consider myself lucky to be your student.
My most sincere and heartfelt thanks to the FERMI team. A significant portion of my research would not have been possible without the support and contributions from all of you. Many thanks to all operators, for patiently help me during the shifts, to the beamline scientists from LDM, TIMER, TIMEX, DiProI and MagneDyn, the laser group, the controls group, PADRES and the accelerator physicists.
In particular, I would like to thank my "FERMI uncles": Enrico Allaria, because I have never found a physicists of your stature (in the literal and the figurative sense of the word) and kindness and, while spending my PhD at FERMI, I had the honor to sit on the shoulders of a giant. David Garzella, for being a supportive figure from the scientific and sympathetic points of view, for the stimulating outcome of our consultations and for the great advice. Giuseppe Maria Penco, who showed me that being a scientist means being enthusiastic and charismatic person, that challenges are necessary to improve, and the right dose of fun does not hurt. Carlo Spezzani, that I had the pleasure of accompanying during these years of experiments and shifts, witnessing and admiring his competence. Last, but not least, he endured the herculean feat of being my office roommates.
Many thanks to Professor De Ninno, for the incentivizing and profound discussions that we had in these years and his availability to always consider my suggestions and ideas, promoting them despite my little experience.
I am thankful to Alexander Darius Brynes, that in several occasions (including the drafting of this thesis) has kindly provided his support and accepted my involvement in his brilliant research.
I want to thank Marco Veronese for the fruitful and pleasing collaboration and the time spent in sharing his expertise and his passion for physics with me.
Special thanks to the many people who read my thesis, spending time in revising it and sharing with me their valuable comments: Domenico Caiazza, Carlo Callegari, Bruno Diviacco, Primož Rebernik Ribič and Marco Zangrando.
I am deeply grateful to doctor Mirian, for the recognition showed by an accomplished and inventive scientist that promoted so actively my research and the great trust that she placed in me.
I am grateful to professor Benatti, because I had the privilege to collaborate with him. I experienced the mindset of an expert theoretician at work, a competence that I hope to acquire eventually.
Finally, many thanks to my "students" Federico and Francesco: despite my aversion for platitudes, I have to admit that I have learnt a lot while dealing with you two.

Bibliography

1. Krinsky, S. & Yu, L. H. Output power in guided modes for amplified spontaneous emission in a single-pass free-electron laser. *Phys. Rev. A* **35,** 3406–3423. doi:10.1103/PhysRevA.35.3406 (8 Apr. 1987).
2. Yu, L. H. Generation of intense uv radiation by subharmonically seeded single-pass free-electron lasers. *Phys. Rev. A* **44,** 5178–5193. doi:10.1103/PhysRevA.44.5178 (8 Oct. 1991).
3. Bonifacio, R. *et al.* Physics of the high-gain FEL and superradiance. *La Rivista del Nuovo Cimento (1978-1999)* **13,** 1–69 (1990).
4. Kondratenko, A. & Saldin, E. Generating of coherent radiation by a relativistic electron beam in an ondulator. *Part. Accel.* **10,** 207–216 (1980).
5. Bonifacio, R., Pellegrini, C. & Narducci, L. *Collective instabilities and high-gain regime free electron laser* in *AIP conference proceedings* **118** (1984), 236–259.
6. Kim, K.-J. Three-dimensional analysis of coherent amplification and self-amplified spontaneous emission in free-electron lasers. *Physical review letters* **57,** 1871 (1986).
7. Bonifacio, R. & Casagrande, F. Instabilities and quantum initiation in the free-electron laser. *Optics Communications* **50,** 251–255. ISSN: 0030-4018. doi:https://doi.org/10.1016/0030-4018(84)90327-4 (1984).
8. Gorobtsov, O. Y. *et al.* Statistical properties of a free-electron laser revealed by Hanbury Brown-Twiss interferometry. *Phys. Rev. A* **95,** 023843. doi:10.1103/PhysRevA.95.023843 (2 Feb. 2017).
9. Benatti, F. *et al.* Quantum state features of the FEL radiation from the occupation number statistics. *Optics Express* **29,** 40374–40396 (2021).
10. Allaria, E. *et al.* Highly coherent and stable pulses from the FERMI seeded free-electron laser in the extreme ultraviolet. *Nature Photonics* **6,** 699–704 (2012).
11. Allaria, E. *et al.* Two-stage seeded soft-X-ray free-electron laser. *Nature Photonics* **7,** 913–918 (2013).
12. Zhang, Z. *et al.* Microbunching-instability-induced sidebands in a seeded free-electron laser. *Phys. Rev. Accel. Beams* **19,** 050701. doi:10.1103/PhysRevAccelBeams.19.050701 (5 May 2016).
13. Saldin, E., Schneidmiller, E. & Yurkov, M. Klystron instability of a relativistic electron beam in a bunch compressor. *Nuclear Instruments and Methods in Physics Research Section A: Accelerators, Spectrometers, Detectors and Associated Equipment* **490,** 1–8 (2002).
14. Bonifacio, R., Cola, M. M., Piovella, N. & Robb, G. R. M. A quantum model for collective recoil lasing. *Europhysics Letters* **69,** 55. doi:10.1209/epl/i2004-10308-1 (Dec. 2004).
15. Bonifacio, R., Piovella, N. & Robb, G. The quantum free electron laser: A new source of coherent, short-wavelength radiation. *Fortschritte der Physik* **57,** 1041–1051. doi:https://doi.org/10.1002/prop.200900097. eprint: https://onlinelibrary.wiley.com/doi/pdf/10.1002/prop.200900097 (2009).
16. Dattoli, G., Palma, E. D., Pagnutti, S. & Sabia, E. Free Electron coherent sources: From microwave to X-rays. *Physics Reports* **739,** 1–51. ISSN: 0370-1573. doi:https://doi.org/10.1016/j.physrep.2018.02.005 (2018).

17. Debus, A., Steiniger, K., Kling, P., Carmesin, C. M. & Sauerbrey, R. Realizing quantum free-electron lasers: a critical analysis of experimental challenges and theoretical limits. *Physica Scripta* **94,** 074001 (2019).

18. Becker, W. & McIver, J. Many-particle quantum theory for a class of free-electron devices. *Physics Reports* **154,** 205–245. ISSN: 0370-1573. doi:https://doi.org/10.1016/0370-1573(87)90068-8 (1987).

19. Gorobtsov, O. Y. *et al.* Seeded X-ray free-electron laser generating radiation with laser statistical properties. *Nature communications* **9,** 1–6 (2018).

20. Penco, G. *et al.* Nonlinear harmonics of a seeded free-electron laser as a coherent and ultrafast probe to investigate matter at the water window and beyond. *Phys. Rev. A* **105,** 053524. doi:10.1103/PhysRevA.105.053524 (5 May 2022).

21. Pop, M. *et al.* Single-shot transverse coherence in seeded and unseeded free-electron lasers: A comparison. *Phys. Rev. Accel. Beams* **25,** 040701. doi:10.1103/PhysRevAccelBeams.25.040701 (4 Apr. 2022).

22. Brynes, A. *et al.* Characterisation of microbunching instability with 2D Fourier analysis. *Scientific Reports* **10,** 1–12 (2020).

23. Brynes, A. D. *et al.* Microbunching instability characterization via temporally modulated laser pulses. *Phys. Rev. Accel. Beams* **23,** 104401. doi:10.1103/PhysRevAccelBeams.23.104401. arXiv: 2010.00252 [physics.acc-ph] (2020).

24. Di Mitri, S. *et al.* Experimental evidence of intrabeam scattering in a free-electron laser driver. *New Journal of Physics* **22,** 083053. doi:10.1088/1367-2630/aba572 (Aug. 2020).

25. Di Mitri, S. & Perosa, G. Electron Beam Transport in Plasma-Accelerator-Driven Free-Electron Lasers in the Presence of Coherent Synchrotron Radiation and Microbunching Instability. *Physics* **2,** 521–530. ISSN: 2624-8174. doi:10.3390/physics2040029 (2020).

26. Perosa, G. *et al.* Linear optics control of sideband instability for improved free-electron laser spectral brightness. *Phys. Rev. Accel. Beams* **23,** 110703. doi:10.1103/PhysRevAccelBeams.23.110703 (11 Nov. 2020).

27. Penco, G. *et al.* Enhanced seeded free electron laser performance with a "cold" electron beam. *Phys. Rev. Accel. Beams* **23,** 120704. doi:10.1103/PhysRevAccelBeams.23.120704 (12 Dec. 2020).

28. Perosa, G. & Di Mitri, S. Matrix model for collective phenomena in electron beam's longitudinal phase space. *Scientific reports* **11,** 1–10 (2021).

29. Mirian, N. S. *et al.* Characterization of soft x-ray echo-enabled harmonic generation free-electron laser pulses in the presence of incoherent electron beam energy modulations. *Phys. Rev. Accel. Beams* **24,** 080702. doi:10.1103/PhysRevAccelBeams.24.080702 (8 Aug. 2021).

30. Born, M., Wolf, E. & Bhatia, A. *Principles of Optics: Electromagnetic Theory of Propagation, Interference and Diffraction of Light* ISBN: 9780521784498 (Cambridge University Press, 2000).

31. Fowles, G. *Introduction to Modern Optics* ISBN: 9780486659572 (Dover Publications, 1989).

32. Gerry, C. & Knight, P. *Introductory Quantum Optics* doi:10.1017/CBO9780511791239 (Cambridge University Press, 2004).

33. Fox, M. *Quantum Optics: An Introduction* ISBN: 9780198566731 (OUP Oxford, 2006).

34. Haus, H. *Electromagnetic Noise and Quantum Optical Measurements* ISBN: 9783540652724 (Springer Berlin Heidelberg, 2000).

35. Eriksson, M., van der Veen, J. F. & Quitmann, C. Diffraction-limited storage rings – a window to the science of tomorrow. *Journal of Synchrotron Radiation* **21,** 837–842. doi:10.1107/S1600577514019286 (Sept. 2014).

36. Yang, P., Li, W., Ren, Z., Bai, Z. & Wang, L. Design of a diffraction-limited storage ring lattice using longitudinal gradient bends and reverse bends. *Nuclear Instruments and Methods in Physics Research Section A: Accelerators, Spectrometers, Detectors and Associated Equipment* **990,** 164968. ISSN: 0168-9002. doi:https://doi.org/10.1016/j.nima.2020.164968 (2021).

37. Foellmi, C. Intensity interferometry and the second-order correlation function in astrophysics. *Astronomy & Astrophysics* **507,** 1719–1727 (2009).

38. Goodman, J., Skrockij, G. & Kokin, A. *Statistical Optics* ISBN: 9780471015024 (Wiley, 1985).

39. Glauber, R. J. The Quantum Theory of Optical Coherence. *Phys. Rev.* **130,** 2529–2539. doi:10.1103/PhysRev.130.2529 (6 June 1963).

40. Ding, Y., Emma, P., Huang, Z. & Kumar, V. Optical klystron enhancement to self-amplified spontaneous emission free electron lasers. *Phys. Rev. ST Accel. Beams* **9,** 070702. doi:10.1103/PhysRevSTAB.9.070702 (7 July 2006).

41. Ding, Y., Emma, P., Huang, Z. & Kumar, V. Erratum: Optical klystron enhancement to self-amplified spontaneous emission free electron lasers [Phys. Rev. Accel. Beams 9, 070702 (2006)]. *Phys. Rev. Accel. Beams* **23,** 019901. doi:10.1103/PhysRevAccelBeams.23.019901 (1 Jan. 2020).

42. Penco, G., Allaria, E., De Ninno, G., Ferrari, E. & Giannessi, L. Experimental Demonstration of Enhanced Self-Amplified Spontaneous Emission by an Optical Klystron. *Phys. Rev. Lett.* **114,** 013901. doi:10.1103/PhysRevLett.114.013901 (1 Jan. 2015).

43. Schroeder, C. Photon statistics of the SASE FEL. *Nuclear Instruments and Methods in Physics Research Section A: Accelerators, Spectrometers, Detectors and Associated Equipment* **483.** Proceedings of the 23rd International Free Electron Laser Confere nce and 8th FEL Users Workshop, 499–503. ISSN: 0168-9002. doi:https://doi.org/10.1016/S0168-9002(02)00369-8 (2002).

44. Saldin, E., Schneidmiller, E. & Yurkov, M. Study of a noise degradation of amplification process in a multistage HGHG FEL. *Optics Communications* **202,** 169–187. ISSN: 0030-4018. doi:https://doi.org/10.1016/S0030-4018(02)01091-X (2002).

45. Murphy, J., Pellegrini, C. & Bonifacio, R. Collective instability of a free electron laser including space charge and harmonics. *Optics Communications* **53,** 197–202. ISSN: 0030-4018. doi:https://doi.org/10.1016/0030-4018(85)90331-1 (1985).

46. Huang, Z. & Kim, K.-J. Three-dimensional analysis of harmonic generation in high-gain free-electron lasers. *Phys. Rev. E* **62,** 7295–7308. doi:10.1103/PhysRevE.62.7295 (5 Nov. 2000).

47. Tremaine, A. *et al.* Experimental Characterization of Nonlinear Harmonic Radiation from a Visible Self-Amplified Spontaneous Emission Free-Electron Laser at Saturation. *Phys. Rev. Lett.* **88,** 204801. doi:10.1103/PhysRevLett.88.204801 (20 May 2002).

48. Saldin, E. L., Schneidmiller, E. A. & Yurkov, M. V. Properties of the third harmonic of the radiation from self-amplified spontaneous emission free electron laser. *Phys. Rev. ST Accel. Beams* **9,** 030702. doi:10.1103/PhysRevSTAB.9.030702 (3 Mar. 2006).

49. Marcus, G. *et al.* Experimental observations of seed growth and accompanying pedestal contamination in a self-seeded, soft x-ray free-electron laser. *Phys. Rev. Accel. Beams* **22,** 080702. doi:10.1103/PhysRevAccelBeams.22.080702 (8 Aug. 2019).

50. Hemsing, E., Halavanau, A. & Zhang, Z. Statistical theory of a self-seeded free electron laser with noise pedestal growth. *Phys. Rev. Accel. Beams* **23,** 010701. doi:10.1103/PhysRevAccelBeams.23.010701 (1 Jan. 2020).

51. Zhang, Z. *et al.* Statistical analysis of a self-seeded x-ray free-electron laser in the presence of the microbunching instability. *Phys. Rev. Accel. Beams* **23,** 010704. doi:10.1103/PhysRevAccelBeams.23.010704 (1 Jan. 2020).

52. Di Mitri, S. Coherent Synchrotron Radiation and Microbunching Instability. *CERN Yellow Reports: School Proceedings* **1,** 381–381 (2018).

53. Saldin, E., Schneidmiller, E. & Yurkov, M. Longitudinal space charge-driven microbunching instability in the TESLA Test Facility linac. *Nuclear Instruments and Methods in Physics Research Section A: Accelerators, Spectrometers, Detectors and Associated Equipment* **528.** Proceedings of the 25th International Free Electron Laser Conference, and the 10th FEL Users Workshop, 355–359. ISSN: 0168-9002. doi:https://doi.org/10.1016/j.nima.2004.04.067 (2004).

54. Huang, Z. & Kim, K.-J. Formulas for coherent synchrotron radiation microbunching in a bunch compressor chicane. *Phys. Rev. ST Accel. Beams* **5,** 074401. doi:10.1103/PhysRevSTAB.5.074401 (7 July 2002).

55. Bosch, R. A., Kleman, K. J. & Wu, J. Modeling two-stage bunch compression with wakefields: Macroscopic properties and microbunching instability. *Phys. Rev. ST Accel. Beams* **11,** 090702. doi:10.1103/PhysRevSTAB.11.090702 (9 Sept. 2008).

56. Zotter, B. W. & Kheifets, S. *Impedances and Wakes in High Energy Particle Accelerators* doi:10.1142/3068. eprint: https://www.worldscientific.com/doi/pdf/10.1142/3068 (WORLD SCIENTIFIC, 1998).

57. Huang, Z. *et al.* Suppression of microbunching instability in the linac coherent light source. *Phys. Rev. ST Accel. Beams* **7,** 074401. doi:10.1103/PhysRevSTAB.7.074401 (7 July 2004).

58. Ratner, D. *et al.* Time-resolved imaging of the microbunching instability and energy spread at the Linac Coherent Light Source. *Phys. Rev. ST Accel. Beams* **18,** 030704. doi:10.1103/PhysRevSTAB.18.030704 (3 Mar. 2015).

59. Di Mitri, S. & Cornacchia, M. Merit functions for the linac optics design for colliders and light sources. *Nuclear Instruments and Methods in Physics Research Section A: Accelerators, Spectrometers, Detectors and Associated Equipment* **735,** 60–65. ISSN: 0168-9002. doi:https://doi.org/10.1016/j.nima.2013.08.086 (2014).

60. Di Mitri, S. & Spampinati, S. Microbunching Instability Suppression via Electron-Magnetic-Phase Mixing. *Phys. Rev. Lett.* **112,** 134802. doi:10.1103/PhysRevLett.112.134802 (13 Apr. 2014).

61. Huang, Z. *et al.* Measurements of the linac coherent light source laser heater and its impact on the x-ray free-electron laser performance. *Phys. Rev. ST Accel. Beams* **13,** 020703. doi:10.1103/PhysRevSTAB.13.020703 (2 Feb. 2010).

62. Spampinati, S. *et al.* Laser heater commissioning at an externally seeded free-electron laser. *Phys. Rev. ST Accel. Beams* **17,** 120705. doi:10.1103/PhysRevSTAB.17.120705 (12 Dec. 2014).

63. Lee, J. *et al.* PAL-XFEL laser heater commissioning. *Nuclear Instruments and Methods in Physics Research Section A: Accelerators, Spectrometers, Detectors and Associated Equipment* **843,** 39–45. ISSN: 0168-9002. doi:https://doi.org/10.1016/j.nima.2016.11.001 (2017).

64. Hamberg, M., Brinker, F. & Scholz, M. *Commissioning and First Heating with the European XFEL Laser Heater* in *Proc. IPAC'17* Copenhagen, Denmark, May 2017 (JACoW Publishing, Geneva, Switzerland), 2625–2627. doi:10.18429/JACoW-IPAC2017-WEPAB024.

65. Roussel, E. *et al.* Multicolor High-Gain Free-Electron Laser Driven by Seeded Microbunching Instability. *Phys. Rev. Lett.* **115,** 214801. doi:10.1103/PhysRevLett.115.214801 (21 Nov. 2015).

66. Weling, A. S. & Auston, D. H. Novel sources and detectors for coherent tunable narrow-band terahertz radiation in free space. *J. Opt. Soc. Am. B* **13,** 2783–2792. doi:10.1364/JOSAB.13.002783 (Dec. 1996).

67. Decking, W. & Obier, F. Layout of the Beam Switchyard at the European XFEL. *Conf. Proc. C* **0806233** (eds Andrian, I. & Petit-Jean-Genaz, C.) WEPC073 (2008).

68. Milas, N. & Gough, C. H. *Design of the SwissFEL Switchyard* in *Proc. FEL'10* Malmö, Sweden, Aug. 2010 (JACoW Publishing, Geneva, Switzerland), 433–436.

69. Placidi, M., Jung, J.-Y., Ratti, A. & Sun, C. Compact spreader schemes. *Nuclear Instruments and Methods in Physics Research Section A: Accelerators, Spectrometers, Detectors and Associated Equipment* **768,** 14–19. ISSN: 0168-9002. doi:https://doi.org/10.1016/j.nima.2014.09.017 (2014).

70. Faatz, B. *et al.* Simultaneous operation of two soft x-ray free-electron lasers driven by one linear accelerator. *New Journal of Physics* **18,** 062002. doi:10.1088/1367-2630/18/6/062002 (June 2016).

71. Hara, T. *et al.* Pulse-by-pulse multi-beam-line operation for x-ray free-electron lasers. *Phys. Rev. Accel. Beams* **19,** 020703. doi:10.1103/PhysRevAccelBeams.19.020703 (2 Feb. 2016).

72. Alotaibi, B. M., Khalil, S. M., McNeil, B. W. J. & Traczykowski, P. Modelling a laser plasma accelerator driven free electron laser. *Journal of Physics Communications* **3,** 065007. doi:10.1088/2399-6528/ab291b (June 2019).

73. Di Mitri, S. & Cornacchia, M. Electron beam brightness in linac drivers for free-electron-lasers. *Physics Reports* **539.** Electron beam brightness in linac drivers for free-electron-lasers, 1–48. ISSN: 0370-1573. doi:https://doi.org/10.1016/j.physrep.2014.01.005 (2014).

74. Wiggins, S. *et al.* High quality electron beams from a laser wakefield accelerator. *Plasma Physics and Controlled Fusion* **52,** 124032 (2010).

75. Huang, Z., Ding, Y. & Schroeder, C. B. Compact X-ray Free-Electron Laser from a Laser-Plasma Accelerator Using a Transverse-Gradient Undulator. *Phys. Rev. Lett.* **109,** 204801. doi:10.1103/PhysRevLett.109.204801 (20 Nov. 2012).

76. Samant, S. A., Upadhyay, A. K. & Krishnagopal, S. High brightness electron beams from density transition laser wakefield acceleration for short-wavelength free-electron lasers. *Plasma Physics and Controlled Fusion* **56,** 095003 (2014).

77. Ferran Pousa, A., Martinez de la Ossa, A. & Assmann, R. W. Intrinsic energy spread and bunch length growth in plasma-based accelerators due to betatron motion. *Scientific reports* **9,** 1–11 (2019).

78. Couprie, M.-E., Loulergue, A., Labat, M., Lehe, R. & Malka, V. Towards a free electron laser based on laser plasma accelerators. *Journal of Physics B: Atomic, Molecular and Optical Physics* **47,** 234001 (2014).

79. Brinkmann, R. *et al.* Chirp Mitigation of Plasma-Accelerated Beams by a Modulated Plasma Density. *Phys. Rev. Lett.* **118,** 214801. doi:10.1103/PhysRevLett.118.214801 (21 May 2017).

80. Pousa, A. F., de la Ossa, A. M., Brinkmann, R. & Assmann, R. Compact multistage plasma-based accelerator design for correlated energy spread compensation. *Physical review letters* **123,** 054801 (2019).

81. Loulergue, A. *et al.* Beam manipulation for compact laser wakefield accelerator based free-electron lasers. *New Journal of Physics* **17,** 023028 (2015).

82. Nghiem, P. A. P. *et al.* Toward a plasma-based accelerator at high beam energy with high beam charge and high beam quality. *Phys. Rev. Accel. Beams* **23,** 031301. doi:10.1103/PhysRevAccelBeams.23.031301 (3 Mar. 2020).

83. Prat, E. *et al.* Energy spread blowup by intrabeam scattering and microbunching at the SwissFEL injector. *Phys. Rev. Accel. Beams* **25,** 104401. doi:10.1103/PhysRevAccelBeams.25.104401 (10 Oct. 2022).

84. Piwinski, A. Intra-beam-scattering (1974).

85. Bjorken, J. D. & Mtingwa, S. K. Intrabeam scattering. *Part. Accel.* **13,** 115–143 (1982).

86. Bane, K. L. An accurate, simplified model of intrabeam scattering. *arXiv preprint physics/0205058* (2002).

87. Piwinski, A., Bjorken, J. D. & Mtingwa, S. K. Wilson Prize article: Reflections on our experiences with developing the theory of intrabeam scattering. *Phys. Rev. Accel. Beams* **21,** 114801. doi:10.1103/PhysRevAccelBeams.21.114801 (11 Nov. 2018).

88. Kubo, K., Mtingwa, S. K. & Wolski, A. Intrabeam scattering formulas for high energy beams. *Phys. Rev. ST Accel. Beams* **8,** 081001. doi:10.1103/PhysRevSTAB.8.081001 (8 Aug. 2005).

89. Le Duff, J. *Single and multiple Touschek effects* tech. rep. (Cern, 1988).

90. Wei, J. *Stochastic cooling and intra-beam scattering in RHIC* tech. rep. (Brookhaven National Lab., Upton, NY (United States), 1993).

91. Venturini, M. *Intrabeam scattering and wakefield effects in low emittance electron rings* in *19th Particle Accelerator Conference (PAC 2001)* (Jan. 2001), 2958–2960.

92. Raubenheimer, T. The core emittance with intrabeam scattering in e^+/e^- rings. **45** (Sept. 1992).

93. Abramowitz, M. & Stegun, I. A. *Handbook of Mathematical Functions with Formulas, Graphs, and Mathematical Tables* ninth Dover printing, tenth GPO printing (Dover, New York, 1964).

94. Tsai, C.-Y. *et al.* Theoretical formulation of phase space microbunching instability in the presence of intrabeam scattering for single-pass or recirculation accelerators. *Phys. Rev. Accel. Beams* **23,** 124401. doi:10.1103/PhysRevAccelBeams.23.124401 (2020).

95. Craievich, P. *et al.* Implementation of radio-frequency deflecting devices for comprehensive high-energy electron beam diagnosis. *IEEE Transactions on Nuclear Science* **62,** 210–220 (2015).

96. Floettmann, K. & Paramonov, V. V. Beam dynamics in transverse deflecting rf structures. *Phys. Rev. ST Accel. Beams* **17,** 024001. doi:10.1103/PhysRevSTAB.17.024001 (2 Feb. 2014).

97. Van der Geer, B. & De Loos, M. *Applications of the General Particle Tracer code* in. **2** (June 1997), 2577–2579 vol.2. doi:10.1109/PAC.1997.751279.

98. Stupakov, G. & Huang, Z. Space charge effect in an accelerated beam. *Physical Review Special Topics-Accelerators and Beams* **11,** 014401 (2008).

99. Stupakov, G. Using the Beam-Echo Effect for Generation of Short-Wavelength Radiation. *Phys. Rev. Lett.* **102,** 074801. doi:10.1103/PhysRevLett.102.074801 (7 Feb. 2009).

100. Allaria, E. & De Ninno, G. Soft-X-Ray Coherent Radiation Using a Single-Cascade Free-Electron Laser. *Phys. Rev. Lett.* **99,** 014801. doi:10.1103/PhysRevLett.99.014801 (1 July 2007).

101. Pavlovic, L., Borga, A. O., Ferianis, M., Predonzani, M. & Rossi, F. *Bunch Arrival Monitor at FERMI@Elettra* in *Proc. BIW'10* Santa Fe, NM, USA, May 2010 (JACoW Publishing, Geneva, Switzerland), 394–397.

102. Finetti, P. *et al.* Pulse Duration of Seeded Free-Electron Lasers. *Phys. Rev. X* **7,** 021043. doi:10.1103/PhysRevX.7.021043 (2 June 2017).

103. Craievich, P., Di Mitri, S., Milloch, M., Penco, G. & Rossi, F. Modeling and experimental study to identify arrival-time jitter sources in the presence of a magnetic chicane. *Phys. Rev. ST Accel. Beams* **16,** 090401. doi:10.1103/PhysRevSTAB.16.090401 (9 Sept. 2013).

104. Ferrari, E. *et al.* Widely tunable two-colour seeded free-electron laser source for resonant-pump resonant-probe magnetic scattering. *Nature Communications* **7,** 1–8 (2016).

105. Zangrando, M. *et al.* The photon analysis, delivery, and reduction system at the FERMI@ Elettra free electron laser user facility. *Review of Scientific Instruments* **80,** 113110 (2009).

106. Svetina, C. *et al.* PRESTO, the on-line photon energy spectrometer at FERMI: design, features and commissioning results. *Journal of Synchrotron Radiation* **23,** 35–42 (2016).

107. Xiang, D. & Stupakov, G. Echo-enabled harmonic generation free electron laser. *Phys. Rev. ST Accel. Beams* **12,** 030702. doi:10.1103/PhysRevSTAB.12.030702 (3 Mar. 2009).

108. Hemsing, E. *et al.* Echo-enabled harmonics up to the 75th order from precisely tailored electron beams. *Nature Photonics* **10,** 512–515 (2016).

109. Rebernik Ribič, P. *et al.* Coherent soft X-ray pulses from an echo-enabled harmonic generation free-electron laser. *Nature Photonics* **13,** 555–561 (2019).

110. Huang, Z., Ratner, D., Stupakov, G. & Xiang, D. Effects of energy chirp on echo-enabled harmonic generation free-electron lasers (Feb. 2009).

111. Penn, G. Stable, coherent free-electron laser pulses using echo-enabled harmonic generation. *Phys. Rev. ST Accel. Beams* **17,** 110707. doi:10.1103/PhysRevSTAB.17.110707 (11 Nov. 2014).

112. Rebernik Ribič, P. *et al.* Echo-Enabled Harmonic Generation Studies for the FERMI Free-Electron Laser. *Photonics* **4.** ISSN: 2304-6732. doi:10.3390/photonics4010019 (2017).

113. Hemsing, E., Garcia, B., Huang, Z., Raubenheimer, T. & Xiang, D. Sensitivity of echo enabled harmonic generation to sinusoidal electron beam energy structure. *Phys. Rev. Accel. Beams* **20,** 060702. doi:10.1103/PhysRevAccelBeams.20.060702 (6 June 2017).

114. Hemsing, E. Bunching phase and constraints on echo enabled harmonic generation. *Phys. Rev. Accel. Beams* **21,** 050702. doi:10.1103/PhysRevAccelBeams.21.050702 (5 May 2018).

115. Hemsing, E. Minimum spectral bandwidth in echo seeded free electron lasers. *Frontiers in Physics* **7,** 35 (2019).

116. Venturini, M. & Qiang, J. Transverse space-charge induced microbunching instability in high-brightness electron bunches. *Phys. Rev. ST Accel. Beams* **18,** 054401. doi:10.1103/PhysRevSTAB.18.054401 (5 May 2015).

117. Zhang, K., Zeng, L., Qi, Z., Feng, C. & Wang, D. Eliminating the microbunching-instability-induced sideband in a soft x-ray self-seeding free-electron laser. *Nuclear Instruments and Methods in Physics Research Section A: Accelerators, Spectrometers, Detectors and Associated Equipment* **882,** 22–29 (2018).

118. Loudon, R. *The quantum theory of light* (OUP Oxford, 2000).

119. Glauber, R. J. Dirac's Famous Dictum on Interference: One Photon or Two? *American Journal of Physics* **63,** 12–12 (1995).

120. Paul, H. *et al. Introduction to quantum optics: from light quanta to quantum teleportation* (Cambridge University Press, 2004).

121. Barnett, S. M. On single-photon and classical interference. *Physica Scripta* **97,** 114004. doi:10.1088/1402-4896/ac971a (Oct. 2022).

122. Van Enk, S. J. & Fuchs, C. A. Quantum State of an Ideal Propagating Laser Field. *Phys. Rev. Lett.* **88,** 027902. doi:10.1103/PhysRevLett.88.027902 (2 Dec. 2001).

123. in. *Table of Integrals, Series, and Products (Eighth Edition)* (eds Zwillinger, D., Moll, V., Gradshteyn, I. & Ryzhik, I.) Eighth Edition, 867–1013 (Academic Press, Boston, 2015). ISBN: 978-0-12-384933-5. doi:https://doi.org/10.1016/B978-0-12-384933-5.00008-4.

124. Genovese, M. *et al.* Measuring the photon distribution with on/off photodetectors. *Laser physics* **16,** 385–392 (2006).

125. Brida, G. *et al.* Constrained MaxLik reconstruction of multimode photon distributions. *Journal of Modern Optics* **56,** 196–200. doi:10.1080/09500340802389805. eprint: https://doi.org/10.1080/09500340802389805 (2009).

126. Casella, G., Robert, C. P. & Wells, M. T. Generalized Accept-Reject Sampling Schemes. *Lecture Notes-Monograph Series* **45,** 342–347. ISSN: 07492170 (2004).

127. Kondratenko, A. M. & Saldin, E. L. Generating Of Coherent Radiation By A Relativistic Electron beam In An ondulator. *Part. Accel.* **10,** 207–216 (1980).

128. Saldin, E. L., Schneidmiller, E. A. & Yurkov, M. V. Statistical and coherence properties of radiation from x-ray free-electron lasers. *New Journal of Physics* **12,** 035010. doi:10.1088/1367-2630/12/3/035010 (Mar. 2010).

129. Bonifacio, R., McNeil, B. W. J. & Pierini, P. Superradiance in the high-gain free-electron laser. *Phys. Rev. A* **40,** 4467–4475. doi:10.1103/PhysRevA.40.4467 (8 Oct. 1989).

130. Hasan, M. Z. & Kane, C. L. Colloquium: Topological insulators. *Rev. Mod. Phys.* **82,** 3045–3067. doi:10.1103/RevModPhys.82.3045 (4 Nov. 2010).

131. Wolkow, D. M. Uber eine Klasse von Losungen der Diracschen Gleichung. *Z. Phys.* **94,** 250–260. doi:10.1007/BF01331022 (1935).

132. Berson, I. Electron in the Quantized Field of a Monochromatic Electromagnetic Wave. *Soviet Journal of Experimental and Theoretical Physics* **29,** 871 (Jan. 1969).

133. Beers, B. & Nickle, H. Algebraic Solution for a Dirac Electron in a Plane-Wave Electromagnetic Field. *Journal of Mathematical Physics* **13,** 1592–1595 (1972).

134. Bagrov, V. G., Gitman, D. M. & Kuchin, V. A. Electron in the field of a classical and a quantized plane wave traveling in the same direction. *Soviet Physics Journal* **17,** 952–956. doi:10.1007/BF00891066 (July 1974).

135. Bergou, J. & Varro, S. Nonlinear scattering processes in the presence of a quantised radiation field. II. Relativistic treatment. *Journal of Physics A: Mathematical and General* **14,** 2281. doi:10.1088/0305-4470/14/9/023 (Sept. 1981).

136. Dattoli, G., Richetta, M. & Torre, A. Operator disentanglement. *Phys. Rev. A* **37,** 2007–2011. doi:10.1103/PhysRevA.37.2007 (6 Mar. 1988).

137. Bocchetta, C. J. & other. *FERMI@Elettra FEL Conceptual Design Report, ST/F-TN-07/12*

138. Roussel, E. *et al.* Polarization Characterization of Soft X-Ray Radiation at FERMI FEL-2. *Photonics* **4.** ISSN: 2304-6732. doi:10.3390/photonics4020029 (2017).

139. Howe, J. *et al.* Comparison of film detectors, charged-coupled devices, and imaging plates in x-ray spectroscopy of hot dense plasma. *Review of Scientific Instruments* **77,** 036105. doi:10.1063/1.2166515. eprint: https://doi.org/10.1063/1.2166515 (2006).

140. Hirono, T. *et al. Characterization of fully depleted CMOS active pixel sensors on high resistivity substrates for use in a high radiation environment* in *2016 IEEE Nuclear Science Symposium, Medical Imaging Conference and Room-Temperature Semiconductor Detector Workshop (NSS/MIC/RTSD)* (2016), 1–4. doi:10.1109/NSSMIC.2016.8069902.

141. Giampaolo, R. A. *et al. Depleted MAPS on a 110 nm CMOS CIS Technology* in *2019 26th IEEE International Conference on Electronics, Circuits and Systems (ICECS)* (2019), 514–517. doi:10.1109/ICECS46596.2019.8964823.

142. Ruat, M. & Ponchut, C. Characterization of a Pixelated CdTe X-Ray Detector Using the Timepix Photon-Counting Readout Chip. *IEEE Transactions on Nuclear Science* **59,** 2392–2401. doi:10.1109/TNS.2012.2210909 (2012).

143. Ghioni, M., Gulinatti, A., Rech, I., Zappa, F. & Cova, S. Progress in Silicon Single-Photon Avalanche Diodes. *IEEE Journal of Selected Topics in Quantum Electronics* **13,** 852–862. doi:10.1109/JSTQE.2007.902088 (2007).

144. Braga, L. H. C. *et al.* A Fully Digital 8×16 SiPM Array for PET Applications With Per-Pixel TDCs and Real-Time Energy Output. *IEEE Journal of Solid-State Circuits* **49,** 301–314. doi:10.1109/JSSC.2013.2284351 (2014).

145. Conca, E. *et al.* Large-Area, Fast-Gated Digital SiPM With Integrated TDC for Portable and Wearable Time-Domain NIRS. *IEEE Journal of Solid-State Circuits* **55,** 3097–3111. doi:10.1109/JSSC.2020.3006442 (2020).